Leading Edge Aeronautics Research for NASA (LEARN)

Cooperative Gust Sensing and Suppression for Aircraft Formation Flight

Final Report

Principal Investigator (PI)
Marcello R. Napolitano, Professor
Director of Flight Control Systems Laboratory
West Virginia University (WVU)
PO Box 6106, Morgantown, WV 26506/6106
Tel. (304) 293-3304, FAX (304) 293-4970
Email: *Marcello.Napolitano@mail.wvu.edu*

Period of Performance: Nov. 14, 2012 – Dec. 31, 2013

Grant # NNX13AB74A

Science Co-I(s)
Haiyang Chao, Assistant Professor.
Aerospace Engineering Department
University of Kansas (KU)
E-mail: *chaohaiyang@ku.edu*
and
Yu Gu, Assistant Professor
Interactive Robotics Laboratory
Mechanical & Aerospace Engineering Department
West Virginia University (WVU)
E-mail: *Yu.Gu@mail.wvu.edu*

Technical Officer
Curtis E. Hanson
NASA Dryden Flight Research Center
PO Box 273, MS 4840D, Edwards CA 93523-0273
Phone: (661) 276-3966
Email: *curtis.e.hanson@nasa.gov*

Submitted to:
Ms. Theresa Stanley
NASA/Shared Services Center, MS XD
Stennis Space Center, MS 39529-6000
Telephone: (877) 677-2123
Email: nssc-contractcenter@nasa.gov

February 2014

Cooperative Gust Sensing and Suppression for Aircraft Formation Flight

Motivation

Aircraft formation flight has shown great potential benefits for future commercial applications. For example, a fuel saving up to 18% for the trailing aircraft was demonstrated in 2001 by the NASA Autonomous Formation Flight (AFF) program (*Vachon et. al., 2002*). The reduced fuel consumption along with the associated lower environmental impact can potentially foster the development of a sustainable air transportation industry. Additionally, formation flight could also allow air traffic control systems to better handle the increasing traffic in the next generation airspace.

One of the critical technical issues to be addressed before commercial aircraft can routinely fly in formation is the problem of turbulence suppression. In fact, since the trailing aircraft is always flying in the wingtip vortex of a leading aircraft, the design and operational implementation of active turbulence suppression system is a critical issue for both flight safety and passenger comfort. From a different perspective, the extended spatial sensing range with a group of aircraft also creates new opportunities for the cooperative sensing and suppression of ambient and wake induced atmospheric gusts and turbulences.

Executive Summary

The following three tasks/milestones were proposed within the Phase I proposal document:

1. Cooperative gust and turbulence sensing and prediction;
2. Active gust suppression control;
3. Flight simulation and validation.

The technical achievements in Phase I are summarized below.

Cooperative Gust and Turbulence Sensing and Prediction

An Unscented Kalman Filter (UKF) has been developed to provide real-time wind estimates through the fusion of measurements from multiple on-board sensors (GPS, Inertial Measurement Unit, pilot-tube, and air-flow vanes). The wind estimation results have shown a desirable match between simulation data and measurements from the ground weather station (*Rhudy, et al., 2013*).

A cooperative wind sensing strategy was also developed. Within this approach, the leader is used as a remote sensor platform for the follower. The leader performs ambient wind estimation using its onboard sensors that can provide information for predicting its wake propagation according to the flight state and the estimated ambient wind condition. The predicted 3D wind components at the follower location are then used as a set of measurement for the wind-estimation UKF running on the follower. The cooperative wind sensing algorithm was evaluated with simulations; a substantial improvement in wind estimation performance was achieved compared with the non-cooperative algorithm.

Active Gust Suppression Control

The WVU formation control laws are formulated based on a previous design featuring an inner/outer loop architecture (*Gu, et al., 2009*). The inner loop control laws perform attitude

tracking and passive turbulence suppression functions, while the outer-loop control is tasked with maintaining the formation geometry. Additionally, a set of gust suppression control laws was developed, which includes a feed-forward link from the predicted ambient and wake turbulence using leader provided information.

Flight Simulation and Validation

A comprehensive formation flight simulator was developed during Phase I of the effort. The simulator features high fidelity aircraft models, formation flight control laws, ambient wind and gust, wake propagation models, wind estimation filters, and visualization tools. The simulation environment has proven to be a critical tool for the project.

Fig.1. Phastball Aircraft in Close Formation Flight

High priority was given to the flight testing program in the second half of the effort (April-November 2013). More than 40 flight tests were performed during the 2013 flight testing season, including 13 two-aircraft formation flight experiments. In addition to accomplishing the wind data collection objective proposed for Phase I, the following additional objectives were achieved:

1. Demonstrated that precision close formation flight is achievable with two low-cost sub-scale aircraft platforms. Close formation flight with a 5-wing span (~12 m) distance - as shown in Figure 1- was performed in 8 experiments. The standard deviation error was found to be ~1 m during the straight portion of the flight.
2. Demonstrated that small subscale aircraft (~25 lbs.) will generate vortices with enough magnitude and strength to be sensed by the follower before dissipating in the ambient wind. Flight data from a representative wake encountering event is shown in Figure 2.
3. Acquired direct observations and valuable insights about the aircraft wake through a series of flow visualization experiments using a Remotely Controlled (RC) trainer aircraft, as shown in Figure 3.

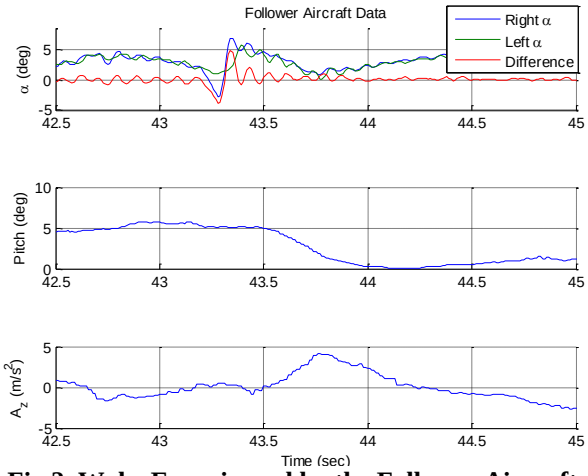

Fig.2. Wake Experienced by the Follower Aircraft (the left and right α vanes are 25cm apart laterally)

Fig.3. Wake Vortex Visualization with a RC

Final Report

Period of Performance: November 14, 2012 – December 31, 2013

Objective

The key objective of this research effort is the development of a cooperative strategy for gust sensing and suppression within a formation flight setting. Specifically, each trailing aircraft will analyze real-time flight data collected from leading aircraft to estimate the effects of ambient and wake turbulences on its airframe.

Status of Technical Work

Throughout the project, the research activities focused on the following three research areas:

Research Area #1: Development of a UAV Formation Flight Simulator

A key aspect of the overall effort was the development of an accurate Matlab/Simulink-based flight simulator for the validation of formation flight controller as well as wind/gust/wake estimation algorithms. During the effort, a flight simulation framework - named WVU Phastball Multi-UAV Simulator (WVU-PMUS) - has been developed to support the above tasks. Simulation results have shown the effectiveness of the designed framework with a desirable match between actual flight data and the PMUS simulated results. In addition, a formation control law based on a Non Linear Dynamic Inversion (NLDI) approach has been adapted from a prior design. Simulation results have shown the accurate tracking of two-aircraft formation through pre-planned trajectory.

Research Area #2: Flight Validation of Multi-UAV Framework & Wake Encounter Test

Flight testing efforts for the investigation including hardware debugging and flight software development have been incrementally conducted throughout the project. A Linear-Quadratic (LQ) inner loop flight controller was validated in the initial phase of the effort. In a later phase, emphasis was placed on the development of the software for the outer loop flight controller using a virtual leader strategy. The final stage focused on intensive testing of two-aircraft formation flights with the offset distances ranging from 5 to 20 wingspans. The accurate tracking performance during close formation flight (as close as 5-wing span) showed the effectiveness of the proposed multi-UAV framework. More importantly, the close formation flights coincided with the wake encounter flight tests. The wakes generated by the leading Phastball UAV have been successfully detected by the follower aircraft, observed from onboard sensor measurements. Phase II efforts will focus on the quantification of the detected wake vortex of the Phastball UAV.

Research Area #3: Wind Gust Sensing and Suppression Control Using Small UAVs

The design of the gust estimation algorithm has focused on Unscented Kalman Filter (UKF) approaches using the aircraft on-board measurements including GPS, inertial sensors, pitot-tube, and air flow sensors. Two UKF algorithms were developed respectively for single-aircraft and leader-follower scenarios. The difference of the two filters lies in the fact that the cooperative UKF utilize the wake and ambient wind information sensed and broadcasted by the leading aircraft. The designed UKF algorithms showed desirable performance for the estimation of the wind and gusts in single-aircraft flights and leader-follower flight simulations. Additionally, a

Phastball UAV wake simulation model is developed based from Hallock Burnham vortex model and Sarpkaya decaying model. Based on the proposed wake model and formation control law, a set of preliminary suppression control laws were developed and simulated.

Student Involvement and Activities

a) Number of students involved in research activities

The PI and the Science Co-Is have conducted efforts towards recruiting talented graduate students from West Virginia University and from other institutions. A team of students – including both graduate and undergraduate students – have been assembled to work on the project. The following paragraphs briefly introduce these students and describe their specific technical roles in the project.

The 1st student is Mr. Trenton Larrabee. Mr. Larrabee received his B.S. degree from WVU. Mr. Larrabee joined the team as a graduate research assistant in Spring 2011; he has been involved in the development of wind estimation algorithms, the flight validation of inner loop controller and UAV ground control station, and the wake encounter flight tests. Mr. Larrabee has graduated with a M.S. degree in December, 2013. He is currently employed at the US Navy base in Patuxent River, MD.

The 2nd student is Mr. Caleb Rice. Mr. Rice received his B.S. degree from WVU in 2012 and is currently pursuing his M.S. degree in Aerospace Engineering. Mr. Rice served as a NASA Ames Aeronautics Academy Research Associate under the NASA's leadership program in Summer 2012. Mr. Rice has worked on the development of multi-UAV simulator, and the implementation of the formation flight controller for flight test validations.

The 3rd student is Mr. Lucas A. Behrens. Mr. Behrens is a WVU undergraduate student. Mr. Behrens joined the team in Summer 2013; he has been actively involved with flight testing activities as well as with the maintenance and the upgrades of the Phastball UAV fleet.

b) Ethnic background of current participants

4 Caucasian males;
(PI, 2 Graduate Research Assistants, and 1 Undergraduate Student)
2 Asian (China) male;
(1 Science Co-I)

c) Level of education for participants

2 Professors (PI, Science Co-I);
1 Post Doctoral Fellow (Science Co-I, researcher);
2 M.S. students, Graduate Research Assistants;
1 Undergraduate student.

Patents or Inventions, etc.

N/A.

Synergetic Activities

a) Travel

- Flight-testing and field activities were conducted from April to December throughout the project duration at the WVU Jackson's Mill facility near Weston, WV.

- Faculty travel has included registration fees of American Control Conference 2013, which was held in Washington DC from June 17-19th, 2013.

- Student travel has included registration fees of AIAA GNC Conference 2013, which was held in Boston, Massachusetts from Aug. 19-22nd, 2013.

b) Communications

The WVU research team has had regular technical interaction with Mr. Curtis E. Hanson (NASA Dryden Technical Monitor) and Mr. Joe Pahle (NASA Dryden Scientist). Technical interactions have consisted of e-mail exchanges and phone calls. The communication involved detailed presentations displaying contributions and ongoing activities by all project participants, laboratory and simulation demonstrations, and a review of the flight-testing data and flight testing plan.

Number and Description of Publications and/or Presentations

The following papers have been submitted and accepted for presentation at the 2013 AIAA Guidance, Navigation, and Control (GNC) Conference held in Boston, Massachusetts:

- *Rhudy, M., Larrabee, T., Chao, H., Gu, Y., and Napolitano, M.R.,* "UAV Attitude, Heading, and Wind Estimation Using GPS/INS and an Air Data System," the 2013 AIAA Guidance, Navigation, and Control Conference, ID#: 1659091, Boston, Massachusetts, Aug. 19-22, 2013;
- *Larrabee, T., Chao, H., Mandal, T., Gururajan, S., Gu, Y., and Napolitano, M.R.,* "Design, Simulation, and Flight Test Validation of a UAV Ground Control Station for Aviation Safety Research and Pilot Modeling," the 2013 AIAA Guidance, Navigation, and Control Conference, ID#: 1664533, Boston, Massachusetts, Aug. 19-22, 2013;

The following manuscripts have been submitted and are currently under review:

- *Larrabee, T., Chao, H., Gu, Y., and Napolitano, M.R.,* "Wind Field and Wake Estimation in UAV Formation Flight," submitted to the 2014 American Control Conference, currently under review;
- *Rice, C., Gu, Y., Chao, H., Larrabee, T., Gururajan, S., and Napolitano, M.R.,* "Control Performance Analysis for Autonomous Close Formation Flight Experiments," submitted to the 2014 American Control Conference, currently under review;

A copy of the published papers along with the abstracts of the publications currently under review have been included in Appendix A.

Expenditures

A summary of the project expenditures as provided by the WVU Accounting System is given below:

• Salary (Benefit Eligible)	$	66,256
• Salary (Student)	$	29,900
• Fringe Benefit rates	$	18,971
• Travel	$	3,598
• General Expenses (f. testing activities / laboratory expenditures)	$	5,942
• Overhead	$	62,661
Total to date	**$**	**187,328**

NOTE: Due to a 4-6 weeks delay in the detailed accounting of the expenses in the WVU system, there are likely discrepancies between the actual expenses and the currently reported expenses. As of 12/31/2013 the total expenditures for the project totaled $200,000.

Cooperative Gust Sensing and Suppression for Aircraft Formation Flight

Technical Summary

Section #1

1. Simulator Development for UAV Formation Flight

The WVU Phastball Multi-UAV Simulator (WVU-PMUS) was developed to support the simulation of single UAV flight, multiple UAV flight, and wind/gust/wake sensing algorithms. The Matlab/Simulink-based simulator served as a validation tool for both new flight controllers and novel estimation algorithms. After the simulation validation, the designed control laws or estimator were integrated with the Phastball UAV hardware with a minimal effort for code conversion. In addition, the simulator has been integrated with the Matlab Virtual Reality Toolbox (VRT) for visualization purposes. Based on the UAV model, the formation flight controller has been simulated and validated, showing good tracking of predesigned trajectory.

1.1 – Phastball UAV Platform

The PMUS simulator features the mathematical model of the Phastball UAV platform. This research platform was designed, manufactured, and instrumented by researchers at the WVU Flight Control Systems Laboratory (FCSL) at WVU. A fleet of Phastball UAVs have been built with Phastball 'Blue' shown in Figure 1.1. The WVU Phastball has a length and a wingspan of approximately 2.2 m. and 2.4 m. respectively. It features a mid-wing and T-tail configuration with two brushless electric ducted-fan motors mounted behind the wings. The WVU Phastball has a take-off weight of approximately 11 Kg with a payload of 3 Kg. The cruise speed is approximately 30 m/s. The fuselage is manufactured using carbon fiber and fiberglass composite with plywood bulkheads and rails used for avionics mounting.

For the onboard avionics, each WVU Phastball is equipped with a PC104-based flight computer (PC104) and a complete sensor suite including GPS, Inertial Measurement Unit (IMU), three potentiometers for the measurement of aircraft flow angles (two for angle-of-attack and one for sideslip angle), humidity and temperature sensor, laser range finder, and a pitot tube for both static and dynamic pressure measurements. For communication purposes, the aircraft features a FreeWave 900 MHz wireless data transceiver.

Figure 1.1 WVU 'Blue' Phastball UAV

1.2 – Phastball UAV Simulator Development

The WVU-PMUS simulation code is based on the open source Flight Dynamics and Control (FDC) toolbox developed in MATLAB/Simulink (*Rauw, 2001*). FDC provides a basic default

nonlinear model for a general aircraft. The default model is based on the interaction of several blocks with different functions. The 'Aerodynamic Data' block computes aerodynamic forces and coefficients, the 'Engine Group' computes thrust forces and moments, the 'Gravity Block' computes gravity forces and the 'Wind Block' computes atmospheric forces and wind gust disturbances. They all contribute to the block "Equation of Motion", which is used for the calculation of the derivatives of the states and successive integration. Figure 1.2 shows the main block of the FDC-based Phastball UAV Simulator, including all the blocks described above.

The default nonlinear aircraft model from FDC can be customized according to the requirements of small UAVs. The core FDC has been updated based upon the identified parameters of the Phastball UAV including the aerodynamic derivatives and geometrical coefficients divided in the following groups of parameters:

- Geometry and mass properties;
- Aerodynamic drag derivatives;
- Aerodynamic lift derivatives;
- Aerodynamic Lateral Moment derivatives;
- Aerodynamic Lateral Force derivatives;
- Aerodynamic Horizontal Force derivatives;
- Aerodynamic Vertical Moment derivatives;
- Vector of initial conditions (12 states).

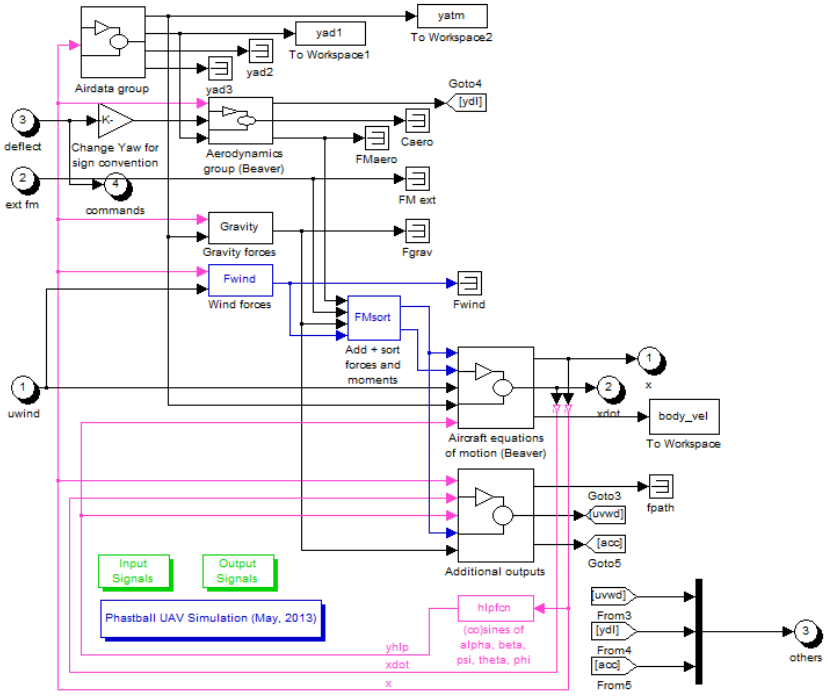

Figure 1.2 – FDC-based Phastball UAV Simulator

The mask used to input the Phastball aerodynamic coefficients is shown in **Error! Reference source not found.**. The coefficients are used to compute the forces and moments of the aircraft, which are integrated by the equations of motion block for the calculation of the system outputs.

The outputs are 12 states commonly used to describe the dynamics of an aircraft with 6 degrees of freedom:

$$x = \begin{bmatrix} V & \alpha & \beta & p & q & r & \psi & \theta & \phi & x & y & H \end{bmatrix}$$

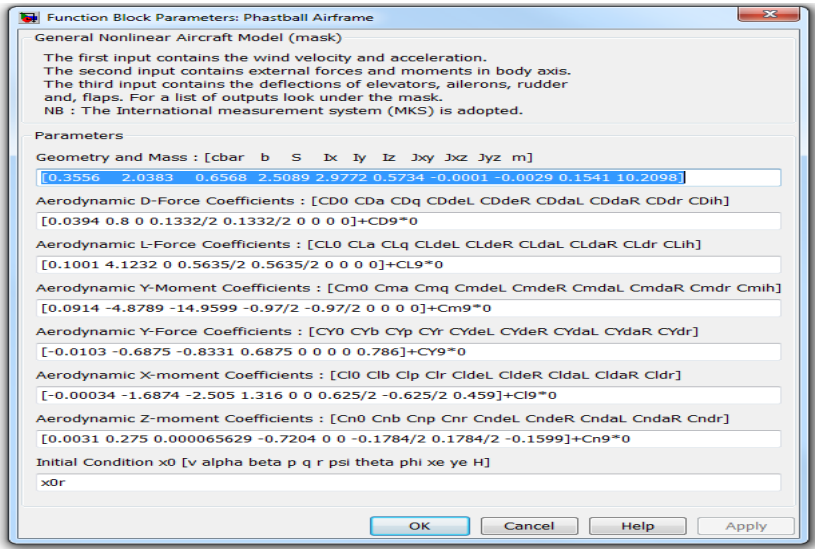

Figure 1.3 – FDC Coefficients Input Masks

The Phastball UAV inertial coefficients (shown in the 1st row in Figure 1.3) have been calculated using FEM codes throughout the design of the aircraft.

The Phastball thrust parameters have been identified through a series of ground and flight tests. The thrust modeling test was designed and performed on the ground. The relationship between the static thrust and the throttle Pulse Width Modulation (PWM) signal was identified using a digital scale for force measurement and a microprocessor for PWM logging. The identified relationship function is listed as the following and displayed in Figure 1.4.

$$T_{static} = 0.00022x^2 - 0.011x - 0.33$$

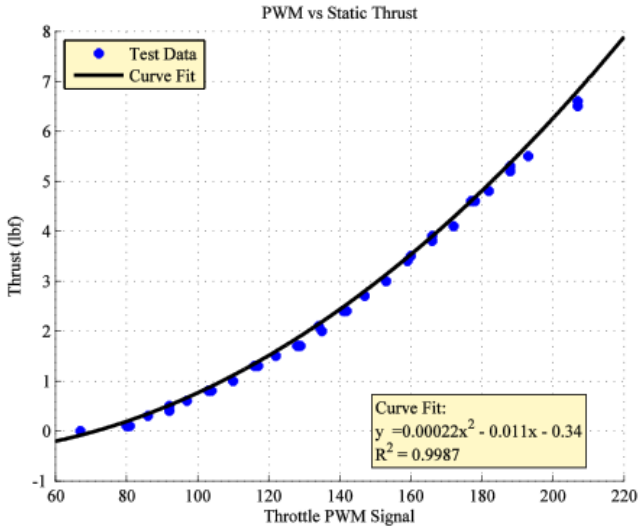

Figure 1.4: Static Thrust vs PWM Signal

With the identified static thrust, the dynamic thrust can then be calculated as:

$$T_{dynamic} = T_{static} - \dot{m}V_{in}$$

where $\dot{m}$ is the mass flow rate and V_{in} is the velocity of the air immediately in front of the fan.

The Phastball aerodynamic parameters were identified following a Parameter Identification (PID) effort using 40 different segments of flight data, with each segment lasting about 10 seconds following predesigned maneuvers (*McGrail, A. K., 2012*). Orthogonal multisines simultaneously performed on the elevators, ailerons, and rudder were selected as the PID maneuver of choice, due to restrictions on the maneuver time, the amplitude of surface movements, and the size of the flight field. The example multisine inputs are shown in Figure 1.5. The parameter identification efforts were conducted in the time domain using the Maximum Likelihood Estimator (MLE) with Newton-Raphson minimization and starting estimates determined using Least Squares Estimation (*Klein, V., and Morelli, E.A., 2006*).

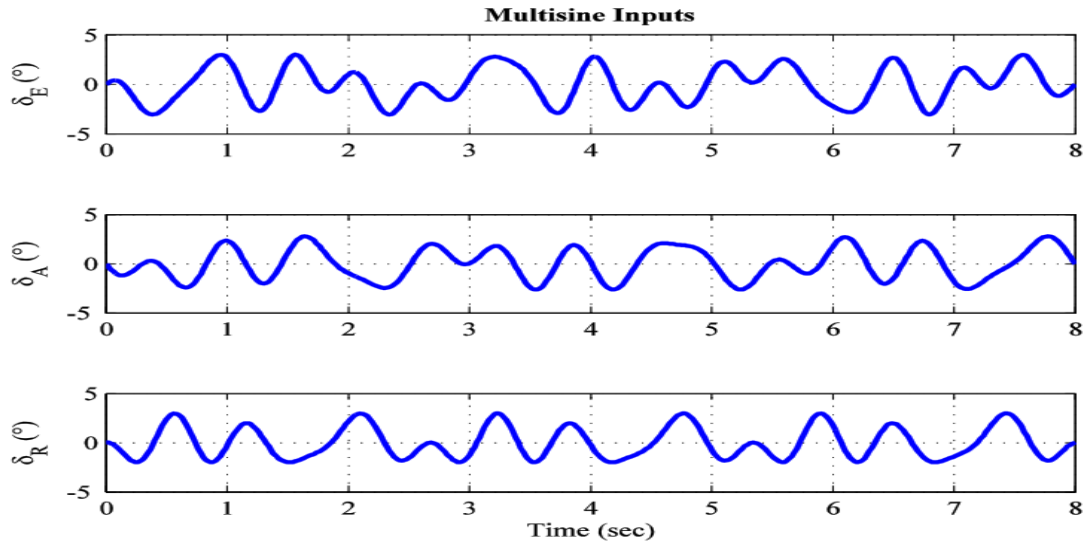

Figure 1.5: Designed Multisine Inputs on the Control Surfaces

Following the PID study in the time-domain, a second study was performed using the frequency-based PID approach introduced by Gene Morelli at NASA Langley (*Klein, V., and Morelli, E.A., 2006*). Both studies provided very similar and consistent results for most of the aerodynamic coefficients, especially the most critical coefficients $\left(c_{L_\alpha}, c_{m_\alpha}, c_{l\beta}, c_{n\beta}\right)$. The final set of values for the Phastball aerodynamic coefficients can be found in (*McGrail, A. K., 2012*).

After the PID analysis, several additional sets of flight data were used for the validation of the identified aerodynamic coefficients. The analysis revealed a desirable match between flight data and simulated data for both the longitudinal and the lateral-directional dynamics, as shown in Figure 1.6 and 1.7.

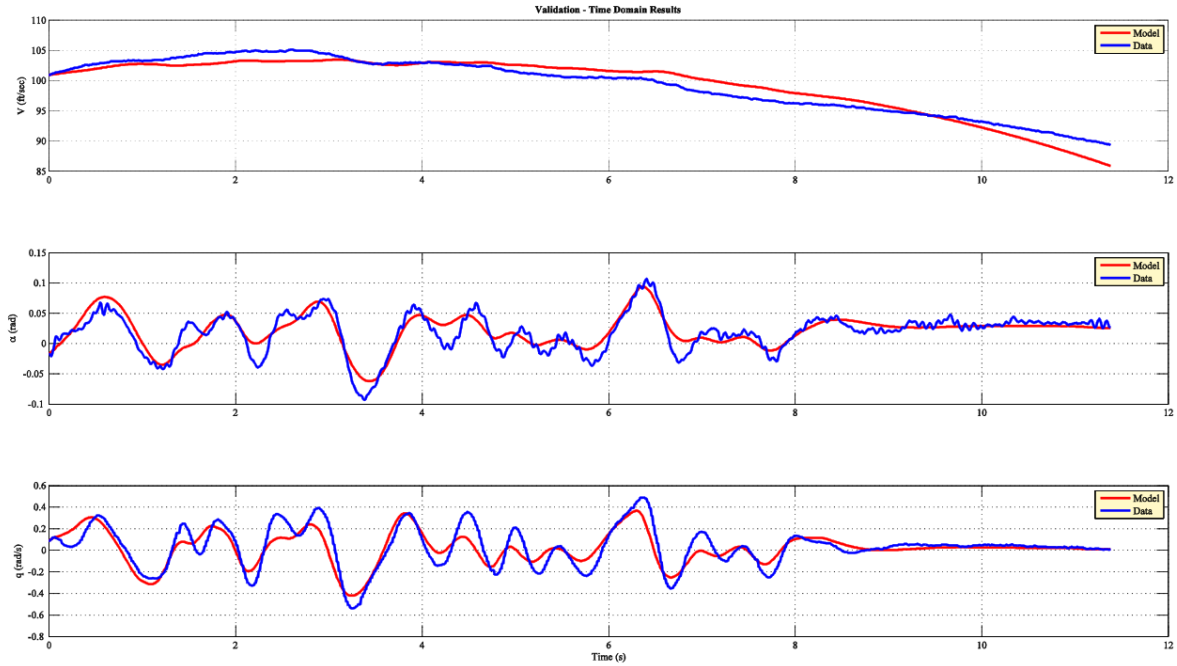

Figure 1.6 – Comparison between flight data and Phastball UAV simulation result (longitudinal)

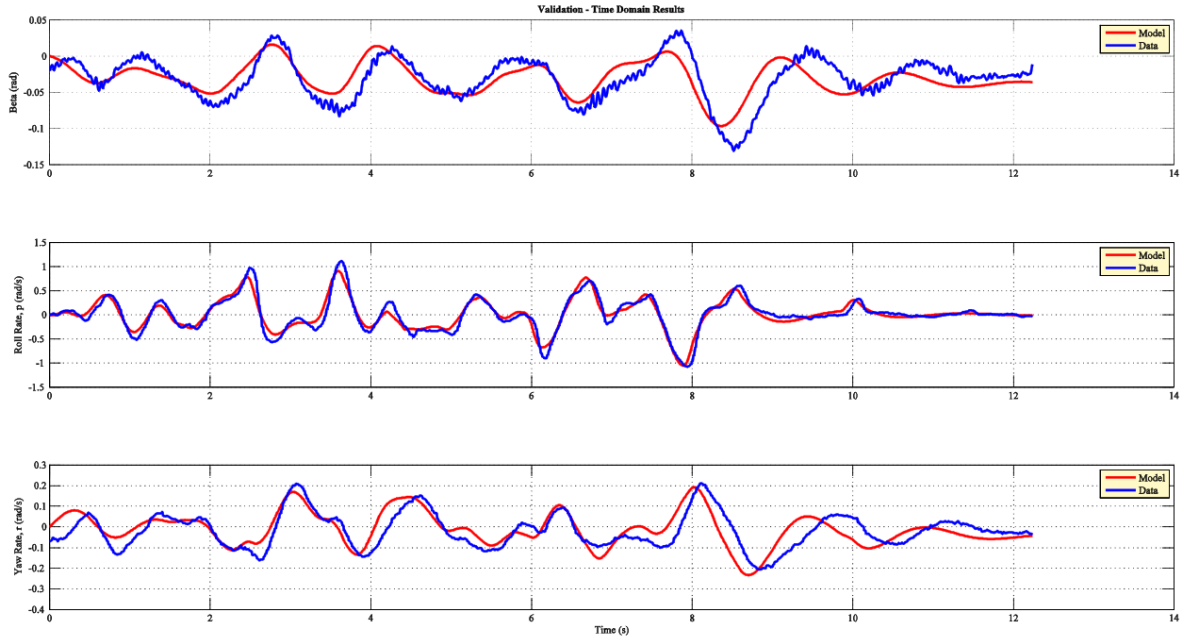

Figure 1.7 – Comparison between flight data and Phastball UAV simulation result (lateral)

1.3 – Formation Flight Using Phastball UAV Simulator

The single-Phastball-UAV simulator was then expanded to support multi-UAV formation flight. The Non Linear Dynamic Inversion (NLDI) based formation controller (*Gu, Y., et. al., 2006; Gu, Y., et. al., 2009*) was developed based upon the mathematical model identified in earlier flight tests. The NLDI based control law is based on a two-loop design, that is an outer loop and an inner loop control laws. The outer loop controller is tasked with trajectory tracking

while the inner loop controller is designed for the attitude tracking. The overall design has been implemented and validated using the PMUS under the 'Virtual Leader' (VL) configuration.

The objective of the formation flight controller is to maintain an 'a priori' defined formation geometry with respect to the 'leader' aircraft along the planar projection of the 'leader' velocity. The formation control problem can be modeled as a non-linear control problem in which a controller acts on throttle, elevator, and aileron/rudder commands to minimize the distance errors *l*, *f*, and *h* with respect to a predefined 'clearance' distance l_c, f_c, and h_c along the 3 axes as shown in Figure 1.8 below.

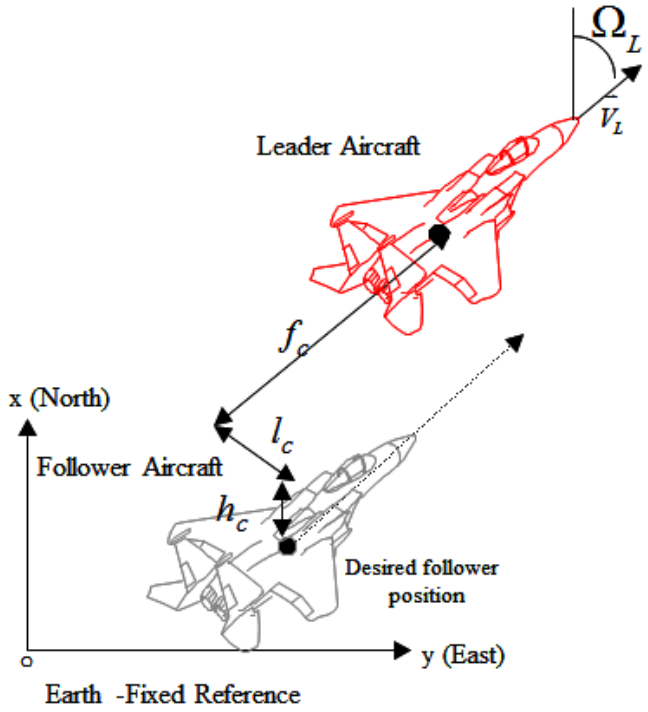

Figure 1.8 – Leader-Follower Formation Geometry

Ultimately the problem reduces itself to the minimization of the following geometric distances:

$$\begin{Bmatrix} l \\ f \\ h \end{Bmatrix} = \begin{bmatrix} \sin(\chi_L) & -\cos(\chi_L) & 0 \\ \cos(\chi_L) & \sin(\chi_L) & 0 \\ 0 & 0 & 1 \end{bmatrix} \begin{Bmatrix} x_L - x \\ y_L - y \\ z_L - z \end{Bmatrix} - \begin{Bmatrix} l_c \\ f_c \\ h_c \end{Bmatrix}$$

With:

$$\sin(\chi_L) = \frac{V_{Ly}}{\sqrt{V_{Lx}^2 + V_{Ly}^2}}$$

$$\cos(\chi_L) = \frac{V_{Lx}}{\sqrt{V_{Lx}^2 + V_{Ly}^2}}$$

The problem can be separated into two decoupled problems, that is horizontal tracking and vertical tracking. Due to the fast attitude dynamics and the relatively slower trajectory dynamics for this problem, the overall controller design is based on an inner loop controller, for pitch and roll angle tracking, and an outer loop controller for lateral-directional and altitude tracking. The overall architecture of the NLDI-based formation flight controller is shown in Figure 1.9, and the inner loop controller is shown in Figure 1.10.

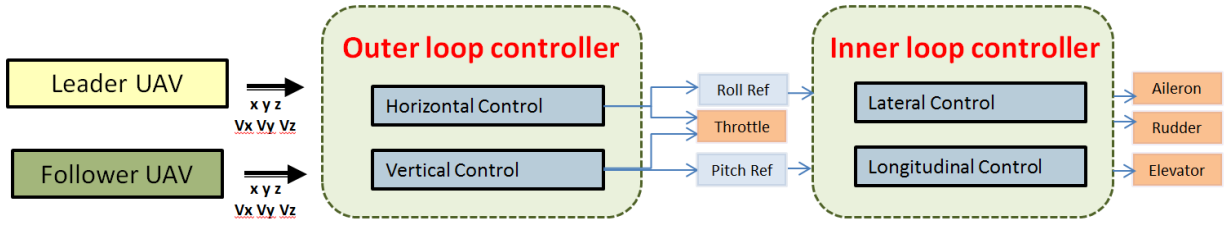

Figure 1.9 – System diagram for NLDI based formation flight controller

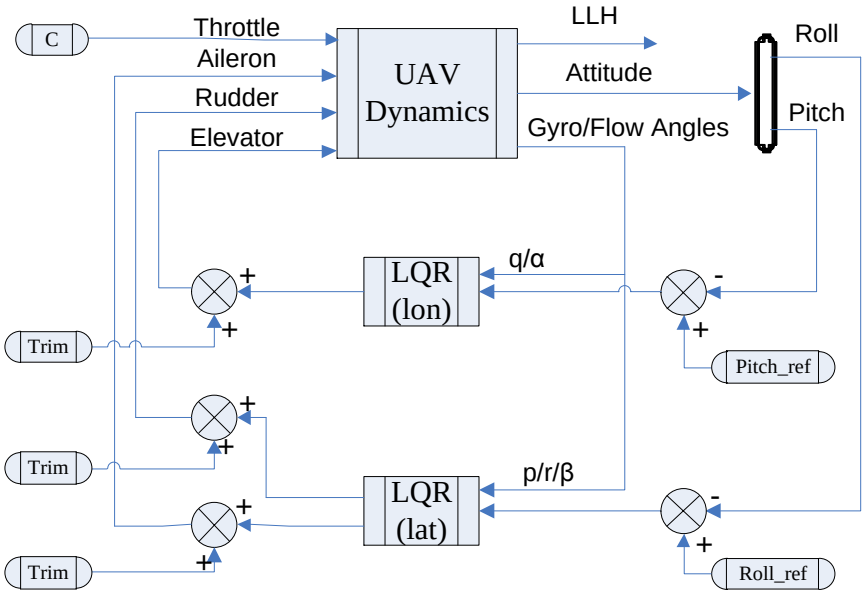

Figure 1.10 – System diagram for inner loop controller (attitude tracking)

The task of the outer loop controller is to generate the desired roll/pitch commands to be fed to the inner loop controller, while the throttle command is provided to the engine directly. The outer loop controller consists of two components, a 'vertical' controller and a 'horizontal' controller. The 'vertical' component is a simple linear altitude controller with the vertical error and its time-derivative as its inputs. The output is the desired pitch angle, which is then provided as a reference signal to the inner loop controller:

$$\theta_d = K_z h + K_{zs}\dot{h}$$

The 'horizontal' component is a nonlinear dynamic inversion (NLDI)-based controller:

$$\phi_d = \arctan\left\{\frac{1}{g\cos\gamma}\left[\ddot{\ell}_d\cos(\chi-\chi_L)+\ddot{f}_d\sin(\chi-\chi_L)\right]\right.$$
$$\left.+\frac{V}{g}\Omega_L+\left[\dot{\ell}\sin(\chi-\chi_L)-\dot{f}\cos(\chi-\chi_L)\right]\frac{\Omega_L}{g\cos\gamma}\right\}$$
$$\delta_T = \frac{m}{K_T\cos\gamma}\left[\ddot{\ell}_d\sin(\chi-\chi_L)-\ddot{f}_d\cos(\chi-\chi_L)\right]$$
$$+\frac{1}{K_T}\left(\frac{1}{2}\rho_0 V^2 S\left(C_{D0}+C_{D\alpha}\alpha_0\right)+m\sin\gamma-T_b\right)$$
$$-\frac{m}{K_T\cos\gamma}\Omega_L\left[\dot{\ell}\cos(\chi-\chi_L)+\dot{f}\sin(\chi-\chi_L)\right]$$

The application of the inputs $[\delta_T, \phi_d]$ has the goal of canceling the non-linearities, leading to:

$$\begin{bmatrix}\ddot{\ell}\\ \ddot{f}\end{bmatrix}=\begin{bmatrix}\ddot{\ell}_d\\ \ddot{f}_d\end{bmatrix}$$

The above system is essentially a linear system consisting of two channels each featuring two integrators in series. This type of system can be controlled using a conventional linear control law; for our specific system, the controller is modeled as:

$$\ddot{\ell}_d = -\tilde{K}_{\ell s}\dot{\ell}-\tilde{K}_{\ell}\ell$$
$$\ddot{\ell}_d = -\tilde{K}_{fs}\dot{f}-\tilde{K}_{f}f$$

Three sets of outer loop controller gains were initialized with root locus approaches, and further fine-tuned through simulations, including the lateral-directional controller gains, the forward distance controller gains, and the vertical controller gains. Additional details on the NLDI-based design for the outer control laws can be found in (*Gu, Y., et. al., 2006*) and (*Gu, Y., et. al., 2009*).

The task of the inner loop control laws is to generate the aileron, elevator, and rudder commands for different roll/pitch reference values from the outer loop controller. The Linear Quadratic (LQ) control law was designed using the identified linear model of the Phastball UAV The controller is designed with the assumption that the longitudinal and the lateral-directional dynamics of the aircraft are decoupled under nominal flight conditions, implying that the dynamics of the vehicle can be expressed by two different linear systems as:

$$\begin{cases}\dot{x}_{lon} = A_{lon}x_{lon}+B_{lon}u_{lon} & x_{lon}=\begin{bmatrix}\alpha & q & \theta\end{bmatrix}^T,\\ \dot{x}_{lat} = A_{lat}x_{lat}+B_{lat}u_{lat} & x_{lat}=\begin{bmatrix}\beta & p & r_f & \phi\end{bmatrix}^T\end{cases}$$

and the control input vectors include elevator for longitudinal direction and ailerons/rudder for the lateral direction. Following the classical LQ controller approach, the control action can then expressed as:

$$\begin{cases}u_{lon} = K_{lon,r}\theta_{ref}-K_{lon,x}x_{lon}\\ u_{lat} = K_{lat,r}\phi_{ref}-K_{lat,x}x_{lat}\end{cases}$$

The NLDI-based formation flight controller has been designed and implemented within the PMUS simulator. Figure 1.11 shows the system structure of an example two-UAV-formation simulation.

The telemetry data collected from a previous flight test was used as the virtual leader, and two Phastball UAVs were configured as the followers for simulation purposes. The Phastball UAV nonlinear model and the NLDI based flight controller are further shown in the right section of Figure 1.11.

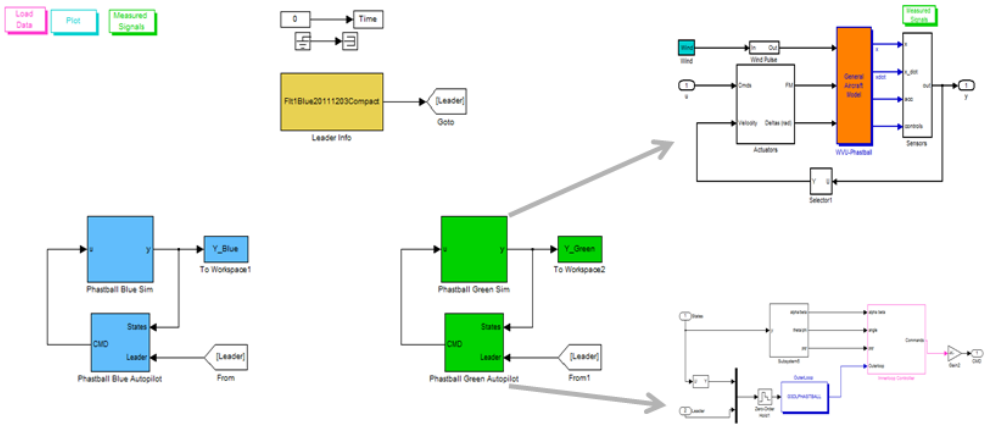

Figure 1.11 - Phastball Multi-UAV Simulator: Two-UAV-Formation

The simulated tracking trajectory for two-UAV-formation is shown in Figure 1.12. The trajectory of the virtual leader is plotted in red while the two followers are plotted in blue and green, respectively. The virtual leader trajectory includes two half circles and two straight legs due to the constraints at the local flight testing facility. It can be seen that the followers could track the leader trajectory and maintain the predefined distance of 20/20/20 meters.

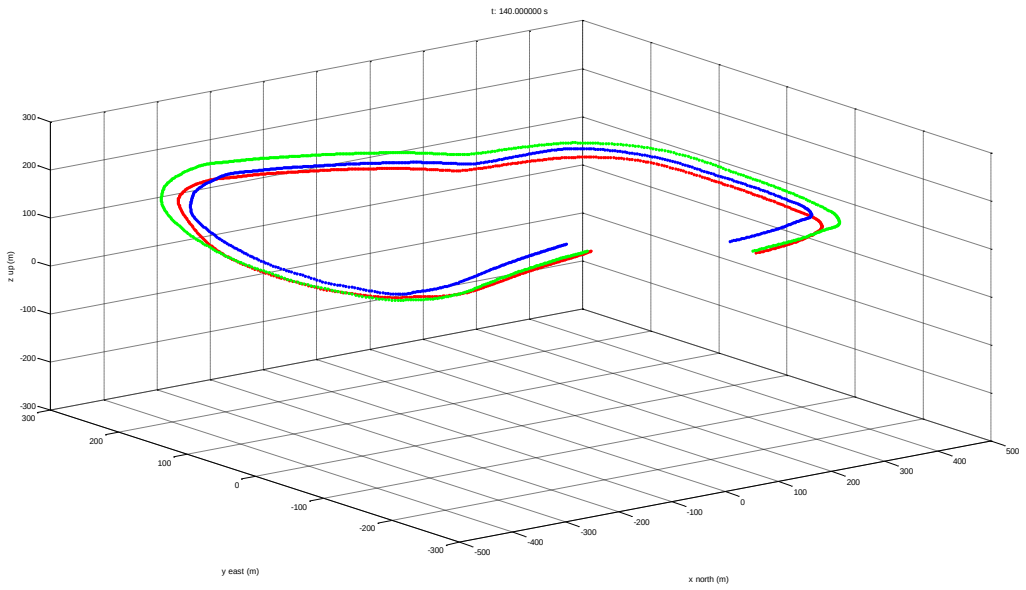

Figure 1.12 – Virtual leader trajectory tracking with 2-UAV formation

Section #2

2. Flight Validation of Multi-UAV Framework & Wake Encounter Tests

Flight test validation of the proposed multi-UAV framework and wind/gust/wake estimation algorithms were among the main objectives of this project. Firstly, onboard sensor fusion algorithms were developed and implemented on the hardware platform to provide high accuracy estimation of attitude and position to support formation flight. Then, the inner loop flight control laws with LQ approach were validated through multiple flight tests. Outer loop flight tests showed reasonable and desirable trajectory tracking performance for formation flights as close as 5 wing span. A detailed analysis of the tracking performance is provided in subsection 3. Finally, the flight results of several wake encounter tests using small UAVs were explained in detail with both smoke visualization plots and onboard sensor measurements.

2.1 – Sensor Fusion for Attitude and Position Estimation

IMU and GPS information were combined to provide a light-weight and low-cost navigation solution using an Extended Kalman Filter (EKF) (*Gross, J., et. al., 2010*). Figure 2.1 illustrates how the GPS position measurement jumps is filtered through the inertial sensors, which in turn improves the formation flight control performance.

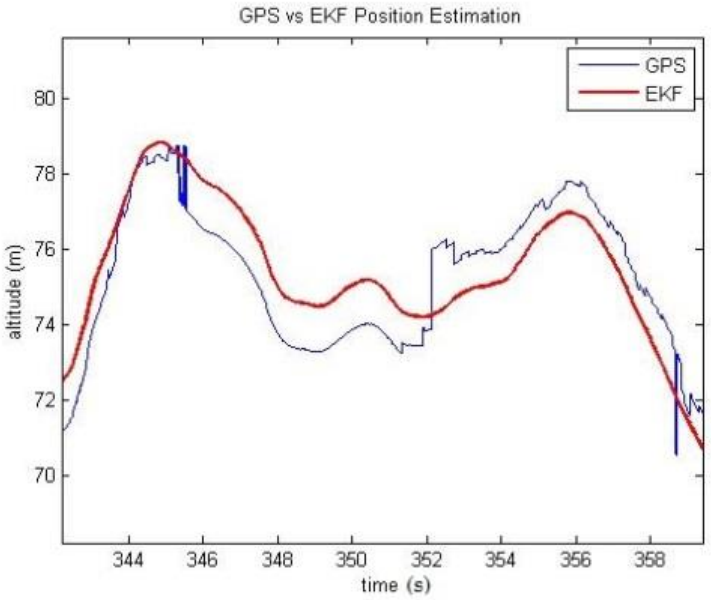

Figure 2.1 – A Comparison of GPS and GPS/INS Position Estimation

The EKF estimates 9 state parameters which are the three-axis position (x, y, z) and velocity (V_x, V_y, V_z,) defined in a local Cartesian frame (L), and attitude angles (ϕ, θ, φ) defined by the aircraft body-axis (B):

$$\mathrm{x} = \begin{bmatrix} x^L & y^L & z^L & V_x^L & V_y^L & V_z^L & \phi^B & \theta^B & \psi^B \end{bmatrix}^T$$

During the state prediction stage, the inertial measurements in terms of three-axis accelerations $\left(\tilde{a}_x^b = a_x^b + v_{ax},\ \tilde{a}_y^b = a_y^b + v_{ay},\ \tilde{a}_z^b = a_z^b + v_{az}\right)$, and three-axis angular rates $\left(\tilde{p}^b = p^b + v_p,\ \tilde{q}^b = q^b + v_q,\ \tilde{r}^b = r^b + v_r\right)$ are integrated to provide an estimate of the state vector x . Each

measurement (e.g. $\tilde{a}_x^b$) is a combination of the true measured parameter (e.g. a_x^b) and a noise term (e.g. v_{ax}). The noise is assumed to be zero mean and normally distributed, with its variance approximated by statistical analyses from static ground tests. The three position states are predicted through direct integration, as represented in discrete-time:

$$\begin{bmatrix} x^L_{k|k-1} \\ y^L_{k|k-1} \\ z^L_{k|k-1} \end{bmatrix} = \begin{bmatrix} x^L_{k-1|k-1} \\ y^L_{k-1|k-1} \\ z^L_{k-1|k-1} \end{bmatrix} + \begin{bmatrix} V^L_{x\ k-1|k-1} \\ V^L_{y\ k-1|k-1} \\ V^L_{z\ k-1|k-1} \end{bmatrix} T_s$$

where T_s = *0.02 s* is the length of the discrete time step. For velocity prediction, the 3D acceleration measurements are integrated and transformed from the aircraft body-axis to the local Cartesian navigation frame:

$$\begin{bmatrix} V^L_{x\ k|k-1} \\ V^L_{y\ k|k-1} \\ V^L_{z\ k|k-1} \end{bmatrix} = \begin{bmatrix} V^L_{x\ k-1|k-1} \\ V^L_{y\ k-1|k-1} \\ V^L_{z\ k-1|k-1} \end{bmatrix} + DCM\left(\phi^B_{k-1|k-1}, \theta^B_{k-1|k-1}, \psi^B_{k-1|k-1},\right) \begin{bmatrix} \tilde{a}^B_{x\ k} \\ \tilde{a}^B_{y\ k} \\ \tilde{a}^B_{z\ k} \end{bmatrix} T_s + \begin{bmatrix} 0 \\ 0 \\ g \end{bmatrix} T_s$$

where DCM is the Direction Cosine Matrix:

$$DCM\left(\phi,\theta,\psi\right) = \begin{bmatrix} c\psi c\theta & -s\psi c\theta + c\psi s\theta s\phi & s\psi s\phi + c\psi s\theta c\phi \\ c\psi c\theta & c\psi c\phi + s\psi s\theta s\phi & -c\psi s\phi + c\psi s\theta c\phi \\ -s\theta & c\theta s\phi & c\theta c\phi \end{bmatrix}$$

'*s*' and '*c*' are abbreviated sine and cosine functions respectively. The aircraft Euler angles are predicted with the 3-axis angular rate measurements:

$$\begin{bmatrix} \phi^B_{k|k-1} \\ \theta^B_{k|k-1} \\ \psi^B_{k|k-1} \end{bmatrix} = \begin{bmatrix} \phi^B_{k-1|k-1} \\ \theta^B_{k-1|k-1} \\ \psi^B_{k-1|k-1} \end{bmatrix} + \begin{bmatrix} \tilde{p}^B_k + \tilde{q}^B_k \sin\phi^B_{k-1|k-1} \tan\theta^B_{k-1|k-1} + r^B_k \cos\phi^B_{k-1|k-1} \tan\theta^B_{k-1|k-1} \\ \left(\tilde{q}^B_k \cos\phi^B_{k-1|k-1} - \tilde{r}^B_k \sin\phi^B_{k-1|k-1}\right) \\ \left[\left(\tilde{q}^B_k \sin\phi^B_{k-1|k-1} + \tilde{r}^B_k \cos\phi^B_{k-1|k-1}\right)\sec\theta^B_{k-1|k-1}\right] \end{bmatrix} T_s$$

The nine predicted state variables are then regulated by the GPS position and velocity measurements during the measurement update process with a simple observation equation:

$$z_k = [\tilde{x}^L_k = x^L_k + v_x \quad \tilde{y}^L_k = y^L_k + v_y \quad \tilde{z}^L_k = z^L_k + v_z$$
$$\tilde{V}^L_{x\ k} = V^L_{x\ k} + v_{Vx} \quad \tilde{V}^L_{y\ k} = V^L_{y\ k} + v_{Vy} \quad \tilde{V}^L_{z\ k} = V^L_{z\ k} + v_{Vz}]^T$$

The solution of the GPS/INS sensor fusion problem follows the classis EKF approach outlined in (*Simon, D., 2006*). The filter tuning is performed through the selection of the process noise covariance matrix *Q* and the measurement noise covariance matrix *R*. Specifically, the process noise is approximated by the sensor-level noise present on the IMU measurement.

$$Q = diag[0 \quad 0 \quad 0 \quad \sigma^2_{v_{ax}} \quad \sigma^2_{v_{ay}} \quad \sigma^2_{v_{az}}]\, T_s^2$$

where the first three zeros indicate that no uncertainty is associated with kinematic equations. Similarly, the variance of the GPS measurement noise calculated with a ground static test is used for providing the *R* matrix:

$$R = diag[\sigma_{v_x}^2 \quad \sigma_{v_y}^2 \quad \sigma_{v_z}^2 \quad \sigma_{V_{V_x}}^2 \quad \sigma_{V_{V_y}}^2 \quad \sigma_{V_{V_z}}^2]$$

2.2 – Formation Controller Implementation

A major advantage of the PMUS simulator is its fairly seamless integration with the Phastball UAV hardware. Both sensing and control schemes are implemented using MATLAB S functions, which can be easily converted across hardware platforms. Once a scheme is validated through the PMUS simulator, the controller or estimator block can be directly dragged to the flight scheme for the creation of the executable file (Linux RTAI). The compilation procedure of the flight scheme is shown in the general block shown in Figure 2.2. An example of a flight scheme is shown in Figure 2.3. The overall scheme structure is displayed in the upper left sub-figure of Figure 2.3 with its two major functions, that is sensing and flight control. The sensing block is for the telemetry logging, sensor calibration, and real-time state estimation (EKF), shown in the lower sub-figure of Figure 2.3. The controller block takes in the data from the sensing block and sends out PWM commands to the control surfaces.

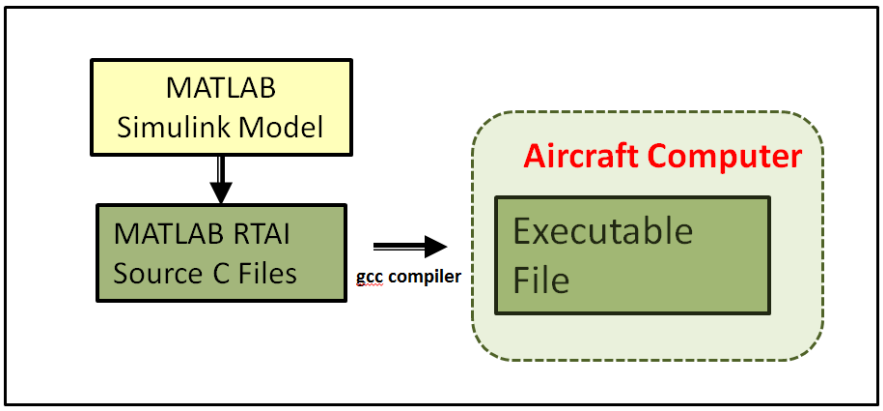

Figure 2.2 – Flight scheme compilation procedure for Phastball UAV

Multiple flight schemes have been created for the task of inner loop attitude tracking. The initial controller gains were derived through LQ design and tuned through a series of flight tests converging to the following set of controller gains for the Blue Phastball:

$$K_r^{lon} = [-0.6325]$$

$$K_x^{lon} = [-0.0991, -0.1308, -0.6325]$$

$$K_r^{lat} = [-0.5413, -0.0147]^T$$

$$K_x^{lat} = \begin{bmatrix} -0.1665 & 0.045 & 0.0413 & 0.5385 \\ -0.0827 & 0.0076 & 0.1708 & 0.1171 \end{bmatrix}$$

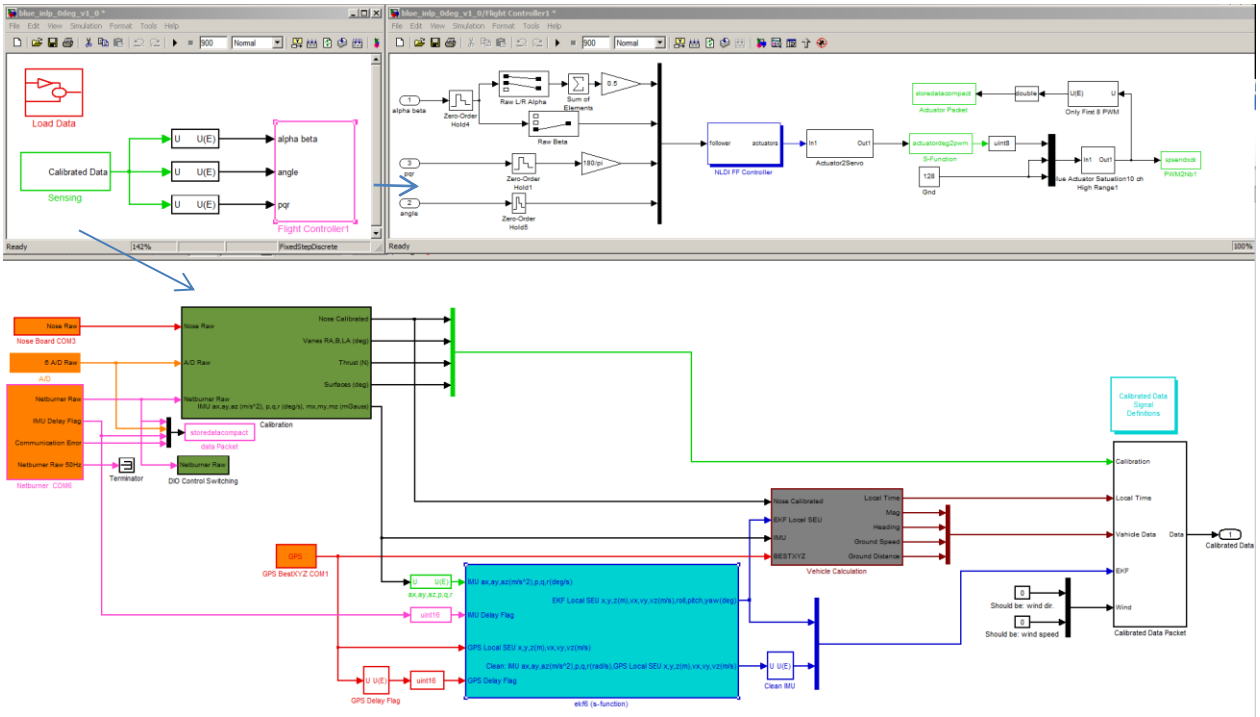

Figure 2.3 – Software scheme of outer loop flight controller for Phastball UAV

The inner loop tracking performance for one example flight is shown in Figure 2.4. A series of desired roll/pitch commands are generated using the joystick to simulate the outputs from outer loop flight controller to show the effectiveness of the attitude tracking performance.

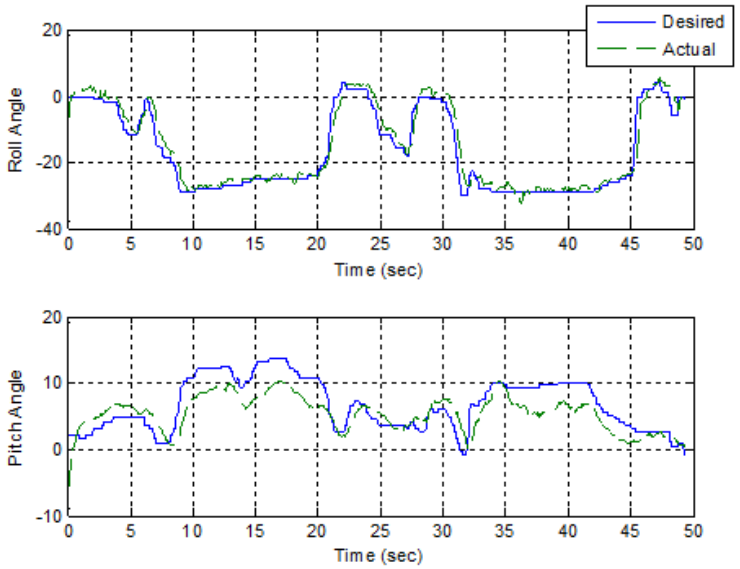

Figure 2.4 – Flight performance of inner loop flight controller for Phastball UAV

The outer loop flight control laws have also been implemented within a virtual leader approach. In other words, a preplanned virtual leader trajectory was created for the Phastball UAV to follow. The outer loop controller gains were found to be:

$$K_{fs} = 1.2, K_f = 0.45;$$

$$K_{ls} = 1.7, K_l = 0.6;$$

$$K_{vs} = 0.8, K_v = 1.3;$$

2.3 – Formation Flight Testing Results

The validation of the fully developed formation flight controller was conducted first with a 'virtual leader' setup, where the follower aircraft would follow a pre-recorded leader aircraft's GPS trajectory. Later, flight tests were conducted using a physical leader aircraft and a follower aircraft.

Three 2-aircraft formation flights and seven 2-aircraft close formation flights (with a separation at around 5 wingspans) were performed in the 2013 flight testing season. The leader aircraft maintained an oval flight path over the airfield. Once the aircraft achieved an approximate 'rendezvous', the formation flight control laws were activated and the follower maintained formation as shown in figure 2.5. Figure 2.6 shows the leader and follower in flight.

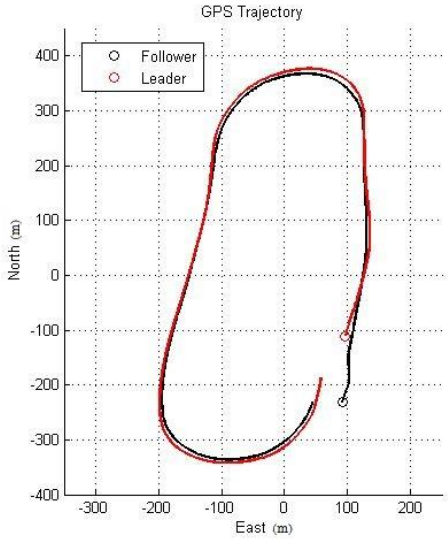

Figure 2.5 – Oval Flight Path of a Single Lap in Formation

Figure 2.6 – Aircraft Demonstrating Close Formation Flight

Out of a total six flight experiments, only flight #1, #2, #3, and #5 were suitable for steady state error analysis. Flights #4 and #6 were conducted instead with variable formation geometry to evaluate transient behaviors. Figure 2.7 shows the trend of the errors on the 3 axis over the course of a single lap.

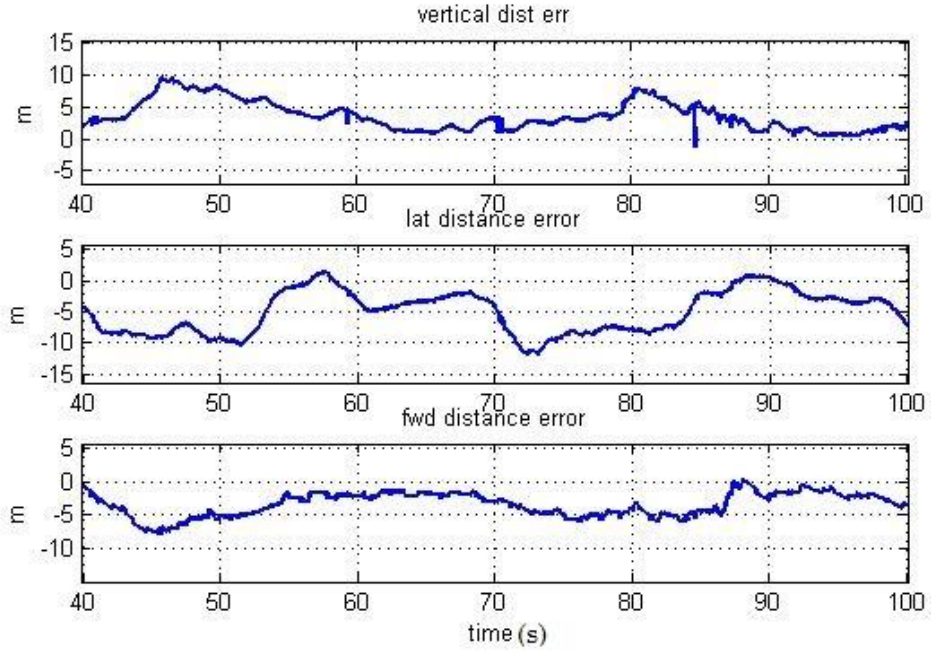

Figure 2.7 – Formation Flight Errors of a Single Lap

The transient response, shown in Figure 2.8 for the forward distance error, is characterized for all dimensions in Table 2.1. In Figure 2.8, the desired forward clearance decreased from 27m to 12m within approximately about 21 seconds.

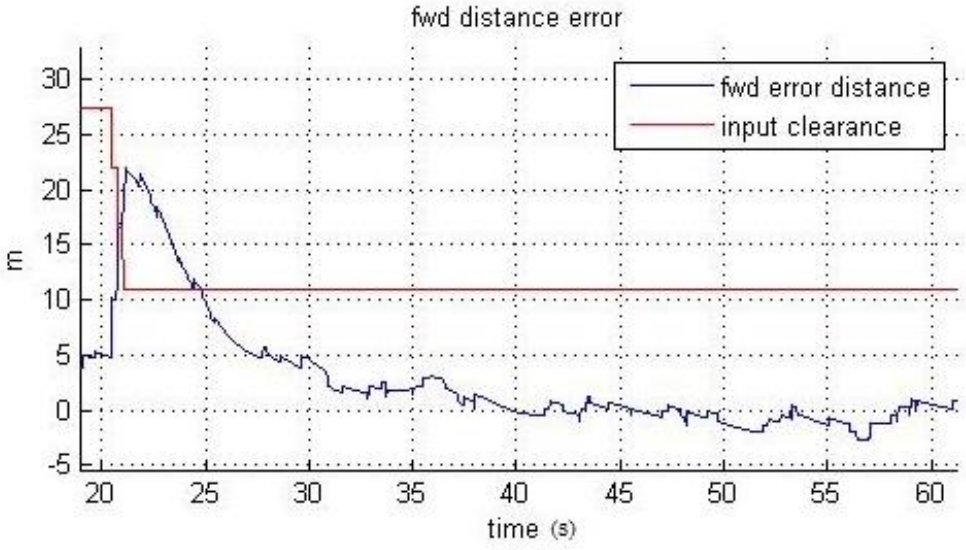

Figure 2.8 – Transient Response in Forward Distance Error

The steady state error analyses are shown for the straight legs and turning in Tables 2.2 and 2.3 respectively. It should be emphasized that the steady state error calculation does not consider GPS errors, which are rated for 1.5m RMS, but could occasionally reach much higher values during the flight.

TABLE 2.1 - TRANSIENT BEHAVIOR FROM THE INITIATION OF FORMATION FLIGHT

Transient Behavior		Init. Err. Distance (m)	T react (s)	T peak (s)	T rise (s)	T settling (s)	OS%
	Vrt	-26.18	1.18	3.52	2.45	2.91	12.50%
	Lat	28.69	2.79	n/a	4.30	5.11	n/a
Flight 1	Fwd	65.48	8.22	n/a	14.24	16.91	n/a
	Vrt	0.16	0.61	0.96	0.04	2.38	116.61%
	Lat	10.85	2.44	4.86	2.53	11.10	60.82%
Flight 2	Fwd	78.30	6.57	18.84	12.00	14.25	9.19%
	Vrt	-3.34	0.29	1.14	0.37	0.44	49.70%
	Lat	-15.55	8.18	12.82	9.50	11.29	4.00%
Flight 3	Fwd	71.25	8.34	20.14	13.82	15.46	4.41%
	Vrt	--	--	--	--	--	--
	Lat	-31.17	1.54	3.52	1.60	1.90	62.61%
Flight 4	Fwd	7.57	2.56	n/a	12.88	15.30	n/a
	Vrt	10.00	6.00	7.96	5.06	7.44	2.48%
	Lat	-6.54	5.38	n/a	3.41	4.05	n/a
Flight 5	Fwd	5.43	0.73	3.36	0.93	1.10	40.19%
	Vrt	-8.99	0.93	1.98	1.10	--	18.77%
	Lat	5.84	2.75	6.64	2.67	30.36	63.93%
Flight 6	Fwd	81.00	10.28	17.96	12.99	15.43	2.62%

TABLE 2.2 - PERFORMANCE OF THE PHASTBALL 2-AIRCRAFT FORMATION FLIGHT DURING THE STRAIGHT LEGS

FF Straight legs		Clearance	Max Err. Distance	Mean Abs. Err. Distance	Mean Err. Distance	Std. Dev.	avg. % wing span
	Forward (m)	50	-6.112	2.623	-2.356	1.896	98.17%
Flight	Lateral (m)	0	-5.615	2.011	-1.628	1.985	67.83%
1	Vertical (m)	0	4.778	2.617	2.617	0.993	109.04%
	Forward (m)	40	-3.6999	2.1435	-2.1435	0.5388	89.31%
Flight	Lateral (m)	0	-8.4467	2.8026	-2.6397	1.8898	109.99%
2	Vertical (m)	0	5.973	2.7304	2.7304	1.3327	113.77%
	Forward (m)	30	-2.281	0.798	-0.7443	0.5524	31.01%
Flight	Lateral (m)	0	-5.4955	1.7245	-1.3809	1.3803	57.54%
3	Vertical (m)	0	6.3215	2.3565	2.3565	1.0408	98.19%
	Forward (m)	12	2.0679	0.5332	0.4939	0.4857	20.58%
Flight	Lateral (m)	0	-1.8902	1.1925	-1.0496	0.695	43.73%
5	Vertical (m)	2.4	3.0881	2.3906	2.3906	0.3856	99.61%
	Forward (m)	12	1.8985	0.6487	-0.4989	0.5958	20.79%
Flight	Lateral (m)	1.2	0.5507	0.1838	-0.0212	0.2382	0.88%
7	Vertical (m)	2.4	2.2287	1.6403	1.6403	0.2121	68.35%
	Forward (m)	12	1.5292	0.5356	-0.1432	0.5955	5.97%
Flight	Lateral (m)	1.2	1.0828	0.6056	-0.6056	0.2251	25.23%
8	Vertical (m)	2.4	2.0269	1.3024	1.3024	0.3271	54.27%
	Forward (m)	12	3.5632	1.7632	-1.5206	1.2385	63.36%
Flight	Lateral (m)	1.2	0.386	0.1285	-0.0232	0.157	0.97%
10	Vertical (m)	2.4	2.3495	1.6959	1.6959	0.3679	70.66%
	Forward (m)	12	2.4633	1.1678	-0.9037	1.0197	37.65%
Flight	Lateral (m)	2.4	1.6007	0.6302	-0.6302	0.4694	26.26%
11	Vertical (m)	2.4	1.1452	0.4337	-0.34	0.3974	14.17%
	Forward (m)	12	2.6368	1.5098	-1.5098	0.787	62.91%
Flight	Lateral (m)	2.4	1.0408	0.619	-0.619	0.28	25.79%
12	Vertical (m)	2.4	1.8147	1.2932	1.2932	0.3173	53.88%
	Forward (m)	12	2.6857	1.5422	-1.5255	0.7487	63.56%
Flight	Lateral (m)	2.4	0.7949	0.2144	-0.1482	0.2856	6.18%
13	Vertical (m)	2.4	1.8852	1.545	1.545	0.1369	64.38%

TABLE 2.3 - PERFORMANCE OF THE PHASTBALL 2-AIRCRAFT FORMATION FLIGHT DURING TURNS

FF Straight legs		Clearance	Max Err. Distance	Mean Abs. Err. Distance	Mean Err. Distance	Std. Dev.	avg. % wing span
Flight 1	Forward (m)	50	-12.475	5.650	-7.177	5.220	299%
	Lateral (m)	0	-22.371	8.048	-12.949	5.437	540%
	Vertical (m)	0	9.051	4.209	5.481	2.247	228%
Flight 2	Forward (m)	40	-5.968	3.300	-4.788	0.641	200%
	Lateral (m)	0	-11.773	5.251	-8.406	1.606	350%
	Vertical (m)	0	7.942	3.327	4.091	1.805	170%
Flight 3	Forward (m)	30	-5.010	1.713	-2.940	0.649	123%
	Lateral (m)	0	-7.350	3.211	-5.198	1.865	217%
	Vertical (m)	0	12.051	4.107	6.452	2.673	269%
Flight 5	Forward (m)	12	1.986	0.762	0.729	0.445	30%
	Lateral (m)	0	3.438	2.394	2.394	0.524	100%
	Vertical (m)	0	9.485	3.960	3.960	1.052	165%
Flight 7	Forward (m)	12	2.951	1.863	1.863	0.445	78%
	Lateral (m)	0	4.177	3.180	3.180	0.469	132%
	Vertical (m)	0	6.812	4.265	4.265	1.380	178%
Flight 8	Forward (m)	12	6.059	3.431	3.431	1.307	143%
	Lateral (m)	0	4.402	3.836	3.836	0.221	160%
	Vertical (m)	0	8.423	5.994	5.994	1.015	250%
Flight 10	Forward (m)	12	3.338	0.949	0.818	0.885	34%
	Lateral (m)	0	4.512	3.561	3.561	0.479	148%
	Vertical (m)	0	11.391	8.718	8.718	1.585	363%
Flight 11	Forward (m)	12.00	3.401	0.972	0.955	0.904	40%
	Lateral (m)	2.40	6.449	4.878	4.878	0.660	203%
	Vertical (m)	2.40	5.019	3.811	3.811	0.960	159%
Flight 12	Forward (m)	12.00	2.030	0.777	0.567	0.753	24%
	Lateral (m)	2.40	4.778	4.264	4.264	0.412	178%
	Vertical (m)	2.40	13.094	10.773	10.773	2.187	449%
Flight 13	Forward (m)	12.00	2.492	1.082	0.747	1.152	31%
	Lateral (m)	2.40	5.584	4.719	4.719	0.557	197%
	Vertical (m)	2.40	7.298	5.454	5.454	1.032	227%

Along the straight portions of the loop, the average magnitude of mean distance error from Table 2.3 is 3.43 meters with a standard deviation of less than 2 meters. However, in the turns, the average magnitude of the mean distance error from Table 2.4 increases to approximately 10 meters with a standard deviation of approximately 3 meters. Table 2.4 displays the proximity between the leader and follower to give a better analysis of the formation flight performance.

TABLE 2.4 - PROXIMITY BETWEEN LEADER AND FOLLOWER DURING FORMATION FLIGHT

Aircraft Proximity During FF							
		Straight legs			Turns		
	Clearance (m)	Max (m)	Min (m)	Average (m)	Max (m)	Min (m)	Average (m)
Flight 1	50	51.791	44.245	48.018	54.963	40.485	47.724
Flight 2	40	38.896	36.958	37.927	38.473	34.936	36.705
Flight 3	30	31.104	27.799	29.451	30.979	27.002	28.990
Flight 5	12.24	16.407	14.434	15.421	22.520	14.481	18.500
Flight 7	12.30	15.275	13.558	14.417	20.815	15.535	18.175
Flight 8	12.30	15.057	12.875	13.966	23.567	13.423	18.495
Flight 10	12.30	16.582	13.332	14.957	24.995	18.625	21.810
Flight 11	12.47	15.624	12.480	14.052	21.322	16.642	18.982
Flight 12	12.47	15.837	13.260	14.549	26.556	19.696	23.126
Flight 13	12.47	15.847	13.740	14.793	21.992	17.651	19.821

It is worth mentioning that formation flight was previously demonstrated with the WVU YF-22 aircraft (*Gu, Y., et. al., 2006*) where the magnitude of the mean distance error was found to be 13.52 for a circular flight pattern. The WVU Phastball platforms performed significantly better than the YF-22 during turning (with similar clearance values of about 30m). Known factors which contributed to this improvement are the use of electric motors, which are substantially more responsive than the gas turbines used on the WVY YF-22, the use of improved and more accurate avionics, state estimation, as well as an extensive effort in tuning the control gains for the WVU Phastball.

As expected, the controller performs better during straight flight than turning. Having the horizontal and vertical dimensions decoupled limits the tracking capabilities when the leader enters a turn or a climb. The design could be improved by deriving the 3D formation control laws without decoupling the vertical and horizontal components.

The benefits of formation flight can only be enjoyed if aircraft are precisely controlled. This experiment will contribute to the future of close formation flight research for energy saving and improved air traffic management.

2.3 – Wake Encounter Test Using UAV Formation

Two types of wake flight tests were performed during the project efforts. The first effort focuses on the initial feasibility validation of using subscale aircraft for wake encounter test. A Remote Controlled (RC) model airplane with smaller dimensions than the Phastball was used for the wake visualization test when flying through generated smokes. After the initial validation, WVU Phastball UAVs were flown in close tandem formation (about 5 wingspan) for wake encounter test. Onboard sensor measurements clearly showed the detection of wake vortices generated by the leading aircraft.

Wake Visualization Using a Model Airplane

Wake visualization is a straight forward process in order to physically see the wake behind a small UAV. Smoke bombs were set off during flight tests and a small model airplane with an attached camera was flown through the smoke. Figure 2.9 shows the wake produced as the model airplane when flying through the edge of the smoke cloud.

Several observations can be made from the analysis of the image and the recorded ground/onboard video. First, the center of each vortex does not have any smoke which shows that the influence of the vortex goes to zero at the core of the wake. It can also be seen through video data that the wake continues to spin for quite some time without a substantial loss of altitude. This observation validates the small descent speed assumption used in the modeling of the Phastball wake simulation, which is described in detail in Section 3. In addition, the observable size of the vortices are on the order of approximately a third of the wingspan and do not seem to affect each other. Finally, although the two well defined counter rotating vortices can be easily observed behind the model airplane, it seems that the air directly behind the aircraft is barely, if at all, affected by the wingtip wake vortices.

Figure 2.9 - Wake visualization using a RC model airplane

Wake Encounter Test with Phastball UAV Formation Flight

As mentioned flight testing was conducted with two Phastball UAVs in formation flight during wake encounter tests. Multiple wake encounters were observed during several close formation flights. Two representative set of onboard measurements were illustrated, shown in Figure 2.10 and 2.11.

Multiple two-aircraft formation flights were performed with the follower's nose directly behind the wing tip of the leader. The initial formation geometrics are set at 5 wingspans in the forward direction, 0 wingspans in the vertical direction, and half a wingspan in the lateral direction. It is worth mentioning that the formation control laws were modified so that the ground pilot could adjust the formation geometrics in real time for more chances of wake encounters under different wind conditions.

Figure 2.10 and 2.11 show representative measurements of multiple abrupt encounters between the follower UAV and the leader's wake. It can be observed from Figure 2.10 that the right vane encountered the downwash of the wake and then quickly hit the upwash of the wake. Approximately half a second after the vanes sensed the wake, the longitudinal dynamics show the wake encounter as well through acceleration and pitch measurements. The UAV experienced an acceleration of 4 m/s^2 to almost -5m/s^2, which is essentially a change of almost 1 g in about a 1.5 second. This level of variation in acceleration could easily be felt by passengers for a commercial aircraft.

Figure 2.11 shows a similar wake encounter where in this case the left AoA vane encountered the upwash of the leader's wake with an AoA measurement of more than 9 deg. The interesting difference in this encounter is that there is a much longer residual effect of the wake on the AoA vane, as it takes nearly 0.5 second for the vane to return to similar readings of the right vane. In this case, the upwash causes a slight increase in the pitch of the aircraft starting again approximately 0.5 second after the vane initially sensed the wake. Most likely due to the short duration of the encounter and also due to the fact that the rest of the UAV is under effects

from the wake and atmosphere, there is no much evidence of the wake shown in the accelerometer data.

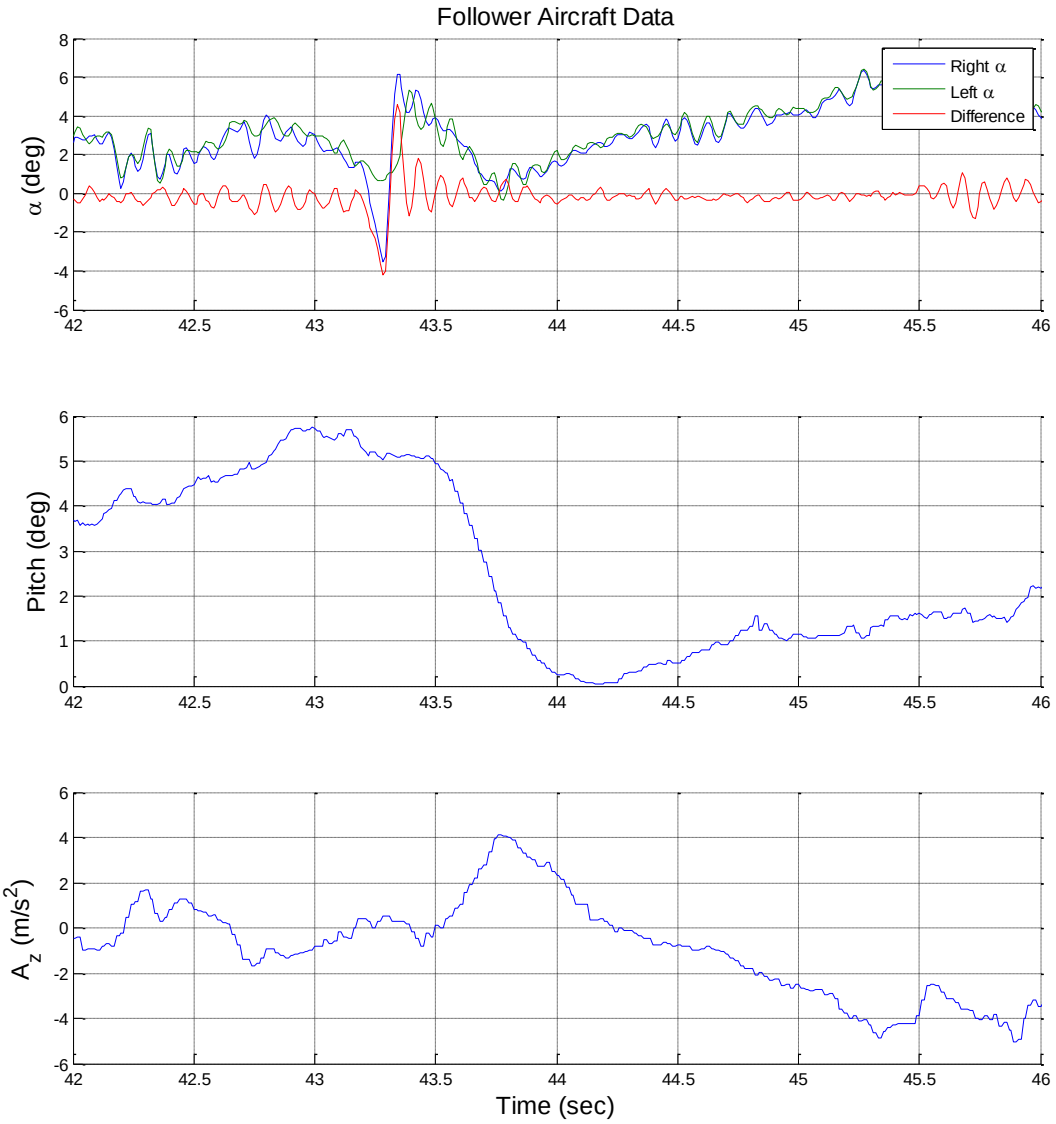

Figure 2.10 – Follower onboard measurements during wake encounter test (1)

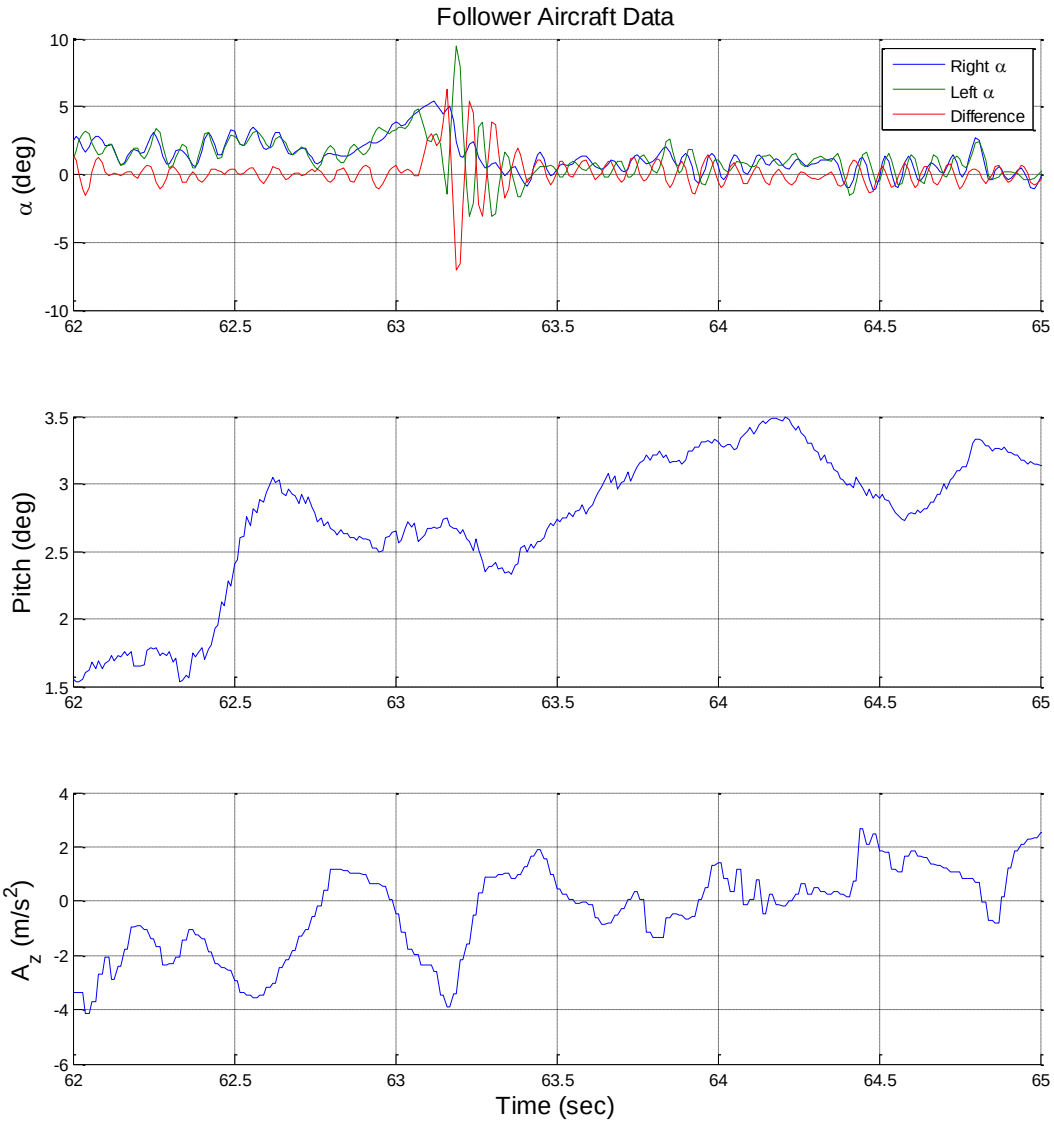

Figure 2.11 - Follower onboard measurements during wake encounter test (2)

Through close formation flights, the generated downwash and upwash can be sensed by the airflow vanes on the left/right side of the Phastball, as the follower flies through the leader's wake. Additionally, the accelerometer will sense the aircraft being pushed by the induced wind, and the pitch angle will change as the follower falls in a region of upwash or downwash. It is interesting to point out that the follower UAV is under control to maintain a formation with the leader; therefore, as the wake causes variations in the pitch and roll of the aircraft, the formation control laws try to compensate these changes. Similarly, the effects of wake encounters of Phastball UAVs tend to be short because the aircraft flight controller will try to cancel out disturbances such as wake encounters. Therefore, the net result is that the effects of the wake on

the follower are not as pronounced as it could be if the UAV was allowed to fly through the wake in an open-loop mode.

It is interesting to observe that often the wake is only sensed by one of the two AoA vanes. Clearly, during steady level flight and in the absence of wake effects or variable wind conditions, the difference between the two vanes should be negligible. This could be due to the fact that the two AoA vanes are installed on the left and right side of the fuselage. The front part of the aircraft could shade the vanes from the wake effects. More importantly, the wake of Phastball UAV is relatively small and it is very challenging to hit the wake with both vanes simultaneously. In fact, the distance between the two AoA vanes is approximately the same as the detectable size of the vortex core (with vertical wind components around 1 m/s).

In summary, the above flight results showed the feasibility of using sub-scale aircraft for wake encountering tests and visualizations. The quantification of wake encounter measurements as well as the identification of the Phastball UAV wake model are still undergoing. They are among the objective of the planned efforts for Phase II of the project.

Section #3

3. Wind/Gust Sensing and Suppression Control Using Small UAVs

The accurate estimation of prevailing wind and gusts was another critical goal of the project. The '*one minus cosine*' gust model and Phastball wake model were first introduced for the simulation purposes. Two nine state Unscented Kalman Filters (UKF) were designed and implemented for the wind gust estimation with and without using the wake information from the leader aircraft. The UKF was selected for this study due to its flexibility of implementation without requirements for calculation of computationally intensive Jacobian matrices. Early results have shown the accurate estimation of prevailing wind using collected flight data (*Rhudy, M., et. al., 2013*). The UKF is further extended to the gust case with the PMUS simulator for single aircraft operations. For leader-follower flights, a cooperative UKF is proposed for the follower aircraft by incorporating the wake information as part of the measurement equations. Simulation results showed the improvement of the estimation results using the cooperative UKF. Finally, preliminary gust suppression controllers are proposed based from the developed wind/wake sensing algorithms.

3.1 – Wind/Wake Modeling & Simulation for Phastball UAVs

For simulations used in wind estimation and wake modeling, it is important to have a wind model that accurately models wind gusts occurring during flight testing. A model that is often used for its simplicity is the 'one minus cosine' idealization. Each individual gust consists of a '*cosine*' pulse, shown in Figure 3.1 below, where U_0 is the amplitude of the idealized wind gust. The frequency and magnitude of the gust model can be selected accordingly based on the user requirements.

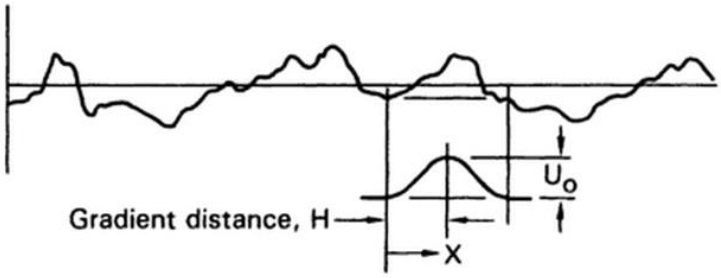

Figure 3.1 – 'One-minus-cosine' gust idealization (*Hoblit, F.M., 2001*)

Wake modeling is a critical task for the verification of the wake sensing. This task can be performed using various models. Wake modeling essentially consists in calculating the circulation strength and core size of the wake and then calculating the effects the wake has on the following aircraft. The method described in this section assumes the induced wind is acting only at the CG of the follower aircraft. In future studies it is envisioned to expand to multiple points about the aircraft which can then be averaged to find a more accurate representation of the effect of induced wind.

In this effort, the selected wake model was the Hallock Burnham vortex (*Gertz, T., et. al., 2002*). The induced wind at any point away from the wake can be calculated using the following equations:

$$\Gamma_0 = \frac{mg}{\rho S b V}$$

$$R_c = 0.05b$$

$$v_\theta(r) = \frac{\Gamma_0}{2\pi R}\frac{R^2}{R^2 + R_c^2}$$

where Γ_0 is the root circulation, *m* is the mass of the UAV, g is the gravitational constant, ρ is the air density, *S* and *b* are the wing area and the wing span respectively, v is the velocity, and v_θ is the induced wind velocity at a particular distance *R* from the root core that has a radius of R_c. Figure 3.2 shows a sketch of the wake behind an aircraft, which shows two counter-rotating vortexes trailing the wing tips. The sketch also shows that disturbances in the atmosphere due to the deflection of various aircraft control surfaces are pulled into these two main vortex pairs.

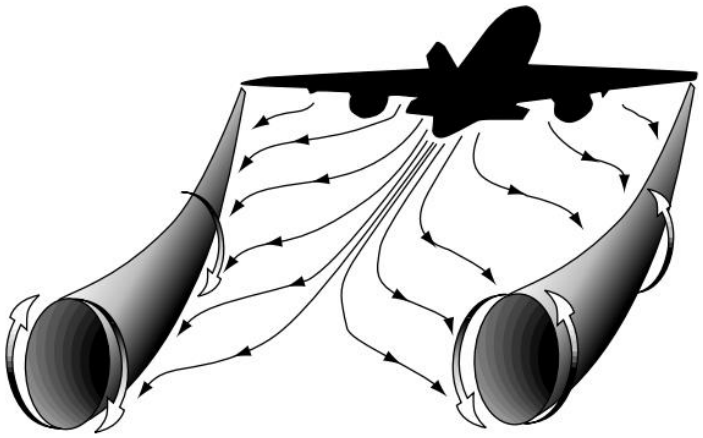

Figure 3.2 - Wake model sketch (from faa.gov website)

It is also important to model how the wake moves and decays over time as function of the distance x from where the wake was generated. This relationship is described by the following equations from the Sarpkaya decaying model (*Sarpkaya, T., 2000*):

$$\omega_0 = \frac{\Gamma_0}{2\pi b_0}$$

$$\Gamma(x) = \frac{\Gamma_0 \; e^{(-0.45\, x\, \tau\, \Gamma_0)^{0.25}}}{\rho V b}$$

where ω_0 is the descent speed and b_0 is half the wing span of the UAV. The term $\Gamma(x)$ models the decay of the vortex as a function of x where τ is the amount of turbulence in the atmosphere (in this study assumed to be light turbulence since flight testing was conducted in calm weather conditions).

Finally, the induced velocity can be converted to the inertial frame using the equation:

$$\begin{bmatrix} V_E \\ V_D \end{bmatrix} = \begin{bmatrix} -v_\theta \sin(\varphi) \\ v_\theta \cos(\varphi) \end{bmatrix}$$

where $[V_E, V_D]^T$ is the velocity in East and Down directions induced on the follower from the leader's wake and φ is the angle about which the follower is rotated about the wake of the leader. The values of all the constant terms in each of the above equations are reported in **Table** .

Table 3.1 Constants used in wake modeling

Variable	Description	Value	Units
R_c	Root Core	0.0912	m
Γ_0	Root Circulation	1.72	m^2/s
b	Wing Span	2.4	m
S	Wing Area	0.73	m^2
m	Mass	11	kg
g	Gravitational Constant	9.81	m^2/s
ρ	Air Density	1.2727	kg/m^3
ω_0	Descent Velocity	0.156	m/s
τ	Light Turbulence Level	0.003	N/A

Figure 3.3 shows the induced vertical velocity from the Phastball UAV using the previously introduced equations. Only the vertical velocity is shown here because the vertical component is important for energy harvesting purposes when flying in formation.

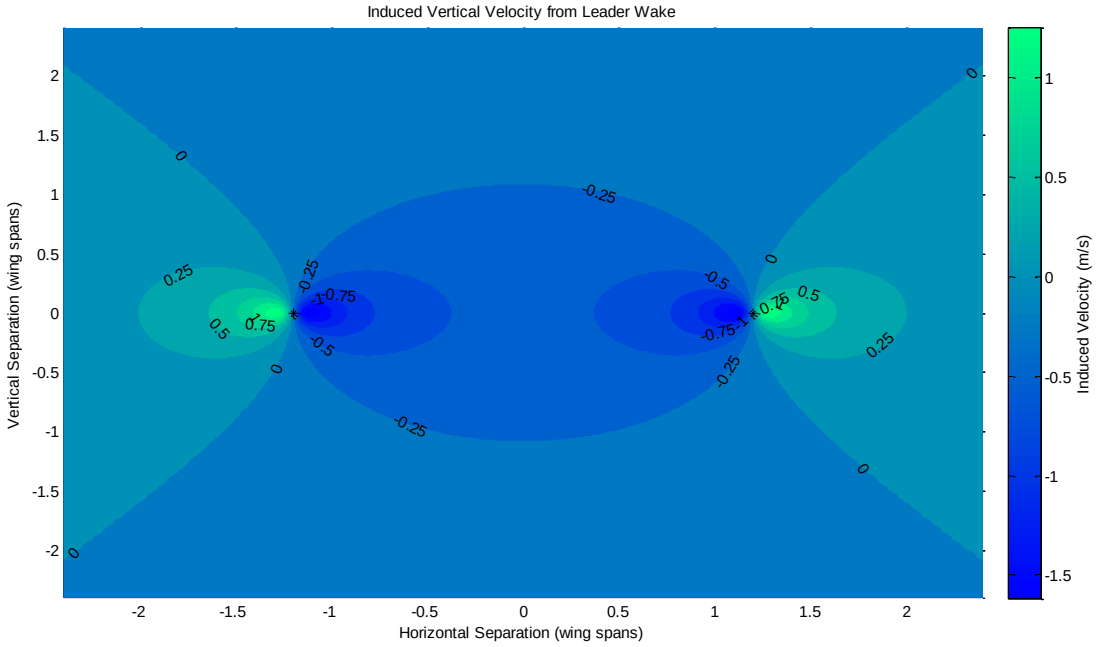

Figure 3.3 - Induced vertical velocity from the wake of the Phastball UAV

Finally, it is important to emphasize two key aspects of the wake. First, the wake will roll up in the near field (anywhere between 5-15 wingspans), followed by a stable vortex pair in the near field (between 15 to 150 wingspans). It is assumed that the wake will maintain its core radius and strength for locations between 5 to 30 wingspans for the application to small UAVs. This is due to the relatively slow descending velocity and the flow evolution of wake vortices generated by

small UAVs. Also, the wake will flow parallel to the aircraft velocity vector which will affect the position of the wake.

3.2 – Wind Gust Estimation Using Small UAVs

The proposed UKF algorithms for single UAV and multiple UAV application were explained in detail in this subsection. First, the air data system of Phastball UAVs is introduced together the ground weather station for validation purposes. Then, a new UKF was proposed for the wind estimation using onboard measurements from small UAVs. Flight test data showed a good match between UKF estimates and predictions from ground weather stations. Finally, the cooperative UKF is proposed and simulated to show its advantages over the UKF for single-UAV scenarios.

3.2.1 - Measuring Hardware

A nose board was custom designed and manufactured by FCSL researchers for the Phastball UAV platform for collecting air speed and flow angle data. A Netburner Mod5213 is used as the main processor which powers the sensors in the nose and collects the data which is sent to the flight computer. Three low-friction inductive potentiometers are used for the measurement of left and right angle of attack as well as the sideslip angle. Two sensors from Sensor Technics measure static and differential pressure. These pressure sensors were selected with the requirements of a 2000 meter flight ceiling and a maximum flight speed of 60 meters per second. To collect data, corresponding firmware was developed which communicates via Serial Peripheral Interface (SPI) protocol with the pressure sensors at 400 Hz. To reduce the effects of noise, an average filter is running every eight samples in order to get an average value of both differential and static pressure data; therefore, the data outputs at 50 Hz. A Pitot tube is used to connect the pressure sensors to the end of the nose and collect pressure data from in front of the aircraft before the airflow has been disturbed. All five air data sensors are calibrated and compensated for temperature effects. **Error! Reference source not found.** shows the nose board of the ADS which collects the data from the Pitot tube and airflow sensors.

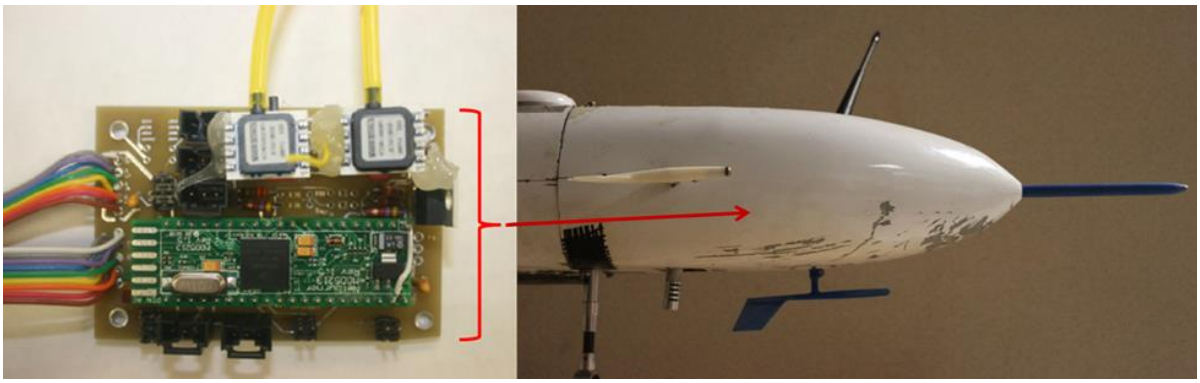

Figure 3.4 - Air data system (left: nose board, right: pitot-tube and air flow sensors)

Calibration of the nose board was performed on a calm air day with little or no wind. From dynamic pressure the airspeed of a UAV can be estimated using

$$V_{Pitot} = k\sqrt{\frac{2 \cdot P_d}{\rho}}$$

where k is the calibration constant due to misalignment error during the installation. P_d is the differential pressure data in units of Pascal, and ρ is air density measured in units of kilograms per cubic meter. The air density based on the static pressure, P_s, and the temperature, T, of the surrounding air is calculated using:

$$\rho = \frac{P_s}{287.058 \cdot T}$$

Based on the above equations the optimal calibration constant, k, is found by assuming no wind and solving the evaluation function using:

$$\min E(|V_{Pitot} - V_{GPS}|)$$

where V_{Pitot} is the airspeed sensed by the Pitot tube and is a function of k, V_{GPS} is the ground speed for the UAV from the GPS sensor. V_{Pitot} and V_{GPS} are identical under a no wind condition so the expectation, $E[\cdot]$, of the difference throughout the entire flight is zero. Through this process the optimal value for k was found to be 1.115 through numerical solutions.

Figure shows the results of calculating the airspeed after calibration where both the airspeed and GPS speed match quite well. The presence of a light breeze can be noticed because of a small difference between Pitot tube and GPS data.

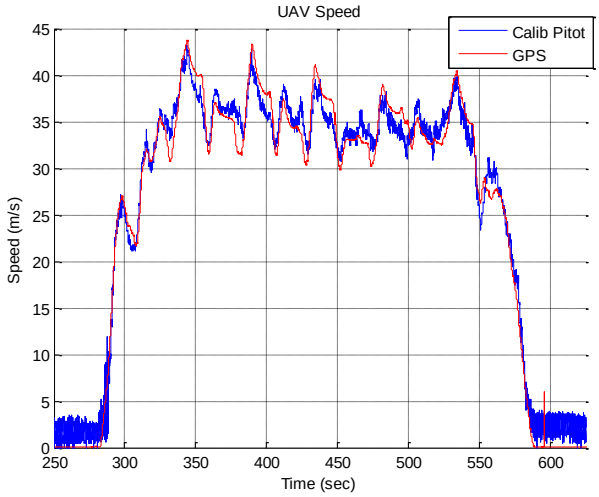

Figure 3.5 - Calibrated air speed data

For validation of wind sensing methods it is important to have a ground truth. This was accomplished through the use of various weather stations at the flight field. The weather station selected for this application was the Ultimeter 2100 from Pete Bros., shown in **Error! Reference source not found.**. In order to minimize ground effects and nearby structures the weather stations were mounted on poles approximately 8 meters above the ground.

Figure 3.5 - Pete Bros. Ultimeter 2100 and Weather station setup

3.2.2 Wind Estimation Algorithm for a Small UAV (UKF Development)

Given GPS velocity, aircraft attitude, and both pressure and flow angles, the wind speed can be estimated using an Unscented Kalman Filter in the following form:

$$\dot{x} = f(x,u)$$

$$y = h(x) + v$$

where $v \sim N(0,R)$, $\dot{x}$ is the derivative of the states, *f(x,u)* is the nonlinear function that relates the derivative of the states to the states and inputs of the system. y is the output of the system, *h(x)* is the nonlinear measurement model, and v is the zero-mean Gaussian measurement noise with a covariance matrix of *R*. The UKF is an extension to the Kalman Filter that estimates the states of a nonlinear system based on the concept that "*it is easier to approximate a Gaussian distribution than it is to approximate an arbitrary nonlinear function or transformation*". In other words instead of sending the states through a nonlinear function for the prediction, a number of sigma points are selected that represent the mean and covariance of the states and the nonlinear function is applied to those sigma points. This leads to a cloud of transformed points that represents the statistics of the output of the system.

The system states, inputs, and outputs of the proposed UKF are listed below:

$$\mathbf{x} = \begin{bmatrix} u & v & w & \phi & \theta & \psi & w_x & w_y & w_z \end{bmatrix}^T$$

$$\mathbf{b} = \begin{bmatrix} b_{a_x} & b_{a_y} & b_{a_z} & b_p & b_q & b_r \end{bmatrix}^T$$

$$\mathbf{u} = \begin{bmatrix} a_x & a_y & a_z & p & q & r \end{bmatrix}^T$$

$$\mathbf{y} = \begin{bmatrix} V_x & V_y & V_z & V_{pitot} & \alpha & \beta \end{bmatrix}^T$$

where $[u, v, w]$ is the air speed expressed in the body frame, $[\phi, \theta, \psi]$ are the Euler angles, roll, pitch, and yaw, respectively, and $[w_N, w_E, w_D]$ are the wind states in the North-East-Down (NED) inertial frame. For the inputs to the system, $[a_x, a_y, a_z]$ are the body frame accelerations measured by the onboard IMU and $[p, q, r]$ are the angular rates also measured by the IMU. The outputs of the system are $[V_x, V_y, V_z]$, the ground velocities measured by the GPS receiver, and $[V_{Pitot}, \alpha, \beta]$ consisting of the airspeed, angle of attack, and sideslip angle which are measured by the ADS.

The first step in the UKF is to develop the dynamics of the system. The body axis velocities are calculated using:

$$\begin{bmatrix} \dot{u} \\ \dot{v} \\ \dot{w} \end{bmatrix} = \begin{bmatrix} rv - qw + a_x \\ pw - ru + a_y \\ qu - pv + a_z \end{bmatrix} + \mathbf{DCM}\left(\phi, \theta, \psi\right)^T \begin{bmatrix} 0 \\ 0 \\ g \end{bmatrix}$$

where the Direct Cosine Matrix (DCM) is given by:

$$DCM\left(\phi, \theta, \psi\right) = \begin{bmatrix} c\psi c\theta & -s\psi c\theta + c\psi s\theta s\phi & s\psi s\phi + c\psi s\theta c\phi \\ c\psi c\theta & c\psi c\phi + s\psi s\theta s\phi & -c\psi s\phi + c\psi s\theta c\phi \\ -s\theta & c\theta s\phi & c\theta c\phi \end{bmatrix}$$

Here '*s*' and '*c*' are abbreviated sine and cosine functions respectively.

The orientation angles are calculated using the Inverted Kinematic Equations below:

$$\begin{bmatrix} \dot{\phi} \\ \dot{\theta} \\ \dot{\psi} \end{bmatrix} = \begin{bmatrix} 1 & \sin\phi\tan\theta & \cos\phi\tan\theta \\ 0 & \cos\phi & -\sin\phi \\ 0 & \sin\phi\sec\theta & \cos\phi\sec\theta \end{bmatrix} \begin{bmatrix} p \\ q \\ r \end{bmatrix}$$

Because wind is composed of turbulent air flow it is by definition random and, therefore, in order to predict future wind states a random walk model is used (*Langelaan, J.W., et. al., 2010*).

Finally, in order to relate the UAV velocities to the wind velocities the output equations were introduced. Since the difference in GPS velocity and body axis velocity is due to the wind acting on the UAV, the dynamic equation rotates the body axis velocity into the inertial frame using the DCM and corrects for wind with the GPS velocity using:

$$\begin{bmatrix} V_x \\ V_y \\ V_z \end{bmatrix} = \mathbf{DCM}\left(\phi, \theta, \psi\right) \begin{bmatrix} u \\ v \\ w \end{bmatrix} + \begin{bmatrix} w_x \\ w_y \\ w_z \end{bmatrix}$$

The measurement equations are comprised of the wind triangle equation and the equations of air flow angles, listed as the following:

$$u = V \cos\alpha \cos\beta$$
$$v = V \sin\beta$$
$$w = V \sin\alpha \cos\beta$$

3.2.3 – Simulation and Flight-Test Validation

In terms of wind gust estimation and later gust suppression control, the simulator described in Section #1 was used. The UKF described above was developed for estimating the wind states based on the response of the UAV within the FDC simulation environment.

Figure shows the UKF estimation of a sinusoidal wind gust. Here the filter stayed within 0.5 meter per second of error throughout the entire flight, and converged as soon as the UAV flies into the wind field (5 seconds into flight).

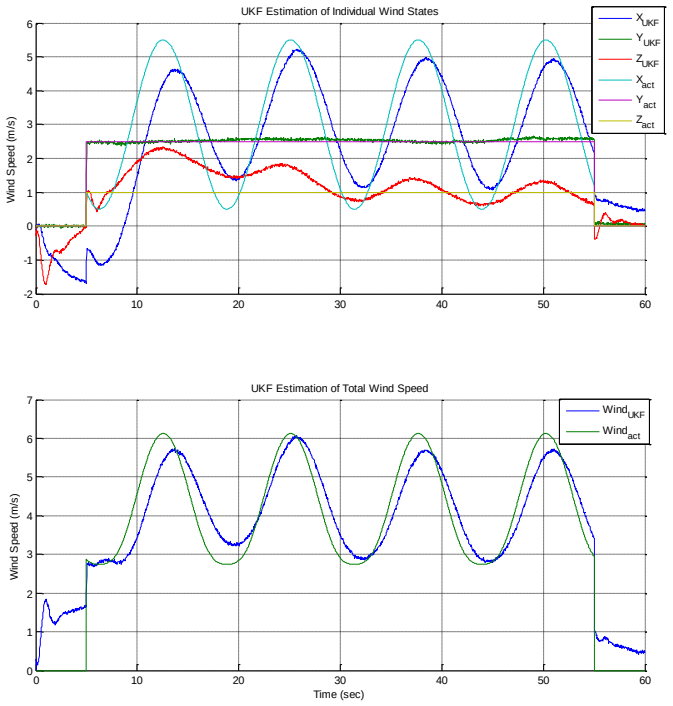

Figure 3.6 - UKF estimation of wind for a sinusoidal gust field

A set of flight data collected with the WVU Phastball was used for flight validation purposes, using the raw measurements from pressure and air flow angle sensors. This data set is approximately 5 minutes in duration from take-off to landing of the aircraft with a maximum altitude of approx. 120 meters. The flight data included several lateral and longitudinal doublet maneuvers. The wind estimation results using UKF are shown in the left side of Figure 3.7. In an effort to validate the wind estimation results, the horizontal planar wind speed and direction were calculated from the wind velocity component estimates and are plotted with the corresponding measurements from the ground weather station in the right portion of Figure 3.7. The wind speed

reference directly from the weather station is shown together with the wind estimates at the flight altitude using the power law correction.

Figure 3.7 shows that the wind estimates are reasonable when compared with the ground weather station. These estimates do not closely match the ground weather station, which is to be expected since they are measuring different points in the local wind field, and local turbulence will cause changes in the measurement of the wind. Additionally, these measurements are compared at the same point in time, but due to the flow of the wind, this comparison is not truly valid. However, in general the wind estimates and ground weather station are in good agreement, which provides justification that the wind estimation results are reasonable.

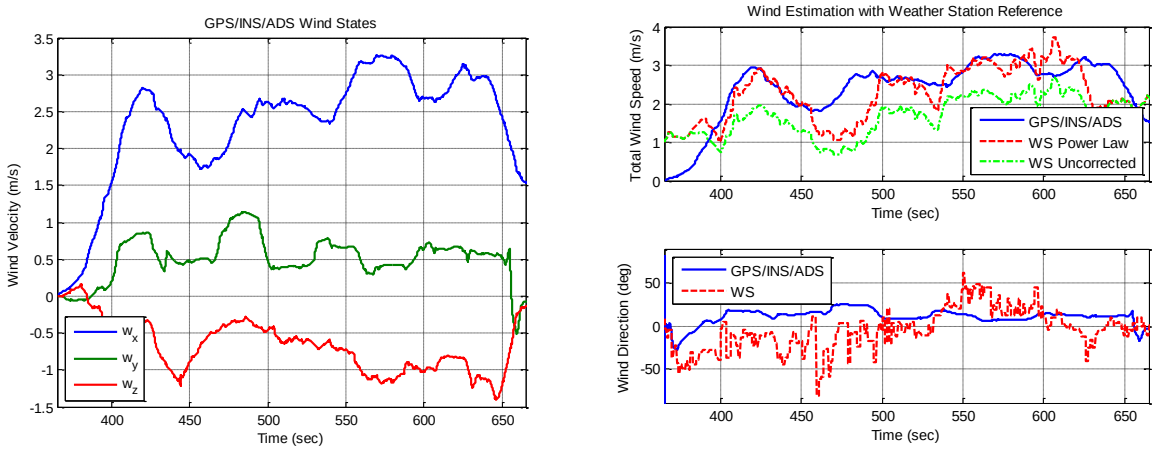

Figure 3.7 – Estimated wind velocity components and comparison with ground weather station reference

3.2.4 – Cooperative Wind Estimation with UAV Formation

For cooperative wind sensing, the UKF described above was converted for the follower UAV in order to include the wind estimation of the leader as a measurement. This was accomplished by modifying the above $[V_x, V_y, V_z]$ equation by adding in the estimated wind states of the leader aircraft, $[\hat{w}_{LN}, \hat{w}_{LE}, \hat{w}_{LD}]$, as shown below:

$$\begin{bmatrix} V_x \\ V_y \\ V_z \end{bmatrix} = DCM(\phi,\theta,\psi)\begin{bmatrix} u \\ v \\ w \end{bmatrix} + \begin{bmatrix} W_N \\ W_E \\ W_D \end{bmatrix} + \begin{bmatrix} \hat{W}_{LN} \\ \hat{W}_{LE} \\ \hat{W}_{LD} \end{bmatrix}$$

The wake modeling described in Section 3.1 was used to determine the induced wind on the follower from the leader's wake. Table 3.2 below shows the advantages of using cooperative wind gust estimation. It can be observed that the mean of the error is reduced significantly from using follower flight data only.

Figure 3.8 shows the wind field used for the simulation of cooperative wind sensing from the follower and leader UAV respectively. As shown, there was a sinusoidal wind field along the North and East axis with a magnitude of 2.5 and 1 m/s respectively with a bias of 3 and 2 m/s respectively. Also, there is a 1 m/s constant wind along the Down axis for both UAVs.

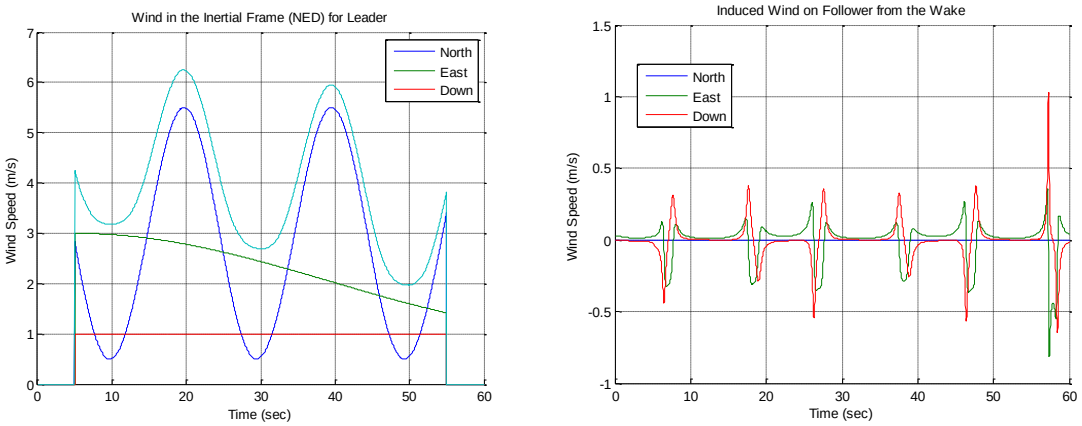

Figure 3.8 - Wind field of Leader UAV (left) and induced wind on follower from the leader's wake (right)

Two separate approaches were used. The first approach consists in the UKF estimation of wind using only leader data; this was done as a baseline in order to compare estimation results under various scenarios. The second approach is based on the UKF estimation of follower wind using the wake information generated by the leader. In other words, due to the increase in turbulence and induced wind gusts, the UKF estimation of the wind states sensed by the follower are never as good as the leader. However, by using the wind estimation of the leader the follower can estimate the wind with much greater precision. **Error! Reference source not found.** shows the statistics of UKF wind estimation using leader data only, follower data only, and cooperative wind estimation. The analysis of the data in the case of cooperative wind estimation shows that the mean of the error over all three axis dropped by approximately 21%; similarly, the standard deviation improved by approximately 22%.

Table 3.2 Cooperative wind estimation statistics

	Mean of Error (m/s)	Std of Error (m/s)
Leader X	0.6523	0.3809
Leader Y	0.2718	0.2571
Leader Z	0.3757	0.3214
Leader Norm	0.8003	0.5608
Follower X	0.5958	0.3522
Follower Y	0.9104	0.5857
Follower Z	0.3751	0.3590
Follower Norm	1.1509	0.7720
Coop X	0.7569	0.4283
Coop Y	0.3282	0.2765
Coop Z	0.3539	0.3290
Coop Norm	0.8977	0.6068

3.3 – Gust Suppression Control Preliminary

After knowing the wind states of the leader aircraft, the follower can compensate for the effects that the wind gusts will have on its dynamics. It is well known that large wind gusts can induce large accelerations along the *z* axis, which can potentially cause structure damages and passenger discomfort. In order to alleviate the effects of the wind on the *z* component of acceleration, an elevator command is added on top of the command coming from the outer loop controller.

The simulation scenario is to reduce the gust level detected during a formation flight where the follower is constantly affected by the leader's wake vortices. Figure 3.9 shows the induced wind from the leader's wake as described in a previous section. It is important to note here that as the follower aircraft moves through the wake of the leader aircraft it can reach a significant roll angle. This is due to the fact that the induced wind along the Y and Z axes can induce acceleration along the local z axis of the airplane. Therefore, it is important to consider both the wind speed and acceleration during the controller design.

The change in elevator is based on the amplitude of the induced wind as well as the sign of the vertical position relative to the leader (ζ_1) and the sign of the roll angle of the follower (ζ_2), which is shown in the following equation:

$$\delta_E = (\zeta_1 + \zeta_2) * (k_1 W_E + k_3 \dot{W}_E) + k_2 W_D + k_4 \dot{W}_D$$

The relationships below show instead the logic in flipping the sign of the elevator command as a function of the relative positions between the leader and the follower.

$$\zeta_1 = -1 \qquad P_{DF} < P_{DL}$$

$$\zeta_2 = -1 \qquad \phi_F < 0$$

Figure 3.10 shows the acceleration of the follower due to an encounter with the leader's wake both with and without gust suppression. Finally, Table shows the statistics of simulated gust suppression control which refers to the simulation of the previous two plots. As shown, the maximum vertical acceleration induced by the wake was almost 16 $\mathrm{m/s^2}$ while during gust suppression the maximum vertical acceleration drops to less than 3 $\mathrm{m/s^2}$.

Table 3.3 Gust suppression control statistics

Statistics	No Gust Suppression Control	Gust Suppression Control
Mean	-0.018	0.0031
std	1.7427	1.0
Max	15.9639	2.8185

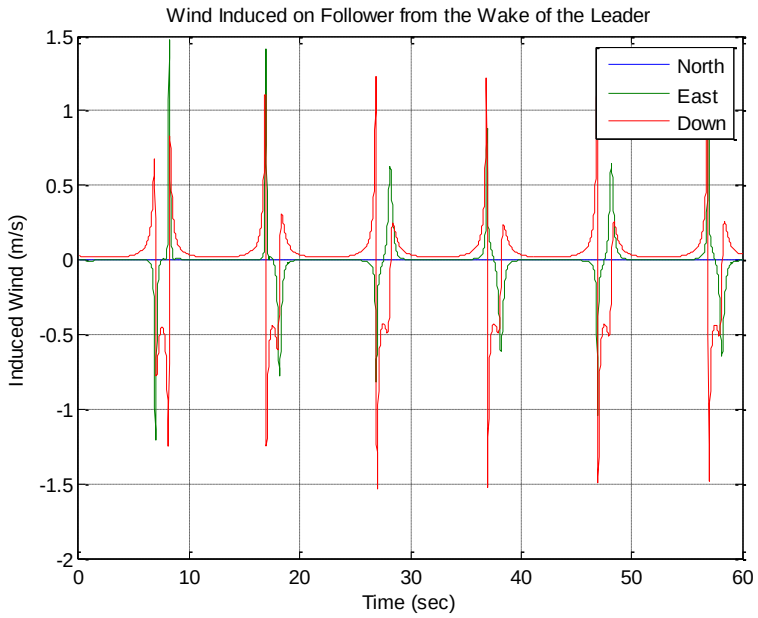

Figure 3.9 - Induced wind from the leader's wake onto the follower

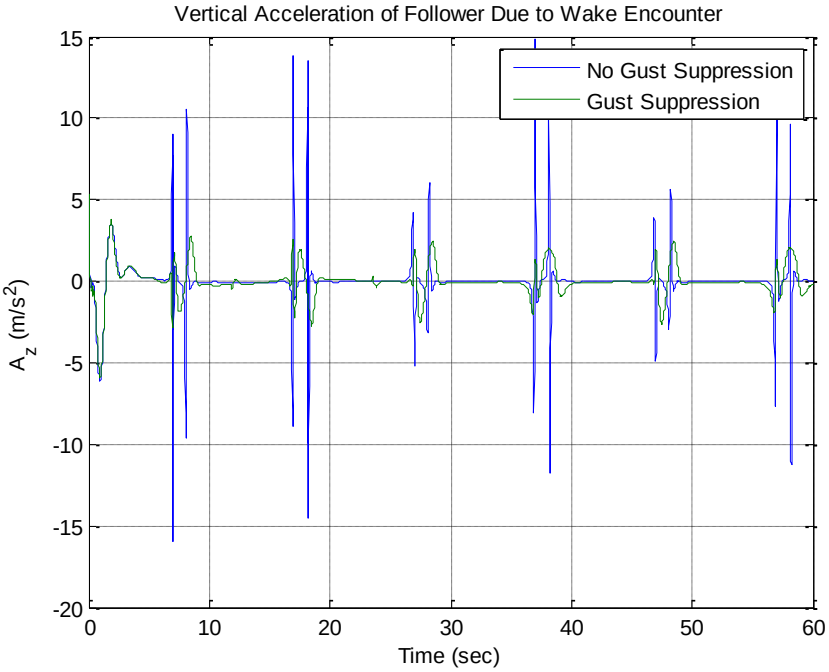

Figure 3.10 - Vertical acceleration of the follower UAV during wake encounter

4. - Conclusions

Throughout Phase I of the project, the following tasks have been accomplished:

- Close Formation Flight with Small UAVs

Close formation flight (up to ~5 wingspan or ~12 m) was proved to be achievable with two lost-cost small UAVs; the formation flight control laws performed as desired in these flight tests. It is envisioned that this experiment will contribute to the future of close formation flight research for energy saving and improved air traffic management.

- Wind Gust Estimation with Small UAVs

Two unscented Kalman filters were developed for the estimation of the wind gusts using single or groups of small UAVs. Single-UAV flight data showed the effectiveness of the proposed UKF using the weather station as the reference. In addition, through simulation it was shown that the cooperative UKF can achieve substantially better estimation results of the local wind field when using information from both the leader and follower.

- Wake Encountering Test Using Small UAVs

Small UAVs are shown to be reliable and feasible platforms for wake encountering test through multiple close formation flights. To the best of our knowledge this is the first experimental effort where wake vortices from small UAVs (~25 lbs) were measured. The collected sensor data can provide valuable insights to the understanding of wake dynamics as well as its interaction with follower aircraft.

- Preliminary Gust Suppression Control for Formation Flight

Based from the PMUS simulation environment, a set of gust suppression control laws were developed and validated. Initial results showed promising improvements on the reduction of acceleration during close formation flights.

In summary, Phase I of the LEARN project has proved the concept of using groups and/or small formation of small UAVs for gust sensing and suppression control missions. All the collected data and developed algorithms have laid a solid foundation for further breakthroughs in a Phase II. The main objectives of the Phase II pending proposal are to refine the wake models, the gust/wake estimation algorithms, and the gust suppression control schemes developed during Phase I, leading to performing in-flight cooperative gust sensing and suppression control experiments.

5. - References

Gertz, T., Holzapfel, F., and Darracq, D., (2002), "Commercial Aircraft Wake Vortices," Progress in Aerospace Science 38, pp. 181-208.

Gross, J.; Gu, Y., Gururajan, S., (2010), "A Comparison of Extended Kalman Filter, Sigma-Point Kalman Filter, and Particle Filter in GPS/INS Sensor Fusion." AIAA Guidance, Navigation, and Control Conf., pp. 1-19. 2010

Gu, Y., Campa, G., Seanor, B., Gururajan, S., and Napolitano, M.R., (2006), "Design and Flight Testing Evaluation of Formation Control Laws," IEEE Transactions Control System Technology, Vol. 14, No. 6, pp. 1105-1112.

Gu, Y., Campa, G., Seanor, B., Gururajan, S., and Napolitano, M.R., (2009), "Autonomous Formation Flight – Design and Experiments," Chapter 12, Aerial Vehicles, ISBN 978-953-7619-41-1, In-Tech, pp. 233-256.

Hoblit, F. M., (2001), Gust Loads on Aircraft: Concepts and Applications, AIAA Educational Series, ISBN: 0-930403-45-2.

Klein, V., and Morelli, E. A., (2006), Aircraft System Identification: Theory and Practice, AIAA Education Series, AIAA, Virginia.

Langelaan, J. W., Alley, N., Neidhoefer, J., (2010), "Wind Field Estimation for Small Unmanned Aerial Vehicles", AIAA Journal of Guidance, Control, and Dynamics.

McGrail, A.K., (2012), "OnBoard Parameter Identification for a Small UAV", M.S. Thesis, West Virginia University.

Rhudy, M., Larrabee, T., Chao, H., Gu, Y., Napolitano, M.R., (2013), "UAV Attitude, Heading, and Wind Estimation Using GPS/INS and an Air Data System", AIAA Guidance Navigation and Control Conference.

Rauw, M., (2001),"FDC 1.2 – A Simulink Toolbox for Flight Dynamics and Control Analysis", 2nd ed.

Sarpkaya, T., (2000), "New Model for Vortex Decay in the Atmosphere," Journal of Aircraft, Vol. 37, No. 1, pp. 53–61.

Simon, D., (2006), "Optimal State Estimation: Kalman, H-Infinity, and Nonlinear Approaches." Wiley & Sons.

Vachon, M. J., Ray, R. J., Walsh, K. R., and Ennix, K., (2002), "*F/A-18 Aircraft Performance Benefits Measured During the Autonomous Formation Flight Project*," AIAA 2002-4491, Proceedings of the AIAA Flight Mechanics Conference and Exhibit.

Appendix A

Copies of Publications

- A.1 (Full paper) - *Rhudy, M., Larrabee, T., Chao, H., Gu, Y., and Napolitano, M.R.*, "UAV Attitude, Heading, and Wind Estimation Using GPS/INS and an Air Data System," the 2013 AIAA Guidance, Navigation, and Control Conference, ID#: 1659091, Boston, Massachusetts, Aug. 19-22, 2013.

- A.2 (Full paper) - *Larrabee, T., Chao, H., Mandal, T., Gururajan, S., Gu, Y., and Napolitano, M.R.*, "Design, Simulation, and Flight Test Validation of a UAV Ground Control Station for Aviation Safety Research and Pilot Modeling," the 2013 AIAA Guidance, Navigation, and Control Conference, ID#: 1664533, Boston, Massachusetts, Aug. 19-22, 2013.

- A.3 (Abstract) - *Larrabee, T., Chao, H., Gu, Y., and Napolitano, M.R.*, "Wind Field and Wake Estimation in UAV Formation Flight," submitted to the 2014 American Control Conference, currently under review.

- A.4 (Abstract) - *Rice, C., Gu, Y., Chao, H., Larrabee, T., Gururajan, S., and Napolitano, M.R.*, "Control Performance Analysis for Autonomous Close Formation Flight Experiments," submitted to the 2014 American Control Conference, currently under review.

Paper A.1

UAV Attitude, Heading, and Wind Estimation Using GPS/INS and an Air Data System

Matthew Rhudy[1], Trenton Larrabee[2], Haiyang Chao[3], Yu Gu[4], and Marcello R. Napolitano[5]
Department of Mechanical and Aerospace Engineering, West Virginia University, Morgantown, WV, 26506

A new attitude, heading, and wind estimation algorithm is proposed, which incorporates measurements from an air data system to properly relate predicted attitude information with aircraft velocity information. Experimental Unmanned Aerial Vehicle (UAV) flight data was used to validate the proposed approach. The experimental results demonstrated effective estimation of the roll, pitch, yaw, and heading angles, and provided a smoothed estimate of the angle of attack and sideslip angles. The wind estimation results were validated with respect to measurments provided by a local weather station. It was shown that this new method of attitude estimation is effective in distinguishing the yaw and heading angles of the aircraft, properly regulating the attitude estimates with air data system measurements, and provding a reasonable estimate of the local wind field.

Nomenclature

a_x, a_y, a_z	=	acceleration in aircraft body frame (m/s^2)
b	=	bias parameter vector
f	=	state prediction function
g	=	acceleration due to gravity (m/s^2)
h	=	observation function
k	=	discrete time index
l	=	power law exponent
p	=	roll rate (deg/s)
Q	=	process noise covariance matrix
q	=	pitch rate (deg/s)
R	=	measurement noise covariance matrix
r	=	yaw rate (deg/s)
T_s	=	sampling time (s)
u, v, w	=	body-axis velocity components (m/s)
u	=	input vector
v	=	measurement noise vector
V	=	total airspeed (m/s)
V_{pitot}	=	Pitot tube airspeed (m/s)
V_x, V_y, V_z	=	Earth-fixed components of velocity (m/s)
W	=	random walk coefficient
w_x, w_y, w_z	=	wind velocity components (m/s)

[1] Ph.D. Candidate, Mechanical and Aerospace Engineering (MAE) Department, PO Box 6106, mbr5002@gmail.com, AIAA Student Member.
[2] M.S. Student, MAE Department, PO Box 6106.
[3] Postdoctoral Researcher, MAE Department, PO Box 6106, AIAA Member.
[4] Assistant Professor, MAE Department, PO Box 6106, AIAA Senior Member.
[5] Professor, MAE Department, PO Box 6106, AIAA Senior Member.

$\mathbf{w}$	=	process noise vector
$\mathbf{x}$	=	state vector
$\mathbf{y}$	=	output vector
z	=	height above ground (m)
$\mathbf{z}$	=	measurement vector
α	=	angle of attack (deg)
β	=	sideslip angle (deg)
θ	=	pitch angle (deg)
ϕ	=	roll angle (deg)
ψ	=	yaw angle (deg)

I. Introduction

THE estimation of aircraft states and parameters can be a challenging problem due to the inevitable presence of wind. This difficulty is especially prevalent for small Unmanned Aerial Vehicle (UAV) applications, due to their smaller size and weight. One particular problem of interest is low-cost attitude estimation, which is important for many aircraft applications such as flight control[1] and remote sensing[2]. A popular approach to the attitude estimation problem involves the integration of sensor information from a Global Positioning System (GPS) receiver with that of a low-cost Inertial Navigation System (INS)[3]. Various formulations of attitude estimation using GPS/INS sensor fusion exist in the literature[4-7], containing comparison studies evaluating different algorithms and nonlinear estimators.

A problem with the existing work in GPS/INS sensor fusion for attitude estimation[4-7] is that it implicitly assumes that the angle of attack and sideslip angles of the aircraft are zero, i.e. the aircraft is always pointing in the direction of its total velocity. The INS can be used to predict the attitude angles of the aircraft effectively through time integration of the rate gyroscope measurements from an Inertial Measurement Unit (IMU). Since these estimates tend to drift with time due to sensor biases, GPS velocity measurements are then used to regulate this drifting phenomenon. However, when using GPS velocity to regulate the attitude angles, current work implicitly makes a simplifying assumption that the orientation of the aircraft is equivalent to the direction of the total velocity of the aircraft. While under many operating conditions this approximation can lead to reasonable results, a more theoretically justifiable formulation should consider air data information in order to properly relate the INS predicted attitude with the GPS velocity calculations. The work presented herein derives a new formulation of attitude estimation that includes measurements from an Air Data System (ADS). The ADS provides measurements of the airspeed, angle of attack, and sideslip angle. The contribution of this work is that it provides a means for accurately estimating the true attitude of the aircraft, allows for a clear distinction between the heading and yaw angles of the aircraft, provides a smoothed estimate of the airspeed, angle of attack, and sideslip, and provides an estimate of the local wind speed and direction.

In this work, the wind field is estimated for both horizontal and vertical wind in order to properly correct INS attitude estimates with GPS velocity information. These wind estimates, however, can also be used for other purposes. Estimation of the wind field is useful in UAV applications for various objectives such as dropping objects, target tracking, geolocation[8], automatic control[9], energy harvesting, trajectory optimization[10], and air traffic control[11]. There is some existing work in the area of wind estimation, which was used for inspiration in deriving the new attitude and wind estimation formulation. Lefas developed a simple filter for wind estimation using magnetic heading, true airspeed, and radar measurements[11]. Kumon *et al.* studied the estimation of horizontal wind using a delta wing UAV with an iterative optimization approach, and validated the results with weather data from a meteorological agency[9]. Langelaan *et al.* presented a thorough simulation study of a direct method for estimating the wind field[10]. Cho *et al*. presented a horizontal wind estimation method using the Extended Kalman Filter (EKF)[12] with both simulated and experimentally collected flight data[8]. The horizontal wind speed and direction were predicted using a random walk noise assumption, then these states were regulated through the wind triangle comparison of ground speed from GPS and air speed[8]. The work presented herein expands upon this concept to include vertical wind, and also incorporates angle of attack and sideslip information, which are useful in relating the aircraft body frame to the wind frame.

The rest of this paper is organized as follows. Section II provides the derivation and description of the new attitude and wind estimation formulation. Section III describes the experimental UAV platform that was used to collect data for this study. Section IV presents some estimation results, followed by a conclusion in Section V.

II. Problem Formulation

This work considers the estimation of aircraft body-axis velocity components (u, v, w), Euler attitude angles, (ϕ, θ, ψ), and three-axis wind velocity components, (w_x, w_y, w_z). This estimation is performed through the fusion of IMU measurements of three-axis accelerations (a_x, a_y, a_z) and angular rates (p, q, r), GPS velocity components (V_x, V_y, V_z), and ADS measurements from a Pitot tube (V_{pitot}) and wind vanes for angle of attack (α) and sideslip (β). Additionally, a bias parameter vector was considered for the inertial sensors which are known to contain biases on the measurement signal[4,7]. Using these values, the state space system is formulated with the following state vector, **x**, bias parameter vector, **b**, input vector, **u**, and output vector, **y**:

$$\begin{aligned}
\mathbf{x} &= \begin{bmatrix} u & v & w & \phi & \theta & \psi & w_x & w_y & w_z \end{bmatrix}^T \\
\mathbf{b} &= \begin{bmatrix} b_{a_x} & b_{a_y} & b_{a_z} & b_p & b_q & b_r \end{bmatrix}^T \\
\mathbf{u} &= \begin{bmatrix} a_x & a_y & a_z & p & q & r \end{bmatrix}^T \\
\mathbf{y} &= \begin{bmatrix} V_x & V_y & V_z & V_{pitot} & \alpha & \beta \end{bmatrix}^T
\end{aligned} \tag{1}$$

The bias parameters are subtracted from the measured input vector before use in the filter

$$\mathbf{u} = \hat{\mathbf{u}} - \mathbf{b} \tag{2}$$

where ^ denotes the measured input vector from the IMU.

First, the state dynamics are defined. The conversion between the body-axes and Earth-fixed axes is given by the Direction Cosine Matrix (**DCM**), which is defined by successive rotations of the roll, pitch, and yaw angles (ϕ, θ, ψ) of the aircraft

$$\mathbf{DCM}(\phi,\theta,\psi) = \mathbf{R}_z(\psi)\mathbf{R}_y(\theta)\mathbf{R}_x(\phi) \tag{3}$$

where the rotation matrices are defined as

$$\mathbf{R}_x(\phi) = \begin{bmatrix} 1 & 0 & 0 \\ 0 & \cos\phi & -\sin\phi \\ 0 & \sin\phi & \cos\phi \end{bmatrix} \tag{4}$$

$$\mathbf{R}_y(\theta) = \begin{bmatrix} \cos\theta & 0 & \sin\theta \\ 0 & 1 & 0 \\ -\sin\theta & 0 & \cos\theta \end{bmatrix} \tag{5}$$

$$\mathbf{R}_z(\psi) = \begin{bmatrix} \cos\psi & -\sin\psi & 0 \\ \sin\psi & \cos\psi & 0 \\ 0 & 0 & 1 \end{bmatrix} \tag{6}$$

The state dynamics for the body-axis velocity states are then given by[13]

$$\begin{bmatrix} \dot{u} \\ \dot{v} \\ \dot{w} \end{bmatrix} = \begin{bmatrix} rv - qw + a_x \\ pw - ru + a_y \\ qu - pv + a_z \end{bmatrix} + \mathbf{DCM}(\phi,\theta,\psi)^T \begin{bmatrix} 0 \\ 0 \\ g \end{bmatrix} \tag{7}$$

The attitude state dynamics are defined using[14]

$$\begin{bmatrix} \dot{\phi} \\ \dot{\theta} \\ \dot{\psi} \end{bmatrix} = \begin{bmatrix} 1 & \sin\phi\tan\theta & \cos\phi\tan\theta \\ 0 & \cos\phi & -\sin\phi \\ 0 & \sin\phi\sec\theta & \cos\phi\sec\theta \end{bmatrix} \begin{bmatrix} p \\ q \\ r \end{bmatrix} \tag{8}$$

Due to the random nature of wind, e.g. turbulence, it is challenging to predict the future behavior of the local wind field dynamics. Therefore, the wind velocity state dynamics are modeled as a random walk process[8].

The state dynamic equations have been defined in continuous-time using the following format

$$\dot{\mathbf{x}} = \mathbf{f}_c\left(\mathbf{x}, \mathbf{u}\right) \tag{9}$$

where $\mathbf{f}_c$ is the nonlinear continuous-time state transition function. In order to implement these equations in a discrete-time filter, a first order discretization is used[15]

$$\mathbf{x}_k = \mathbf{x}_{k-1} + T_s \mathbf{f}_c\left(\mathbf{x}_{k-1}, \mathbf{u}_{k-1}\right) + \mathbf{w}_k \approx \mathbf{f}\left(\mathbf{x}_{k-1}, \mathbf{u}_{k-1}\right) + \mathbf{w}_k \tag{10}$$

where $\mathbf{f}$ is the nonlinear discrete-time state transition function, T_s is the sampling time of the system, and $\mathbf{w}$ is the zero-mean Gaussian process noise vector with covariance matrix, $\mathbf{Q}$.

To define the dynamics for the bias parameters, a first order Gauss-Markov noise model was used. In a related work[16], the Allan variance[17] approach presented in[18,19] was used to determine the parameters of the first order Gauss-Markov noise model for the dynamics of the bias on each IMU channel. The Gauss-Markov noise model for each sensor measurement involves two parameters: a time constant and a variance of the wide band sensor noise. Using this model, the dynamics for the bias parameters are given by

$$\mathbf{b}_k = \mathbf{b}_{k-1} e^{-\frac{T_s}{\boldsymbol{\tau}}} + \mathbf{n}_{k-1} \tag{11}$$

where $\boldsymbol{\tau}$ is a vector of time constants and $\mathbf{n}$ is a zero-mean noise vector with variance given by a diagonal matrix of the variance terms for each sensor. The time constant and variance terms were calculated in[16] for each channel of the same IMU that was considered for this study.

Next, the output equations are defined. In order to properly relate the velocity information, the **DCM** is again used to relate the body frame to the Earth-fixed frame. Using this relationship, the body-axis velocity components can be rotated into the Earth-fixed frame and corrected for wind by[10,13]

$$\begin{bmatrix} V_x \\ V_y \\ V_z \end{bmatrix} = \mathbf{DCM}\left(\phi, \theta, \psi\right) \begin{bmatrix} u \\ v \\ w \end{bmatrix} + \begin{bmatrix} w_x \\ w_y \\ w_z \end{bmatrix} \tag{12}$$

The Pitot tube is mounted in the aircraft along the longitudinal axis, therefore it will measure the airspeed in the body *x*-axis, thus defining the simple output equation

$$V_{pitot} = u \tag{13}$$

The angle of attack and sideslip angle are calculated from the body-axis velocity components using[13]

$$\begin{aligned} \alpha &= \tan^{-1}\left(\frac{w}{u}\right) \\ \beta &= \sin^{-1}\left(\frac{v}{\sqrt{u^2 + v^2 + w^2}}\right) \end{aligned} \tag{14}$$

Using these relationships, the output equations are defined in the following form

$$\mathbf{y}_k = \mathbf{h}(\mathbf{x}_k) + \mathbf{v}_k \tag{15}$$

where **h** is the nonlinear observation function and **v** is the zero-mean Gaussian measurement noise vector with covariance matrix, **R**. The measurement vector, **z**, is provided by GPS velocity calculations, Pitot tube airspeed, and wind vane measurements.

In addition to this GPS/INS/ADS sensor fusion formulation, a comparatively tuned GPS/INS formulation is considered, which is equivalent to the GPS/INS/ADS formulation except that the wind states are removed and the ADS measurements are omitted from the measurement update. This formulation is used as a comparison, in order to illustrate the benefits of using the ADS information. Since both the GPS/INS/ADS and GPS/INS sensor fusion formulations contain nonlinear functions, a nonlinear state estimation technique such as the Extended Kalman Filter (EKF)[12] or Unscented Kalman Filter (UKF)[20] is required. The UKF was selected for this study due to its ease of implementation (no need to calculate Jacobian matrices)[21,22]. The equations for the UKF are well documented in various sources, e.g.[5,23,24], and therefore are not presented here.

III. Experimental Platform

This study uses flight data collected with the 'Red Phastball' small UAV which was designed, manufactured, and instrumented by researchers of the Flight Control Systems Lab (FCSL) at West Virginia University (WVU). The avionic payload includes a custom designed printed circuit board (PCB) featuring four redundant Analog Devices® Inertial Measurement Units (IMUs) and a Novatel OEM-V1 GPS receiver, as shown in **Fig. 1**.

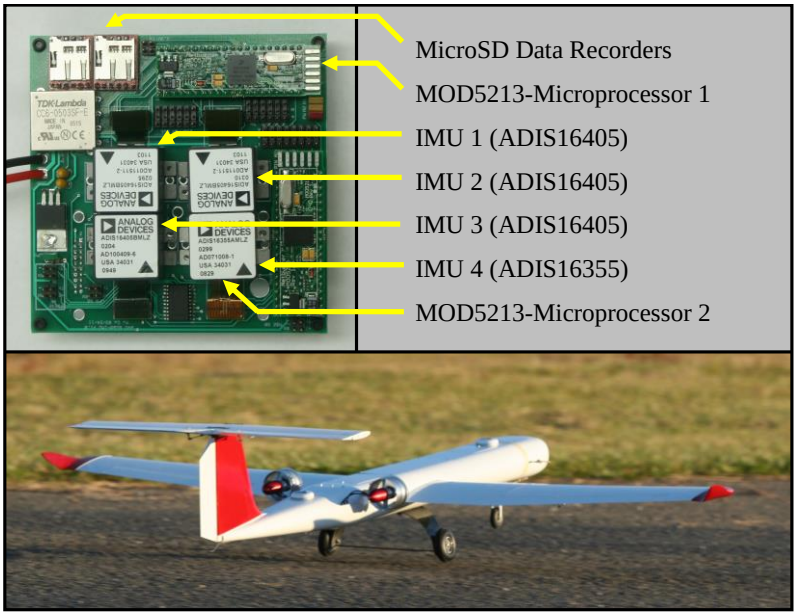

Fig. 1. WVU Red Phastball UAV and Avionics Board

The avionics board records measurements using μSD data loggers interfaced with the measurement systems using two MOD-5213 microprocessors. Although each IMU has an actual resolution of 14-bit, the resolution is improved by oversampling the signals at 200 Hz, then averaging down to 50 Hz, thus achieving a near equivalent of 18-bit resolution. Note that since typical low-cost attitude estimation uses a single IMU, for this study only the data from one of the IMUs, an Analog Devices ADIS16405, is used. Data were also collected from two angle of attack and one sideslip wind vanes attached to potentiometers with 10 V A/D at 16-bit resolution. A Pitot tube was mounted on the nose of the aircraft along the longitudinal axis, connected to Sensor Technics pressure sensors. The air data measurement system is shown in **Fig. 2**.

Fig. 2. Air Data Measurement System

For precision time alignment purposes, a Pulse Per Second (PPS) signal from the GPS receiver is recorded with the IMU data using an Analog to Digital (A/D) port on the MOD-5213 microprocessor. The GPS receiver calculates the local position and velocity using GPS satellite information. In addition to IMU and GPS data, a high-quality Goodrich® mechanical vertical gyroscope was used to obtain direct measurements at 50 Hz of the roll and pitch of the aircraft with 3.3 V A/D at 16-bit resolution. These measurements are used as a 'truth' reference in order to evaluate the low-cost attitude estimation performance.

To provide some validation data for the wind estimation, a portable ground weather station was installed during the flight test. A Peet Brothers Ultimeter 2100 weather station, shown in **Fig. 3**, was used to collect wind data at ~3 Hz with an accuracy of 0.9 m/s for the wind speed and 5% for the 16-point magnetic direction sensing. The weather station setup is mounted securely near the flight path at approximately 7 m off the ground.

Fig. 3. Ground Weather Station

The measurements of wind from the weather station and the UAV are taken at different altitudes, both of which are relatively close to the ground. For altitudes of up to ~200 m, the wind profile is approximated using the following power law due to the ground friction effects[8,25]

$$V_z = V_{ref}\left(\frac{z}{z_{ref}}\right)^{l} \tag{16}$$

where V_z is the scalar mean wind speed at height z above ground level, V_{ref} is the scalar mean wind speed at reference height z_{ref}, and l is the power law exponent. An existing study indicated the power law exponent of 1/7 to be effective for neutral stability conditions, therefore this value was used[26]. The power law correction was considered in order to more properly match the wind speed measured by the weather station to the wind speed measured by the UAV. The altitude of the UAV was estimated using the GPS position for this correction.

IV. Results

A set of flight data was collected with the WVU Red Phastball for use in this study. This data set is approximately 5 minutes in duration from takeoff to landing of the aircraft. The flight included lateral and longitudinal doublet maneuvers. Using the sensor data from this flight, estimation results were calculated using both the GPS/INS/ADS and GPS/INS sensor fusion formulations. Due to the availability of the 'truth' measurement from the vertical gyroscope, the error in the estimates of the roll and pitch angles can be calculated. Over the entire length of flight, the standard deviation of the roll and pitch errors is given in **Table 1**. For an illustrative representation of the roll and pitch estimation results, a 20 second segment of the estimated roll and pitch angle with corresponding vertical gyroscope (VG) measurements is shown in **Fig. 4**. Similar estimation performance is shown

for the GPS/INS/ADS and GPS/INS formulations in **Table 1** and **Fig. 4**. However, in order to witness the benefits of the GPS/INS/ADS formulation, the other states are considered.

Table 1. Summary of Roll and Pitch Estimation Performance

	Roll Error Standard Deviation	Pitch Error Standard Deviation
GPS/INS/ADS	1.0085	1.3125
GPS/INS	1.0299	1.1861

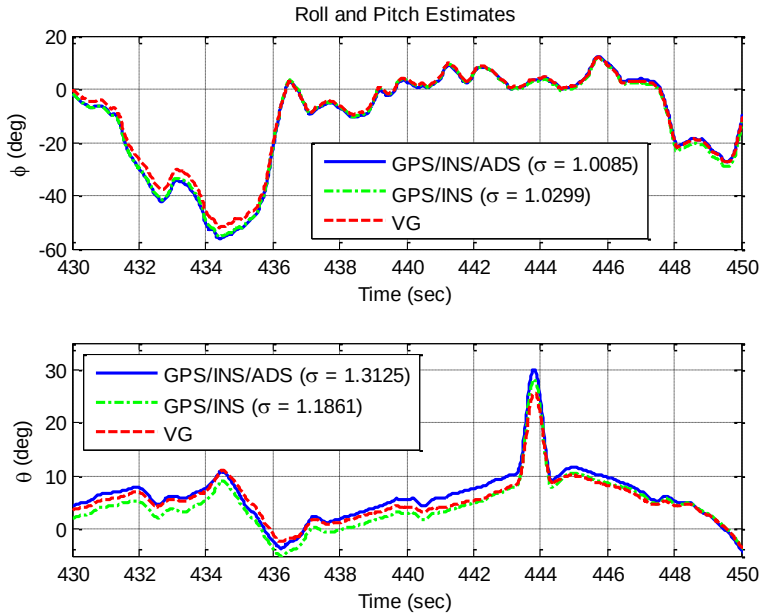

Fig. 4. Roll and Pitch Estimates with Vertical Gyroscope Reference

Although the flight data does not contain a 'truth' reference for the yaw angle, the components of velocity from GPS can be used to calculate the heading of the aircraft. The difference between the heading and yaw of the aircraft is the sideslip angle. A benefit of the GPS/INS/ADS formulation is the implicit estimation and regulation of the sideslip angle, β. This allows for distinct estimation of both the heading and yaw angles of the aircraft, which are assumed equal in standard GPS/INS attitude estimation. A 20 second segment of the estimated heading from yaw plus sideslip and calculated heading from GPS velocity is shown in **Fig. 5**. Close agreement is seen between these two calculations of heading. Additionally, the GPS/INS calculation of heading/yaw is shown in **Fig. 5**. It is clear that this approximation is not very good during this segment, as the sideslip oscillations are apparent in the signal. It is important to note that this comparison is for illustrative purposes only, as the GPS velocity is used in the calculation of yaw and sideslip, therefore the three calculations of heading are not independent.

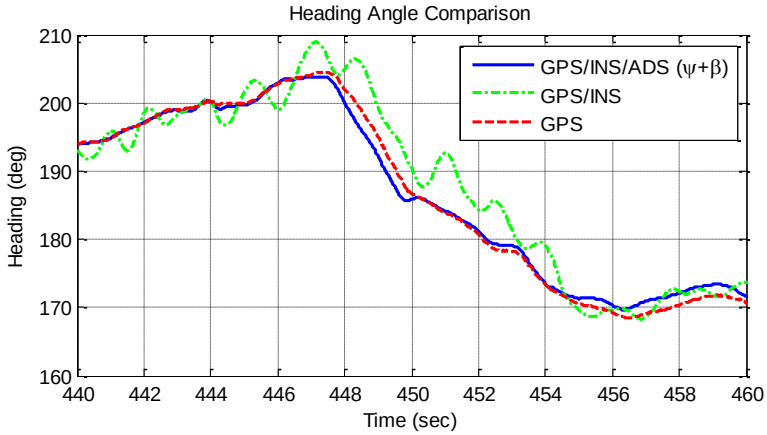

Fig. 5. Heading Angle Comparison

While it is possible to measure the angle of attack and sideslip angles of an aircraft through the use of wind vanes, these measurements contain various sources of uncertainty, including sensor noise, wind gust disturbances, and the inertial dynamics of the wind vane itself. Because of these uncertainties, the measurements of angle of attack and sideslip tend to be noisy. Calculating these angles from the body-axis velocity states leads to smoothed estimates. To illustrate this smoothing, a 10 second segment of the estimated angle of attack and sideslip angles are shown with the corresponding wind vane measurements in **Fig. 6**.

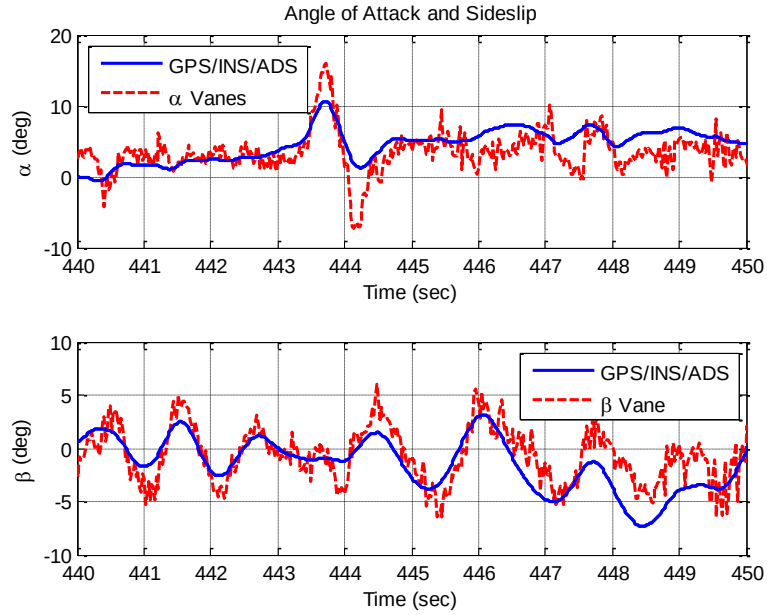

Fig. 6. Estimated and Measured Angle of Attack and Sideslip

It is shown in **Fig. 6** that in addition to smoothing out the high frequency noise in the vane signals, the peaks tend to be less extreme in the GPS/INS/ADS estimate. This could partially be explained by the inertial properties of the physical vane itself, i.e. the vanes have mass, and under changes in aircraft trajectory, the vane's inertia will carry it beyond the actual airspeed direction before settling down to the appropriate value.

For comparison purposes, the total airspeed estimate from each formulation is compared with the ground speed from GPS as well as with the ADS measurement in **Fig. 7**.

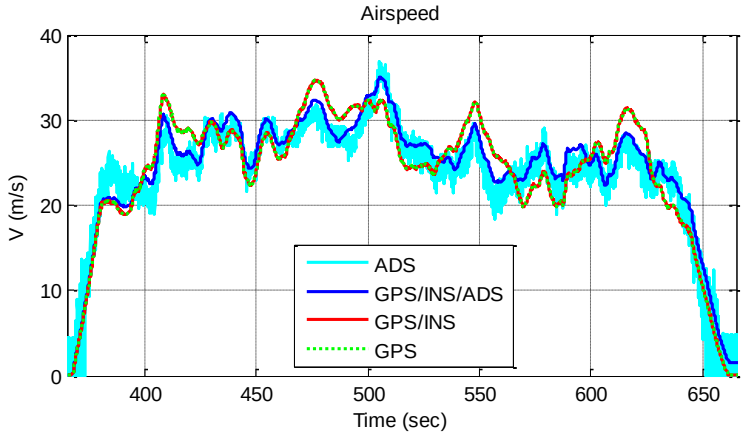

Fig. 7. Comparison of Airspeed, Ground Speed, and Pitot Tube Speed During Flight

It is shown in **Fig. 7** that the GPS/INS/ADS formulation is able to obtain a much smoother estimate of the airspeed than is provided directly from the ADS. The GPS/INS formulation, however, estimates the airspeed as being approximately equivalent to the ground speed. The discrepancy in airspeed and ground speed is clearly demonstrated. This discrepancy occurs due to the local wind field, thus motivating the use of this formulation for wind estimation. The estimated wind components are given in **Fig. 8**.

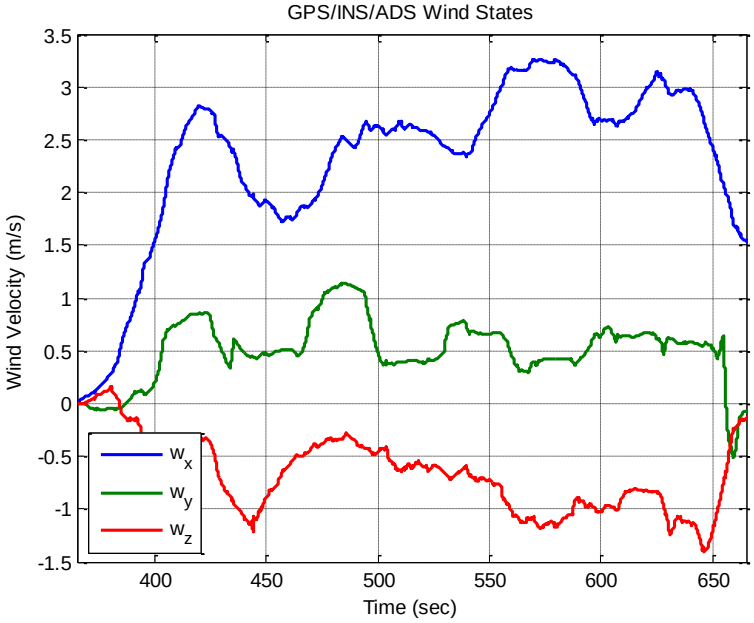

Fig. 8. Estimated Wind Velocity Components

In an effort to validate the wind estimation results, the horizontal planar wind speed and direction were calculated from the wind velocity component estimates and are plotted with the corresponding measurements from the ground weather station in **Fig. 9**. The wind speed reference from the weather station is shown in **Fig. 9** with uncorrected measurements as well as measurements with the power law correction from (16).

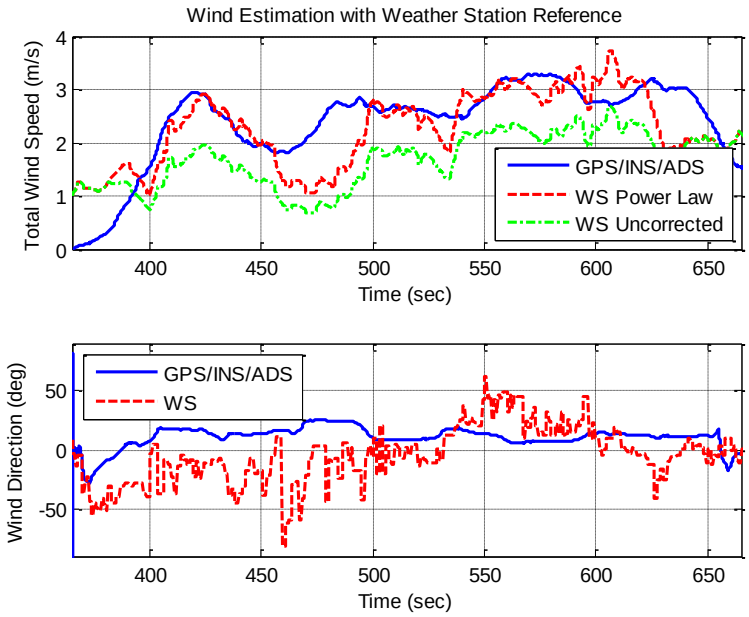

Fig. 9. Horizontal Planar Wind Speed and Direction

It is shown in **Fig. 9** that the wind estimates are reasonable when compared with the ground weather station. These estimates do not closely match the ground weather station, which is to be expected since they are measuring different points in the local wind field, and local turbulence will cause changes in the measurement of the wind. Additionally, these measurements are compared at the same point in time, but due to the flow of the wind, this comparison is not truly valid. However, in general the wind estimates and ground weather station roughly agree, which provides some justification that the wind estimation result is reasonable. In order to provide some statistical comparison, the GPS/INS/ADS estimates and weather station data can be used to calculate the wind field assuming it remains approximately constant in mean over the course of the flight. To obtain these values, the mean is taken over the period of flight. The results for the constant wind assumption are provided in **Table 2**. From these results it is clear that the power law correction is necessary for this application in order to more properly compare the wind speed. With this correction, the mean wind speed over the flight is very well approximated using the GPS/INS/ADS formulation. The constant wind direction estimation is not as good, with an error of approximately 16.7 degrees. A portion of this error is likely due to alignment errors when setting up the remote weather station. Also, this remote weather station has a course resolution of 6 degrees, which could partially contribute to the error.

Table 2. Constant Wind Field Estimation Results

	Mean Wind Speed	Mean Wind Direction
GPS/INS/ADS	2.2677 m/s	9.5353 deg
Wind Speed (Uncorrected)	1.6695 m/s	-7.1672 deg
Wind Speed (Power Law)	2.1848 m/s	-7.1672 deg

V. Conclusion

A new formulation of aircraft attitude estimation that incorporates air data system information was presented. A key distinction of this formulation compared to others is that the GPS velocity components are properly related to the body-axis velocity components through the consideration of wind. This effectly considers the wind triangle of airspeed, ground speed, and wind speed. Because of this adjustment, the estimated attitude states correspond to the actual orientation of the aircraft with respect to the fixed Earth. In particular, the yaw angle of the aircraft is able to be estimated independently of the heading angle through the consideration of sideslip. The experimental results demonstrated effective roll and pitch estimation performance, and the yaw estimate was reasonable when appropriately compared with GPS heading. A benefit of this formulation is that the estimated angle of attack and sideslip are smoother than the corresponding direct measurements from wind vanes, thus providing a means of filtering these measurements for use in other applications, such as parameter identification. Additionally, this

formulation provided estimates of the wind speed and direction, which were validated with respect to a ground weather station.

Acknowledgments

This research was partially supported by NASA grant # NNX10AI14G and # NNX12AM56A. The authors would like to thank Francis J. Barchesky for developing the air data system avionics.

References

[1] Calise, A. J., and Rysdyk, R. T., "Nonlinear Adaptive Flight Control Using Neural Networks," *IEEE Control Systems*, Vol. 18, No. 6, Dec. 1999, pp. 14-25.

[2] Changchun, L., Li, S., Hai-bo, W., and Tianjie, L., "The research on unmanned aerial vehicle remote sensing and its applications," *Proc. of the IEEE International Conference on Advanced Computer Control (ICACC '10)*, Shenyang, China, March 2010, pp. 644–647.

[3] Grewal, M. S., Weill, L. R., and Andrew, A. P., *Global Positioning, Inertial Navigation & Integration*, 2nd Ed., Wiley, New York, NY, USA, 2007.

[4] Crassidis, J. L., "Sigma-point Kalman filtering for integrated GPS and inertial navigation," *Proc. of the AIAA Guidance, Navigation, and Control Conference and Exhibit*, San Francisco, CA, USA, 2005.

[5] van der Merwe, R. D., Wan, E. A., and Julier, S. I., "Sigma-point Kalman filters for nonlinear estimation and sensor-fusion – applications to integrated navigation," *Proc. of the AIAA Guidance, Navigation, and Control Conference*, Providence, RI, USA, August 2004, pp. 1735-1764.

[6] Fiorenzani, T., et al., "Comparative Study of Unscented Kalman Filter and Extended Kalman Filter for Position/Attitude Estimation in Unmanned Aerial Vehicles," *IASI-CNR*, R. 08-08, 2008.

[7] Gross, J., Gu, Y., Rhudy, M., Gururajan, S., and Napolitano, M., "Flight test evaluation of GPS/INS sensor fusion algorithms for attitude estimation," *IEEE Trans. on Aerospace Electronic Systems*, Vol. 48, No. 3, July 2012, pp. 2128-2139.

[8] Cho, A., Kim, J., Lee, S., and Kee, C., "Wind Estimation and Airspeed Calibration using a UAV with a Single-Antenna GPS Receiver and Pitot Tube," *IEEE Trans. on Aerospace and Electronic Systems*, Vol. 47, No. 1, Jan. 2011, pp. 109-117.

[9] Kumon, M., Mizumoto, I., and Iwai, Z., "Wind Estimation by Unmanned Air Vehicle with Delta Wing," *Proc. of the 2005 IEEE International Conference on Robotics and Automation*, Barcelona, Spain, April 2005, pp. 1896-1901.

[10] Langelaan, J. W., Alley, N., and Neidhoefer, J., "Wind Field Estimation for Small Unmanned Aerial Vehicles," *AIAA Guidance Navigation and Control Conference*, Toronto, Canada, 2010.

[11] Lefas, C. C., "Real-Time Wind Estimation and Tracking with Transponder Downlinked Airspeed and Heading Data," *IEEE Trans. on Aerospace and Electronic Systems*, Vol. AES-23, No. 2, March 1987, pp. 169-174.

[12] Kalman, R. E., and Bucy, R. S., "New Results in Linear Filtering and Prediction Theory," *Journal of Basic Engineering (Trans. of ASME)*, Vol. 83, 1961, pp. 95-108.

[13] Klein, V., and Morelli, E. A., *Aircraft System Identification: Theory and Practice*, American Institute of Aeronautics and Astronautics, Inc., Reston, VA, 2006.

[14] Roskam, J., *Airplane Flight Dynamics and Automatic Flight Controls*, DARcorporation, Lawrence, KS, USA, 2003.

[15] Lewis, F. L., and Syrmos, V. L., *Optimal Control*, 2nd Ed., Wiley, NY, 1995.

[16] Gross, J. N., Gu, Y., Rhudy, M., Barchesky, F. J., and Napolitano, M. R., "On-line Modeling and Calibration of Low-Cost Navigation Sensors," *AIAA Modeling and Simulation Technologies Conference*, Portland, OR, USA, Aug. 2011.

[17] Allan, D. W., "Statistics of atomic frequency standards." *Proc. IEEE*, Issue 2, Vol. 54, Feb. 1966.

[18] Xing, Z. Gebre-Egziabher, D., "Modeling and Bounding Low Cost Inertial Sensor Errors," *IEEE/ION Position, Location and Navigation Symposium*, Monterey, CA, USA, 2008, pp. 1122-1132.

[19] Xing, Z., "Over-bounding Integrated INS/GNSS Output Errors," PhD Dissertation, The University of Minnesota, MN, USA, 2010.

[20] Julier, S., and Uhlmann, J., "A New Extension of the Kalman Filter to Nonlinear Systems," *SPIE Proceedings Series*, Vol. 3068, 1997, pp. 182-193.

[21] Rhudy, M., Gu, Y., Gross, J., Gururajan, S., and Napolitano, M. R., "Sensitivity and Robustness Analysis of EKF and UKF Design Parameters for GPS/INS Sensor Fusion," *AIAA Journal of Aerospace Information Systems*, Vol. 10, No. 3, March 2013, pp. 131-143.

[22] Rhudy, M., and Gu, Y., "Understanding Nonlinear Kalman Filters, Part I: Selection between EKF and UKF," *Interactive Robotics Letters*, West Virginia University, June 2013. Link: http://www2.statler.wvu.edu/~irl/page13.html.

[23] Rhudy, M., and Gu, Y., "Understanding Nonlinear Kalman Filters, Part II: An Implementation Guide," *Interactive Robotics Letters*, West Virginia University, June 2013. Link: http://www2.statler.wvu.edu/~irl/page13.html.

[24] Rhudy, M., Gu, Y., Gross, J., and Napolitano, M. R., "Evaluation of Matrix Square Root Operations for UKF within a UAV-Based GPS/INS Sensor Fusion Application," *International Journal of Navigation and Observation*, Vol. 2011, Article ID 416828, Dec. 2011.

[25] U.S. Environmental Protection Agency, "Meteorological Monitoring Guidance for Regulatory Modeling Applications," 2000.

[26] Elliott, D. L., "Adjustment and Analysis of Data for Regional Wind Energy Assessments," Workshop on Wind Climate, Asheville, North Carolina, November 12-13, 1979.

Paper A.2

Design, Simulation, and Flight Test Validation of a UAV Ground Control Station for Aviation Safety Research and Pilot Modeling

Trenton Larrabee[6], Haiyang Chao[7], Tanmay Mandal[8], Srikanth Gururajan[9], Yu Gu[10], Marcello Napolitano[11]
Department of Mechanical and Aerospace Engineering, West Virginia University, Morgantown, WV, 26506-6106

UAV Ground Control Stations (GCS) are being increasingly used for research topics such as subscale aircraft modeling, pilot modeling, pilot-aircraft interface modeling, and UAV mission evaluation. This paper presents the development, simulation, and validation of a UAV GCS with an emphasis on flight test evaluations. The development of hardware and software for both the GCS and UAV platform are introduced along with the development of a simulator for pilot training. Through both ground simulations and UAV flight tests, the capabilities of the GCS have been validated and proven to be capable of meeting current research needs as well as opening up new areas for future research.

I. Introduction

Ground Control Stations together with Unmanned Aerial Vehicles (UAVs) are important tools for increasing the capability, autonomy, safety, and reliability of traditional manned aircraft through aircraft and pilot modeling as well as unmanned aircraft systems. Nowadays, GCSs are being frequently used by the military for unmanned aircraft operations to free human pilots from dangerous, dull, and dirty jobs. With the possible future integration of UAVs into the National Air Space (NAS), UAV GCSs will have more civilian applications including search and rescue, emergency response to natural disasters, scientific monitoring, and many others. From a research point of view, the development of a GCS can strongly augment and support aviation safety research projects based on UAVs by simulating piloted flight following Visual Flight Rules (VFR). Researchers at NASA Langley have been leading the community along this direction through their AirSTAR project by developing an advanced GCS for their subscale research aircraft used for the validation of advanced flight control laws for fault tolerance purposes and real-time parameter identification[1].

Most of the military and scientific research requires the development of customized UAV GCSs for their specific objective. Therefore, different types of UAV GCSs have been ad-hoc designed and developed. The military relies heavily on the capabilities of GCSs for control and mission planning of UAVs such as the Reaper or the Predator in various missions including surveillance, reconnaissance, and strike tasks[2], which are usually tolerant to system delays which could be several seconds. Similarly, the ANKA program designed by the Turkish Aerospace Industries

[6] M.S. Student, Dept. of Mechanical and Aerospace Engineering, West Virginia University, Morgantown, WV, USA. 26506. Email: tlarrab1@mix.wvu.edu, AIAA Member.
[7] Postdoctoral Fellow Dept. of Mechanical and Aerospace Engineering, West Virginia University, Morgantown, WV, USA. 26506. Email: Haiyang.Chao@mail.wvu.edu, AIAA Member.
[8] Ph.D. Student, Dept. Mechanical and Aerospace Engineering, West Virginia University, Morgantown, WV, USA. 26506. Email: tmandal@mix.wvu.edu, AIAA Member.
[9] Postdoctoral Fellow, Dept. of Mechanical and Aerospace Engineering, West Virginia University, Morgantown, WV, USA. 26506. Email: Srikanth.Gururajan@mail.wvu.edu, AIAA Senior Member.
[10] Assistant Professor, Dept. of Mechanical and Aerospace Engineering, West Virginia University, Morgantown, WV, USA. 26506. Email: Yu.Gu@mail.wvu.edu, AIAA Senior Member.
[11] Professor, Dept. of Mechanical and Aerospace Engineering, West Virginia University, Morgantown, WV, USA. 26506. Email: Marcello.Napolitano@mail.wvu.edu, AIAA Senior Member.

and used by the Turkish Air Force has developed a GCS for control and monitoring of an air vehicle in real-time as well as mission planning, data recording, and querying that is non-real-time[3]. Not only military but several universities, research centers, and private companies have developed GCSs for research with various types of UAVs such as Berkeley's BEAR research facility[4] used mainly for rotorcraft while the previously mentioned AirSTAR is used for research into aviation safety by testing loss of control scenarios without risk to a piloted aircraft[1]. L-3 Unmanned Systems has developed a portable command and control station for UAVs that is available commercially[5]. However, most of the GCS configurations are designed either for simple monitoring functions, or for expensive military or governmental missions, which are not suitable for universities or small companies. It is envisioned that low-cost, compact yet capable UAV GCS solutions are needed by researches specifically involved in pilot modeling, pilot training, etc.

As an interface between human pilot and the unmanned system, UAV GCSs can also be used for Human Systems Integration (HSI) research with the general goal of enhancing the capabilities of the overall pilot-UAV system. A group from the Air Force Research Laboratory along with Arizona State University Polytechnic has researched the pilot's ability for navigation and orientation within the virtual environment, the modeling of the pilot's cognitive process within maneuvering and reconnaissance missions, verbal communication between pilot and synthetic entities, as well as analysis of team skill[6]. Another research effort has focused on how to reduce the work load of UAV operators while at the same time mitigating safety issues when the number of aircraft being controlled increase compared to the number of operators[7]. Not only has this been done using single modes of communication between pilots and GCSs, but efforts have gone into how to combine these into multimodal approaches for reduced load by increasing the avenues from which the operator may receive information[8]. Another piece of valuable information is determining what information the pilot is most interested in during UAV control. Through eye tracking of the pilot, research has shown what data the pilot is most concerned about[9]. Along similar lines of research, the University of North Dakota has developed a mobile information display, similar to a GCS without control, that is designed specifically for detecting low flying, observable aircraft[10]. These research topics have shown a great interest in understanding not only how the pilot controls the UAV through the GCS, but also how to best improve the interaction between the pilot and the GCS.

This paper presents the development, testing, and validation of a GCS that is capable of being used for research including pilot and aircraft modeling, system identification, human-machine interface modeling and implementation. The WVU GCS is currently fulfilling two distinct roles: simulation and various UAV flight testing purposes for the WVU Flight Control System Laboratory. The WVU GCS allows for real time monitoring of the aircraft information from the avionics system, pilot commands, aircraft health status, and weather information. This includes not only numerically displayed data but also visually displayed data from a live video nose camera, virtual horizon, ground track, and a synthetic cockpit view synced with the software X-plane[11]. Also, the WVU GCS has the ability to communicate with the safety pilot, research pilot, and on-board flight control systems. Each of these systems can be used independently or cooperatively which allows for unique research capabilities that can replicate real life flight scenarios while keeping the pilots safe. For example, fault tolerant control systems can be studied by injecting failures into the system which takes the aircraft outside its nominal flight envelope while the research pilot remains safely on the ground and the safety pilot has the ability to recover the plane under loss of control conditions. The contributions of this paper include the development of a GCS simulator for testing and modeling purposes, and to outline the capabilities of the GCS in terms of allowing UAV control through three different modes: manual, autopilot, and augmented. This paper also shows flight testing results of GCS controlled UAV flights.

This rest of this paper is prepared as follows. The general design and development of the GCS are described in section II. Section III discusses the hardware setup for both the GCS and the UAV research platform while section **Error! Reference source not found.** highlights GCS functionality and software. Section V discusses results from simulated flight and section VI discusses flight test data. Finally, a summary of the results are found in section VII.

II. GCS Application & Design Objectives

A fully functional GCS provides for research capabilities which cannot be achieved through R/C flight alone. Clearly, the GCS allows pilot modeling with the use of subscale aircraft. Similarly, the use of the GCS is also important for Parameter Identification (PID) research since the pilot no longer has to rely on flying the UAV by visual contact from the ground, but now can track actual values of flight from displayed data which helps in performing precise maneuvers used for aircraft modeling. Finally, the use of the GCS naturally leads to research into new applications of subscale aircraft for otherwise dangerous or long mundane tasks[12]. In general the use of a GCS allows for :

1) Pilot modeling at various conditions including Pilot Induced Oscillations (PIO), Loss of Control (LOC) events (which accounted for 59% of commercial aviation fatalities from 1997-2006[13]), and flights outside of the nominal flight envelope.
2) PID at extreme flight conditions, including high angle of attack, stall conditions, high angular velocity, and other.
3) Simulated flight in commercial or military aircraft outside of nominal flight conditions and extreme maneuvers through the use of UAVs.
4) Surveillance using UAVs for situations that require human intelligence and interaction.
5) Communications relay through long duration UAVs that can act as a network in the sky.

The WVU GCS was designed to have the following capabilities:

1) A ground simulator, to be used for the pilot modeling as well as for pilot training.
2) Flight testing capabilities for verification of pilot and aircraft modeling as well as better pilot-GCS interfacing.
3) Different levels of autonomy for UAVs to support further researches on human systems integration. This includes a manual mode that gives the pilot full control over all control surfaces and throttle settings, an autopilot flight mode that allows for GPS waypoint tracking, and finally, an augmented flight mode that allows for assisted aircraft flight.

In addition, the WVU GCS can also be configured to work with additional R/C vehicles such as unmanned ground/water vehicles.

III. GCS and UAV Hardware System

The hardware system of the designed UAV ground control station is introduced briefly in this section[14].

GCS

The GCS is comprised of four major components:

1) The Pilot Control Input unit
2) The Communication unit
3) The GCS displaying unit
4) The Central Computer

A rugged computer powered by Intel Core i5-2300 processor serves as the central computing/communications/interface hub. This computer is used for converting pilot inputs to commands and sending them to the wireless modem. It also receives and displays data from the UAV. During the flight testing operations there are two pilots, the safety pilot and the GCS research pilot. The research pilot controls the UAV through pilot control input unit, following Visual Flight Rules (VFR). The safety pilot controls the UAV through RC link and will only take control from the research pilot should the research pilot lose control via a switch on the R/C transmitter. The safety pilot is responsible for the take-off and the landing. **Figure 10** shows the WVU GCS and Figure 2 shows the hardware communication protocol. The functions of each subsystem are described below.

Pilot Control Input Unit

A Hotas Warthog side stick, CH PRODUCTS pro pedals, and a Thrustmaster throttle are used for pilot inputs. These are used for the generation of the pilot commands for ailerons, elevators, rudder, and throttle as well as for surface trimming and choosing which screens are displayed in the GCS displaying unit (discussed further in Section III.A.3). Each input has a range of 65536 points, or 16 bit resolution. The GCS software converts the raw inputs into an 8 bit commands with a range of 0 to 255 and then sends them out to the onboard flight computer for surface control through wireless communications.

Communication Unit

The communication between the GCS and the UAV is accomplished using a 900MHz serial data link via a pair of FreeWave® modems. The GCS modem is connected to the central computer through a serial RS232 connection. The modem antennas used for the GCS and UAV are both omnidirectional antennas with a gain of 5dBi and 0dBi respectively. A 0 dBi antenna was selected for the UAV because of its smaller size and weight and also because of the changing orientation and position of the UAV during flight tests. **Figure 11** shows the communication protocol for GCS hardware. Each uplink packet consists of control commands sent from the pilot station, a 2 byte header, a

checksum, and is a total of 16 bytes of data. Downlink packets are 64 bytes in length and include the following: header, checksum, IMU data, GPS data, control commands, air pressure data, flow angles, and attitude angles.

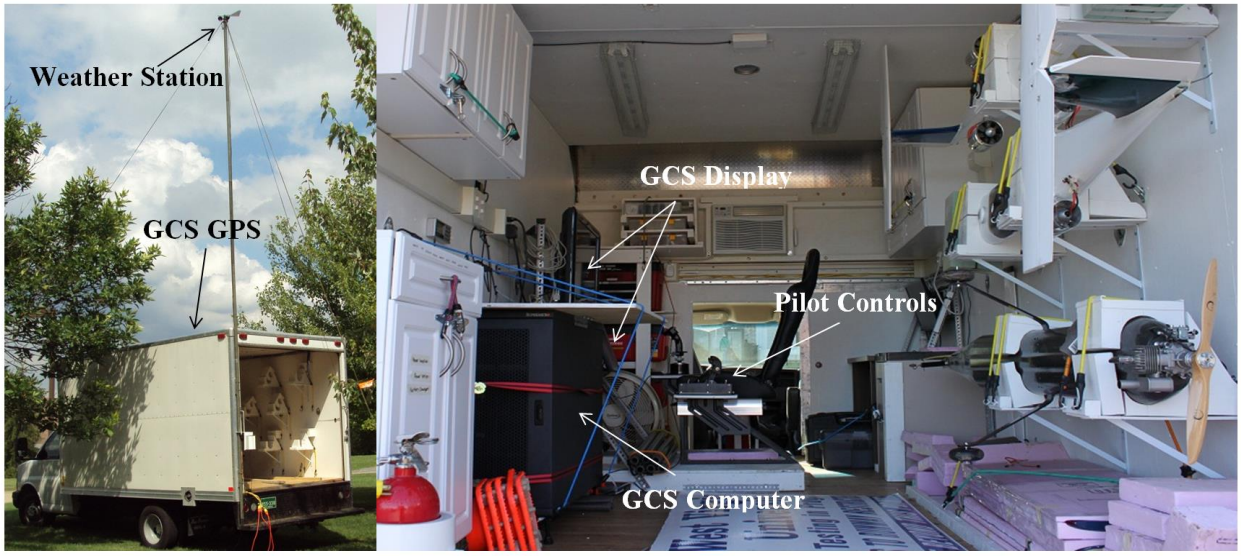

Figure 10. WVU GCS

Figure 11. UAV & GCS Communication Protocol

GCS Display Unit

The purpose of the GCS display unit is to provide both uplink and downlink data to the research pilot. First, a message tree, shown in **Figure 12**, is used to display text data for each specified parameter. Next, data is displayed in a Heads-Up Display (HUD) overlaid on X-plane for a synthetic vision of flight, as shown in **Figure 13**. Finally, there is a pilot station that can display 2 windows out of a possible of 5 to visualize the same data in the message tree. A box at the top of the pilot station will display "SAFETY" when the safety pilot is in control of the UAV and will highlight green and display "RESEARCH" when the research pilot is in control of the UAV. The three windows shown in **Figure 14** are:

1) Primary Flight Display (left): This window contains a virtual horizon that displays pitch and roll angles of the UAV as well as heading. Velocity, altitude, angle of attack, sideslip angle and climb rate are shown on the HUD. Finally, magnetometer and accelerometer data are shown at the top along with angular rates.
2) Overhead Map Display (middle): This window shows a ground track for the UAV as well as the position of

the GCS.

3) Surfaces Display (right): This window displays the deflection of all 5 surfaces as well as both throttle settings. The data is displayed both graphically and numerically for each channel.

downlink [30928]		
count	208	Packet Count
ps	46.08	Static Pressure
qc	321.27	Dynamic Pressure
alpha	-2.78001	Alpha
beta	0.259993	Beta
airtemp	-273.15	Air Temperature
p	0.0599927	P
q	0.0199927	Q
r	-7.30902e-06	R
ax	0.0293229	Acceleration X
ay	0.0191189	Acceleration Y
az	-0.933935	Acceleration Z
mx	51650	Magnetic X
my	21350	Magnetic Y
mz	233.42	Magnetic Z
pitch	1.72843	Pitch
roll	2.30139	Roll
pwm_lele	134	Deflection - Left Elevator
pwm_rele	123	Deflection - Right Elevator
pwm_lail	91	Deflection - Left Aileron
pwm_rail	104	Deflection - Right Aileron

Figure 12. Message Tree Showing Partial Downlink Data During Flight

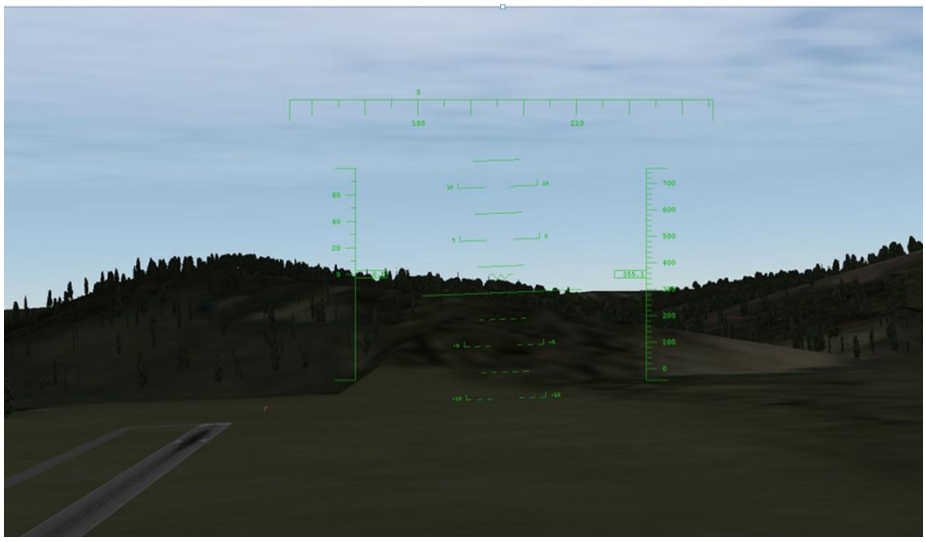

Figure 13. Synthetic Vision

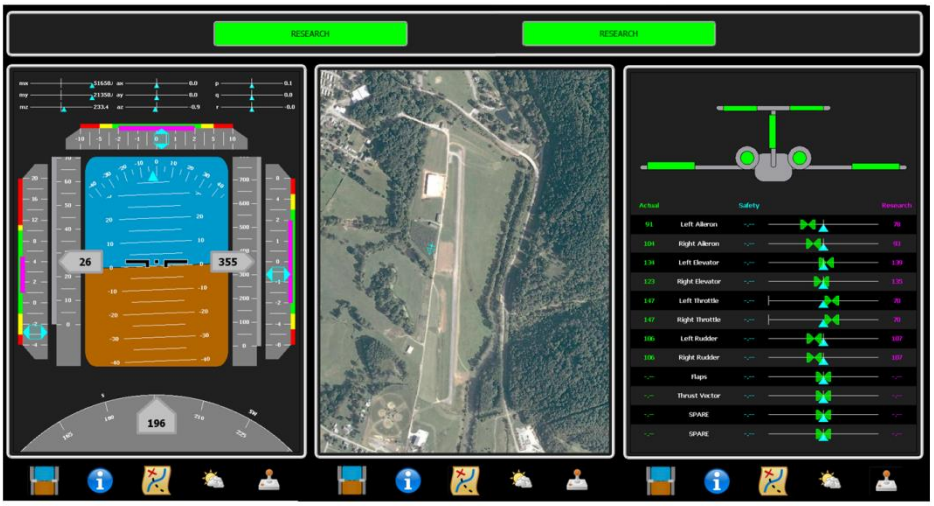

Figure 14. GCS Display Windows: Primary Flight Display, Overhead Map Display, and Surfaces Display

Phastball UAV Platform

The WVU 'Blue' Phastball UAV, shown in Figure , is used for interfacing with the GCS. The fleet of WVU Phastballs also includes a 'Red' and a 'Green' aircraft, however, the 'Blue' aircraft is currently the only aircraft flown with the GCS. These research aircraft were designed, manufactured, and instrumented by researchers at the WVU Flight Control Systems Laboratory at WVU. The WVU Phastball is 2.2 meters in length and has a wingspan of 2.4 meters. It features a mid-wing and T-tail configuration with two brushless electric ducted fans mounted behind the wings. The WVU Phastball has a take-off weight of approximately 11 Kg which includes a payload of 3 Kg. It has a cruise speed of 30 m/s. The fuselage is a carbon fiber and fiberglass composite with plywood bulkheads and rails used for mounting hardware.

For the onboard avionics[15], each WVU Phastball is equipped with a flight computer and a complete sensor suite including GPS, Inertial Measurement Unit (IMU), three potentiometers for aircraft flow angles (2 for angle-of-attack and 1 for sideslip), humidity and temperature sensor, laser range finder, and a pitot tube with both static and dynamic pressure measurements. For communication with the GCS, each aircraft also has a FreeWave® FGR2-Ce_U 902-928 MHz wireless data transreceiver and a PSTGO-925SE series 900MHz 0dBi Omni directional antenna from Mobile Mark, as well as a KPC650 high resolution CCD camera which communicates with the GCS via a 1.28 GHz 800mW video transmitter from Range Video. The WVU Phastball can support the following modes:

1) R/C: Safety pilot has full control of all surfaces and throttle settings
2) Autopilot: Flight computer controls flight maneuvers
3) Pilot in the Loop: Same as autopilot except either the R/C or GCS pilot maintains control of surface deflection
4) GCS Manual: GCS pilot has full control of all surfaces and throttle settings
5) GCS Augmented: GCS pilot has control of desired attitude heading and throttle setting

Figure 15. WVU 'Blue' Phastball

IV. GCS Basic Functions

The basic functions of the WVU GCS for IFR flight are described in this section. The purpose of the 'Simulation Function' is to fly through the GCS with the feedback from a 6 DOF aircraft model in place of the UAV. The purpose of the 'Flight-Test Function' is to fly the UAV through the GCS under instrument flight rules through flight tests.

A. Simulation Function

1. Capabilities

The design objective for the WVU GCS simulator was to create a platform that could be used for pilot training, testing of new software and human-machine interfacing, pilot modeling, and aircraft research. **Figure 16** shows the communication protocol and setup for the simulator. First, it is essential to train pilots and test new functions for the GCS including new hardware and software updates. Pilot training can be conducted using a Phastball mathematical model[16] under a manual and augmented control mode (discussed in Section IV.B.2). Pilot modeling can be conducted through various flight scenarios that push the efforts of the pilot as well as modeling the ability of pilots with different flight experiences. Finally, research can be conducted for aircraft during extreme maneuvers, flight conditions in abnormal environment conditions, etc. **Figure 17** shows the setup for the GCS simulator.

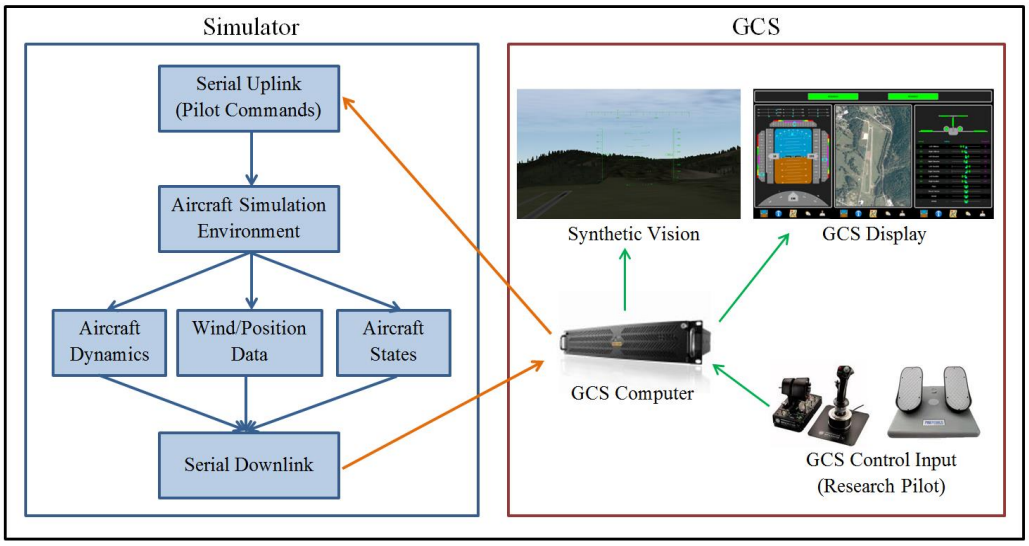

Figure 16. Simulator & GCS Communication Protocol

Figure 17. WVU GCS Simulator Setup in Lab

2. Design

The simulator of the Phastball was developed within a Matlab®/Simulink® environment. The general block diagram of the simulator is shown in **Figure 18**. The simulator is based on the Flight Dynamics and Control Toolbox[17] (FDC) which was developed as an open source simulation within the Simulink® software. Based on the results of the previous PID efforts[16], the default Beaver in the FDC was replaced with a non-linear dynamic model of the WVU Phastball aircraft. Additionally, a static and dynamic thrust model was developed and implemented into the simulator using experimental results. Serial communication is used for simulated uplink and downlink between the simulator and the GCS. The WVU Phastball simulator can implement both the manual and augmented control modes for the aircraft. These two types of control are discussed further in Section IV.B.2.

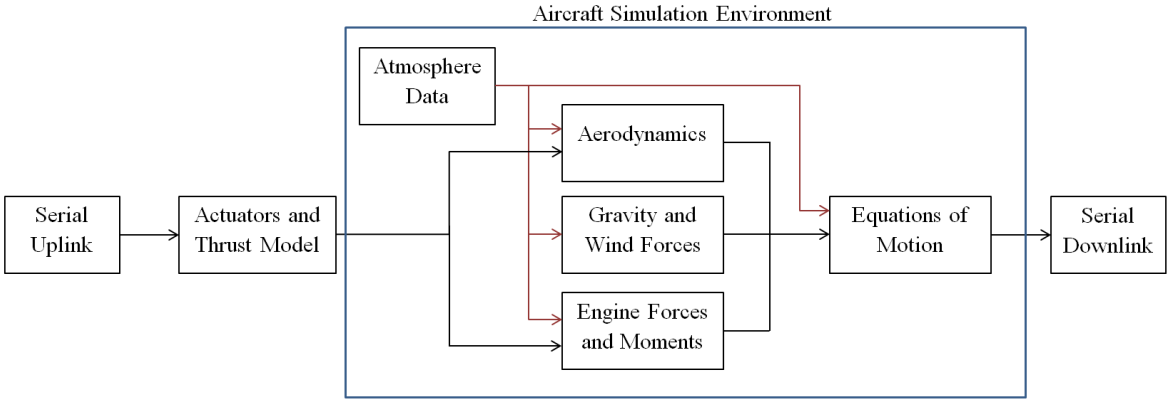

Figure 18. Conceptual Representation of Simulator Designed in Simulink

3. Benchmark Maneuvers

In order to validate the simulator certain "Benchmark" maneuvers were performed that would accurately depict each of the desired research areas for the GCS.

1) Piloted Aircraft Flight: In order to simulate instrumented flight in piloted aircraft it is important to perform certain maneuvers. These maneuvers come from the Instrument Flying Handbook written by the U.S. Department of Transportation Federal Aviation Administration[18] and they involve the ability for attitude and power control and are shown in **Table 3**.

Table 3. Basic Flight Maneuvers

Airplane Basic Flight Maneuvers	Maneuvers
Rectilinear Flight	Maintain Constant Airspeed, Altitude, and Attitude
Approach to Stall	Takeoff Configuration, Clean Configuration, Approach or Landing Configuration
Unusual Attitudes and Recoveries	Nose-High Attitudes, Nose-Low Attitudes
Basic Flight Patters	Racetrack, Standard Procedure Turn, 80/260 Procedure Turn, Teardrop Pattern, Circling Approach
Straight Climbs and Descents	Entry and Leveling Off for both Climbs and Descents
Turns	Standard-Rate, Turns to Predetermined Headings, Timed, Compass, Steep (excess of normal instrumented turns), Climbing, Descending

2) Pilot Modeling: In order to accurately model pilot behavior it is important to have the pilot fly under scenarios that replicate flight conditions used for real flight simulation and research purposes. This includes flying under a time delay in order to look at how the delay in control affects the pilot's ability to perform maneuvers and stabilize the aircraft. Flying with limited rates on surfaces or having the pilot fight maneuvers from the flight computer such as doublets performed on various channels can show pilot learning under adverse conditions as well as research how they compensate for these changes.

3) Aircraft Modeling: For aircraft modeling it is important to excite each mode of the aircraft. Flying doublets as well as performing multisines on each control surface helps in developing accurate models through parameter identification. Flying the aircraft at high angles of attack and performing extreme maneuvers will give a gauge on how well the aircraft will react as well its physical limitations in flight.

4) Surveillance: Simulating surveillance missions require long duration flights that encircle a desired area of importance. The GCS can implement an autopilot mode for flying certain patterns such as circles or figure eights over designated coordinates. Data can be sent to the GCS in real time that allows for human interaction and decision making.

B. Flight Test Function

1. Design Objectives

In order to qualify the GCS as operational for research, it had to function as well as or better than R/C flight, therefore the research pilot was instructed to fly a series of maneuvers in order to replicate R/C flight for a comparison to previous research capabilities. These maneuvers included pitch and roll doublets, coordinated turns, and GCS control of an entire flight lap. Once the pilot was comfortable with his ability to complete the doublets he moved onto the coordinated turn and finally to the complete flight lap.

2. Control Modes

Three types of operating modes were developed to control the WVU Phastball from the GCS, the manual mode, augmented flight mode, and autonomous mode. In the manual mode, the GCS pilot sends commands directly to the five control surfaces and the throttle through the movement of ground joystick. In this mode the GCS is in full control of the aircraft. The augmented flight mode has the ability for tracking desired attitude angles as well as desired rates for roll and pitch. The GCS pilot controls desired values, either heading or rates, through the ground joystick. In this mode, he has direct control of the throttle settings while he does not have control over the rudder setting.

In order to implement the augmented flight mode a set of Linear Quadratic Regulator (LQR) based control laws are running onboard of the UAV to convert desired attitude angles to servo movements. The object of the state regulator is to drive the initial condition error to zero, in this case the difference between desired and actual attitude. The gains for the controller were initialized through the controller design with the identified Phastball model, and then fine-tuned through flight testing. By default with no control input from the pilot, the aircraft will track a desired pitch angle of two degrees and a desired roll angle of zero degree which is based on typical angle-of-attack at cruise speed. Figure 19 shows the design architecture for the augmented flight mode during attitude tracking.

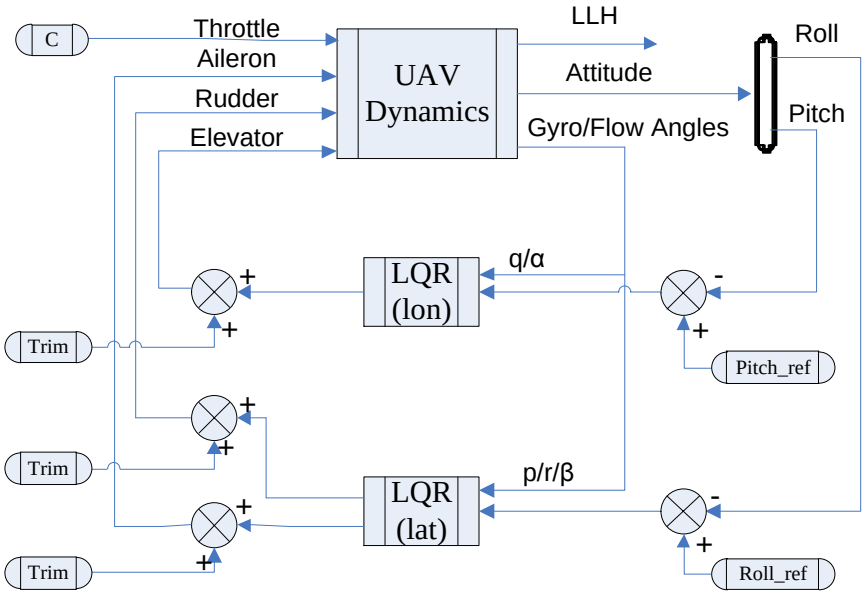

Figure 19. Overview of Augmented Flight Control.

For flight testing the same maneuvers identified for the simulator, Section IV.A.3, are applicable for the verification of the GCS in flight testing.

V. Simulation Results

A. Simulation Data

Using the GCS, simulated flight data was collected through particular maneuvers that would simulate real flight as well as give a comparison current R/C fight capabilities. These maneuvers included doublets that would compare simulated flight with R/C flight as well as help to verify the Phastball model by comparing results to flight data. Next, flight maneuvers consisting of a racetrack pattern and figure eight pattern where chosen based on a few considerations. First, the flight testing environment consists of flying a racetrack pattern and therefore it is valuable

to be able to teach pilots using the same conditions they will see in flight. This pattern also showed the capabilities of the simulator to perform basic flight patterns shown in **Table 3**. Finally, the figure eight pattern was chosen to analyze the capabilities of the simulator to fly more exotic flight formations that include both right and left handed turns which can be useful for surveillance purposes. As shown in section VI.C each of these maneuvers except the figure eight pattern was reproduced in flight testing using GCS control. Future work includes an exhaustive performance analysis of the simulation by performing each of the maneuvers discussed in **Table 3** as well as performing maneuvers for research such as PIO or LOC.

Figure 20 and **Figure 21** show pitch and roll doublets respectively. By comparison the pitch doublet performed by the GCS simulator and R/C flight are similar in magnitude while the roll doublet is a bit larger hitting a max roll angle of about 55 degrees. In terms of the length of the doublet the simulator is approximately twice as long as the R/C performed doublets.

Figure 22 shows the ground track as well as the roll and pitch angles of the UAV during a full lap performed by the GCS simulator. As shown the flight lap is slight larger than flight tests, **Figure 29**, covering about 2382 meters in about 55 seconds which is about 500 meters further and 5 seconds longer. The roll angle shows a maximum value of about -45 degrees during turns while the average pitch angle during the flight was about -0.7 degrees.

Finally, **Figure 23** shows the capabilities of the simulator flying a figure eight pattern. The goal of this maneuver was to turn in both directions as well as looking at the ability to fly certain patterns. This maneuver covered about 1827 meters in 50 seconds. The pitch angle had an average of .93 degrees while the roll angle averaged at -1.53 degrees.

It is important to note here that the latency the simulator, the time it takes for the data to go from the GCS to the simulator and back, is just over 0.08 seconds or about 4 time steps. This latency was calculated while X-plane was running on the GCS. The above maneuvers showed the effectiveness of the designed GCS for simulation purposes. Future work will focus on aircraft and pilot modeling such as adding different types of communication delays to create pilot-induced-oscillations.

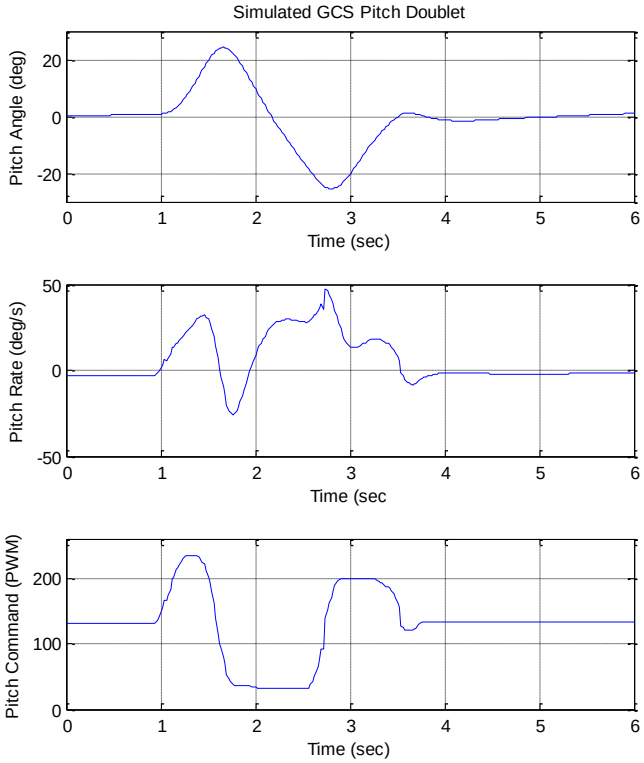

Figure 20. Simulated GCS Pitch Doublet

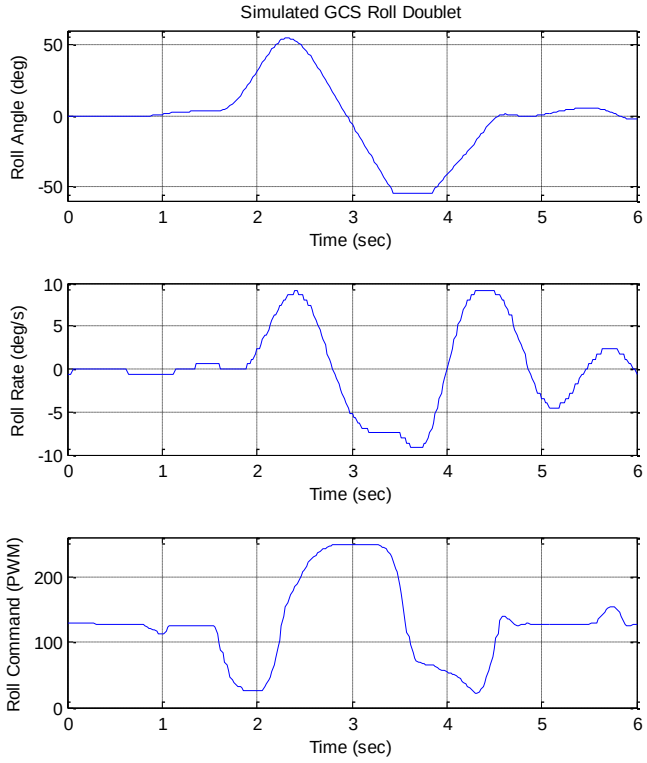

Figure 21. Simulated GCS Roll Doublet

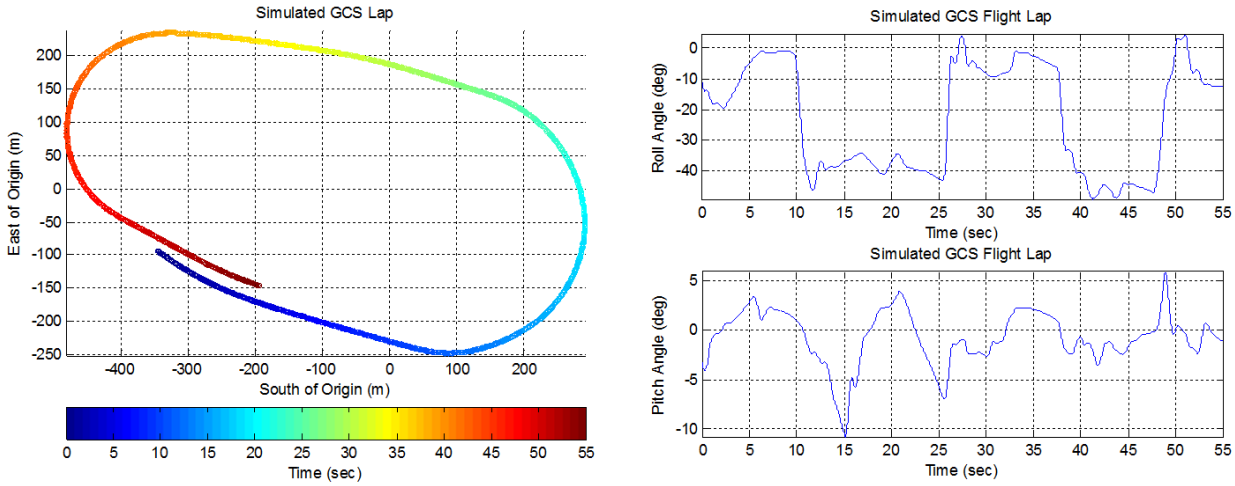

Figure 22. GPS Track with Roll and Pitch Angles for Simulated GCS Flight Lap

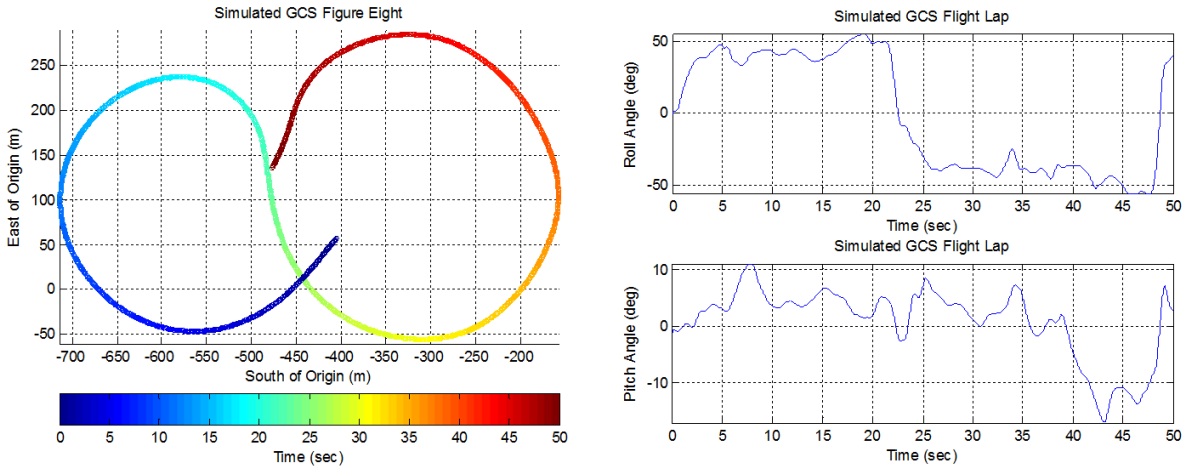

Figure 23. Simulated GCS Figure Eight

VI. Flight Testing Results

A. Flight Testing Environment

The WVU flight testing activities are conducted at the WVU Louis Bennett airfield. The flight facility covers 80 acres at an elevation of 309 meters and has a single asphalt runway which is 974 meters long and 15 meters wide and slants 10 degrees east of north. Based on battery capacity each flight is approximately 6 minutes from takeoff to landing with about 5 minutes of flight.

A communication protocol between the GCS pilot and safety pilot has been developed for flights involving the GCS control both for manual and augmented. Communication between the safety co-pilot and research co-pilot is conducted over two way radios.

B. UAV-GCS Communication Test

Extensive flight tests were conducted during the 2011 and 2012 flight testing seasons to validate and improve the performance of the GCS. Different hardware models, locations, and settings were investigated on the GCS vehicle to reach satisfying results; this is the case of the transreceiver and its antenna were investigated through both ground and UAV flight tests to reach satisfying results.

Both downlink and uplink have been thoroughly tested through UAV flight tests. A high level of reliability was reached for the downlink communication part, and the corrupted and lost packets are less than 0.2% when flying under typical conditions. For the uplink communication, the sum of corrupted and lost packets reaches a maximum packet loss of 38% during a one-second window however the total packet loss was only 1.94% for the entire flight. **Figure 24** shows the percentage of lost packets while on the UAV was on the runway and during flight; note that flight takes place between approximately 200 and 500 seconds. **Figure 25** shows the percentage of lost or corrupted uplink packets with respect to aircraft ground position, the plot on the right shows one lap while the plot on the left shows the entire flight. It is observed that these maximum losses happen along the North portion of the lap as well as during high banked turns. This could be due to the relative positions of the UAV and GCS antennas as well as the increased distance between the UAV and GCS. Another possible reason for the data loss of the uplink is that GCS software does not always send in 50 Hz, since the GCS computer is not running in real time. It is worth mentioning here that the uplink rate was observed to dramatically increase when synthetic vision via X-Plane was not running. Because of this issue, the synthetic vision was not utilized during flight tests. In the future it is planned to remedy this problem by running the synthetic vision on a secondary computer dedicated to the visual interface. Finally, it is important to note here that the total latency of the GCS is roughly 0.072 seconds or about 3.6 time steps.

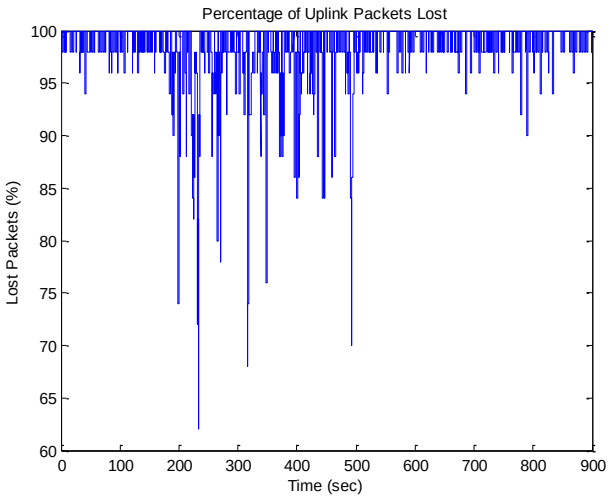

Figure 24. Uplink Rate (Packets per Second)

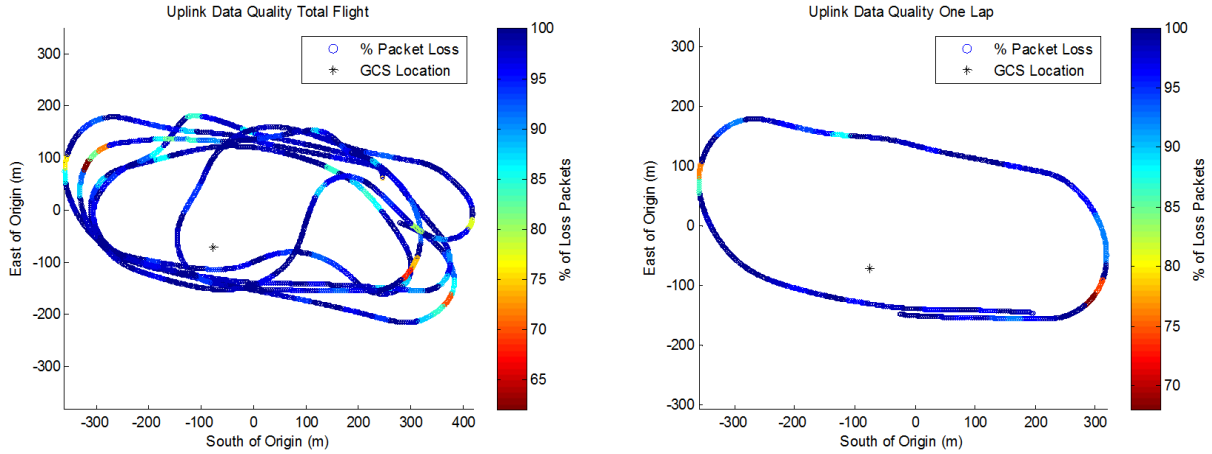

Figure 25. Uplink Packets Received During GCS Controller Flight

C. Flight Data

1. Aircraft Modeling

For comparison between GCS flight and R/C flight both pitch and roll doublets were performed with the final goal of flying a complete lap from the GCS. The following flight data was collected during four manual flights and two augmented flights totaling about 17 minutes and 36 seconds of GCS controlled flight. During manual flights the research pilot completed 4 pitch doublets and 4 roll doublets. Augmented flights resulted in 4 lateral doublets, 7 longitudinal doublets, 2 coordinated turns, and 1 complete flight lap. Augmented flight data presented below was conducted through attitude tracking.

Figure 26 and **Figure 27** show both pitch and roll doublets respectively performed by the research pilot under full manual control of the aircraft. For comparison the same maneuvers performed by the safety pilot during R/C flight are shown to the right. The GCS and manual pitch doublets both take about the same amount of time to perform, while the GCS pilot sent more aggressive pitch command and induced larger maximum pitch angles. The manual GCS pitch doublet shows a starting angle of about -2 degrees and ends at about 10 degrees while the R/C doublet starts around -2 degrees and ends at -6 degrees. It is important to note that the GCS pilot is still in the process of learning to make the link from the numbers on the display to the orientation of the UAV. The roll doublet was more difficult to perform which can be seen in the data provided. The GCS roll doublet command was more severe than the transmitter doublet. The GCS control was terminated by the safety pilot after about a half second for safety reasons.

Compared to manual doublets the augmented doublets are much more precise as well as much closer to manual doublets from the transmitter. The pitch doublet shows a max angle of about 19 degrees compared to the R/C doublet of about 9 degrees while the pitch rates are much closer. For the augmented GCS control the pitch

doublet takes about a half a second longer than R/C doublets. The roll angle and joystick command for augmented control mode looks much smoother than the R/C doublet. The research pilot performed both a left and right roll for one double whereas the R/C doublet consists of only a right roll. The augmented doublet starts at near zero and ends there as well whereas the R/C roll starts at about -10 degrees and ends at about -2 degrees. The roll rate for the R/C maneuver is much smoother but the constant control of the controller makes the movements of the augmented controlled doublet smoother. Once again, the joystick command of the augmented GCS control is converted to a desired roll angle within the flight computer.

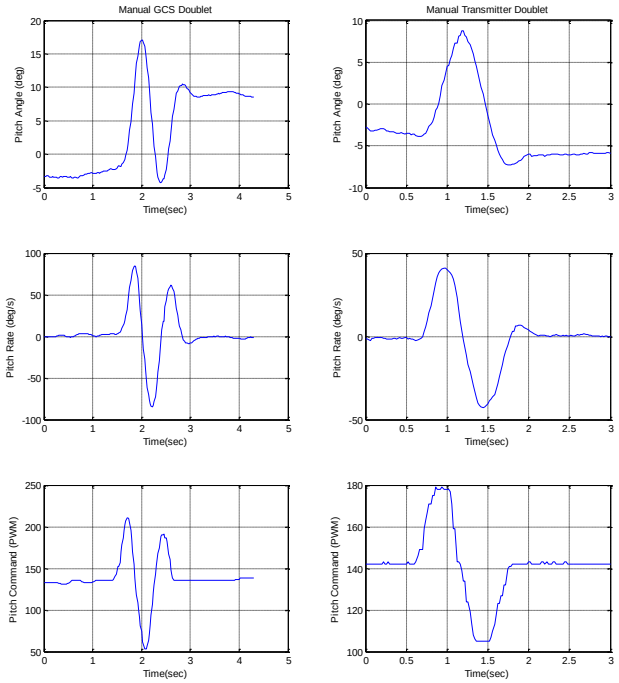

Figure 26. Pitch Doublet from GCS in Manual Mode and from Transmitter

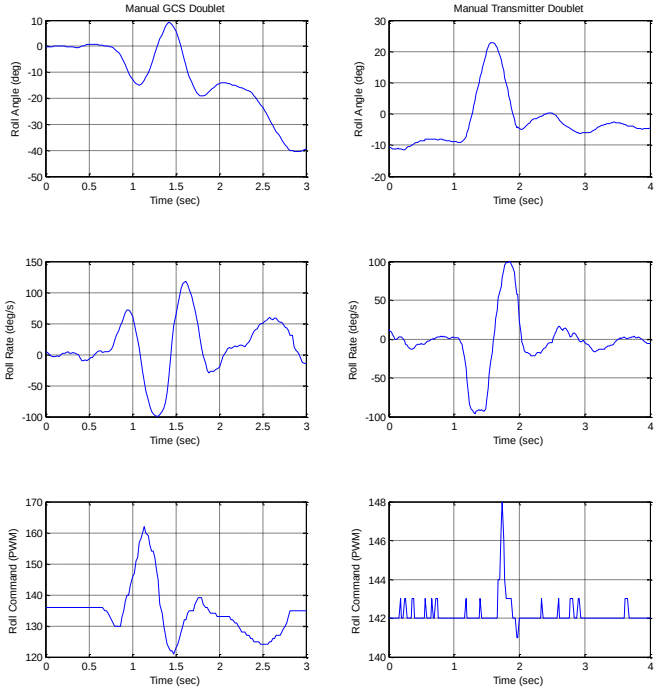

Figure 27. Roll Doublet from GCS in Manual Mode and from Transmitter

2. Instrumented Piloted Flight / Surveillance

Figure 28 shows a coordinated turn on the North end of the flight path and takes approximately 30 seconds to perform and covered about 690 meters of ground distance. The data shows the actual roll angle tracked very well with the desired roll angle with a variation of about three degrees. The actual pitch angle follows the same trend as the desired pitch angle and for the most part stays well within five degrees but there is one part during the second half of the turn where the difference is nearly ten degrees.

Finally, under augmented control mode a complete flight lap was performed. This can be seen in **Figure 29** which shows the ground track as well as both desired and actual heading angles. The ground track shows that the entire lap took just about 50 seconds and covered about 1844 meters of ground distance. The actual roll angle stays within about two degrees of the desired roll angle whereas the actual pitch angle stays within about three degrees of the desired pitch angle.

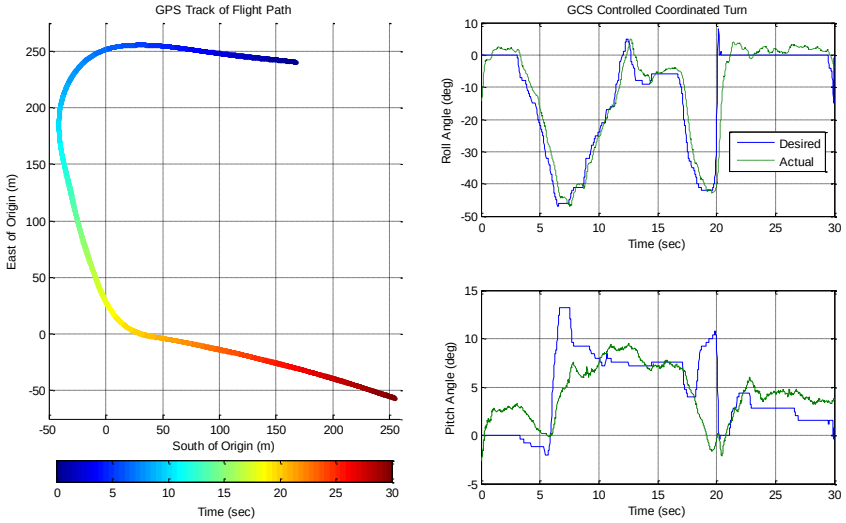

Figure 28. GPS Track with Roll and Pitch Angles for Coordinated Turn

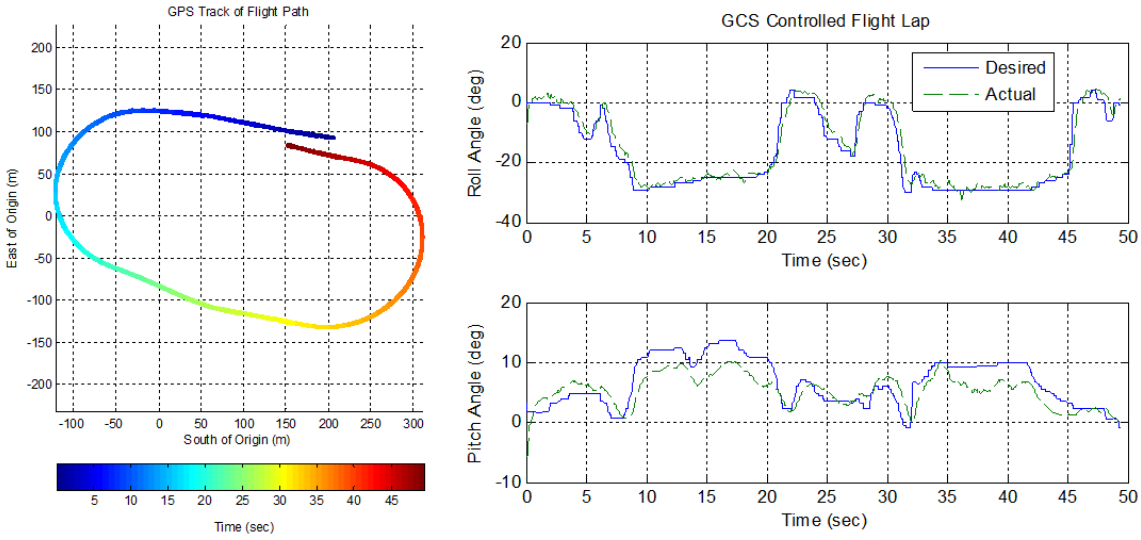

Figure 29. GPS Track with Roll and Pitch Angles for GCS Augmented Control Flight Lap

VII. Conclusions & Future Work

This paper has described the design and the development of the WVU Ground Control Station (GCS). Currently the WVU GCS is fully functional with two modes of operation, manual mode and augmented flight control mode. The GCS pilot has successfully flown the WVU Phastball in both modes. In addition, the WVU GCS has been used for pilot training with its support for flight simulation with identified 6-DOF dynamic model. Some of the lessons learned through the development of the GCS include communication setup, hardware debugging, and GCS pilot feedback.

The development of reliable communication between the GCS and the UAV was an area of extensive study and experimentation. It was found that a 0 dBi Omni-directional antenna was the best for the aircraft considering budget limit because it did not interfere with the range of the aircraft and because of the constant orientation change of the UAV. For the GCS, it was found that a 5 dBi Omni-directional antenna was also good for similar reasons. Point to point protocol was found to be the best between FreeWave® modems with the UAV as the master and the GCS as the slave. In the future it is planned to move to a multipoint setup with the GCS as the master and the UAVs as slaves which will allow for control of multiple UAVs which would be useful for experiments such as formation flight.

The GCS research pilot through the UAV flight test is an experienced pilot for RC airplanes. It is observed that a RC pilot needs a significant amount of time for training to fly in manual mode while trivial training is required for augmented mode. Later flight tests will include different pilots with private pilot license or commercial pilot license.

In addition, future work will include further training of GCS pilots under extreme situations such as high angle of attack, human pilot modeling during GCS flight, and experiments for looking into pilot-induced-oscillations. Also, it is planned to conduct a rigorous testing of the simulator by completing all of the desired maneuvers for simulating piloted flight.

Acknowledgments

This research is partially supported by NASA grant # NNX10AI14G. The authors would like to thank Amanda McGrail and Matthew Rhudy for their support in research.

References

[1] Cox, D. E., Cunningham, K., & Jordan, T., "Subscale Flight Testing for Aircraft Loss of Control: Accomplishments and Future Directions," *AIAA Guidance, Navigation, and Control Conference*, Minneapolis, 2012, AIAA 2012-5029.

[2] Jordan, T. L., Foster, J. V., Bailey, R. M., & Belcastro, C. M., " AirSTAR: A UAV Platform for Flight Dynamics and Control System Testing" *25th AIAA Aerodynamic Measurement Technology and Ground Testing Conference*, San Francisco, 2006, AIAA 2006-3307.

[3]Kayayurt, B., Yayla, I., Yapici, A., & Küçükoğuz, C., "Ground Control Station Avionics Software Development in ANKA UAV", *IEEE/AIAA Digital Avionics Systems Conference (DASC)*, Seattle, vol., no., 2011, pp.5B6-1-5B6-7.

[4] "BEAR: Berkeley Aerobot Team," URL: http://robotics.eecs.berkeley.edu/bear/testbeds.html [cited 24 January 2013].

[5] "Generation IV Ground Control Station" URL: http://www2.l-3com.com/uas/tech_uas/gen_iv.htm [cited 24 January 2013].

[6] Gluck, K. A., Ball, J. T., Gunzelmann, G., Krusmark, M. A., Lyon, D. R., & Cooke, N. J., "A Prospective Look at a Synthetic Teammate for UAV Applications" *AIAA Infotech@Aerospace Conference*, Arlington, 2005, AIAA 2005-6970.

[7] Franke, J., Zaychik, V., Spura, T., & Alves, E., "Inverting the Operator/Vehicle Ratio: Approaches to Next Generation UAV Command and Control." *Association for Unmanned Vehicle Systems International and Flight International*, Baltimore, 2005.

[8] Maza, I., Caballero, F., Molina, R., Peña, N., & Ollero, A., "Multimodal Interface Technologies for UAV Ground Control Station" *Journal of Intelligent and Robotic Systems*, Vol. 57, No. 1-4, January 2010, pp. 371-391.

[9] Tvaryanas, A. P., "Visual Scan Patterns During Simulated Control of an Uninhabited Aerial Vehicle (UAV)" *Aviation, Space, and Environmental Medicine*, Vol. 75, No. 6, June 2004, pp. 531-538.

[10] Marsh, R., Ogaard, K., Kary, M., Nordlie, J., & Theisen, C., "Development of a Mobile Information Display System for UAS Operations in North Dakota," *International Journal of Computer Information Systems and Industrial Management Applications*, Vol. 3, 2011, pp. 435-443.
[11] "Ultra-Realistic Flight Simulation" URL: http://www.x-plane.com [cited 29 January 2013].
[12] Sarris, Z., "Survey of UAV Applications in Civil Markets" *IEEE Mediterranean Conference on Control and Automation*, Croatia, 2001.
[13] Ranter, H., "Airliner Accident Statistics 2006," Tech. rep., Aviation Safety Network, 2007.
[14] Guerra, M., Rhudy, M., Gu, Y., Seanor, B., & Napolitano, M. R., "Mobile Ground Control Station Development for Fault Tolerant UAV Research," *AIAA Guidance, Navigation, and Control Conference*, Minneapolis, 2012, AIAA 2012-4544
[15] Gu, Y., Gross, J., Barchesky, F., Chao, H.Y., & Napolitano, M.R., "Avionic Design for a Sub-Scale Fault Tolerant Flight Control Test-Bed," Chapter 21, Recent Advances in Aircraft Technology, ISBN: 978-953-51-0150-5, InTech, pp. 499-522, 2012.
[16] Gururajan, S., McGrail, A., Gu, Y., Seanor, B., Napolitano, M., Prucz, J., & Phillips, K., "Identification of Aerodynamic Parameters for a Small UAV from Flight Data", *52nd Israel Annual Conference on Aerospace Sciences, Technion-I.I.T,* Haifa, Israel, Feb 29 – Mar 1, 2012.
[17] Rauw, M. O., "FDC 1.2 – A Simulink Toolbox for Flight Dynamics and Control Analysis," 2nd ed., Haarlem, The Netherlands, 1997.
[18] *Instrument Flying Handbook*, U.S. Department of Transportation Federal Aviation Administration, Oklahoma City, 2001, Chapt. 5.

Abstract of Paper A.3

Abstract

Wind and turbulence, including wakes induced by leading aircraft, have a large impact on flight performance and flight safety of both manned and unmanned aircraft. An accurate real-time wind/wake estimation technique is crucial for tasks such as increasing air traffic capacity, commercial formation flight, or aerial refueling, etc. A leader-follower formation flight of Phastball Unmanned Aerial Vehicles (UAVs) were used as the experimental platform for the above problem. The air data system of Phastball UAV was developed with pitot-tube and flow-angle sensors. Using the designed system, several representative wind estimation algorithms were validated for single UAV through collected flight data. In addition, an Unscented Kalman Filter (UKF) based approach is used for the 3D wind estimation and wake sensing in UAV formation flight. Simulation results showed the effectiveness of the proposed method for initial wake estimation with leader-follower formation. Finally, shortcomings of existing techniques and future directions of wind sensing are further discussed.

Abstract of Paper A.4

Abstract

Close Formation Flight is a key potential approach for reducing greenhouse gas emissions and managing traffic in future high density airspace. This paper discusses the implementation and flight testing of a formation flight controller. Experimental results show that an autonomous close formation flight with approximately 5-wingspan separation is achievable with a pair of low-cost unmanned research aircraft.